Vine, David John (2016) Measuring Johnson resistor noise in non-equilibrium conditions. MSc(R) thesis

http://theses.gla.ac.uk/7272/

Measuring Johnson Resistor Noise in Non-Equilibrium Conditions

David Vine B.Sc(Hons)

School of Physics and Astronomy,
University of Glasgow

Presented as a thesis for the degree of
Master of Science (Research)

2015

Contents

List of Figures

List of Tables

'If we knew what it was we were doing, it would not be called research, would it?'

Albert Einstein

Acknowledgments

I'd like to take this opportunity to thank everyone that has helped to make this thesis a possibility.

First and foremost I would like to thank both my supervisors Dr. Giles Hammond and Prof. Sheila Rowan. The guidance and support that they provided throughout this year was invaluable and without their advice I would not be where I am today.

I would also like to take the opportunity to thank the technical staff that helped with any construction that was required. I would like to thank Steven O'Shea for his help in designing and constructing the circuitry required for this experiment, Mr Colin Craig and Mr Russell Jones for assistance in the design and manufacture of sections of the experimental setup and Jamie Scott for his IT support. Throughout the project I received help from various academics with different aspects of the experiment. I would like to thank both Dr Liam Cunningham for his assistance with the ANSYS modelling required for this project and Dr Alan Cumming for his help and advice. The thin film platinum resistor used in this experiment were manufactured at The University of the West of Scotland and so I would like to thank both Dr Stuart Reid and Dr Ross Birney who were both involved in the manufacture of these resistors.

The year would not have been complete without my office mates and colleagues to provide encouragement and laughter. To Karen Haughian, Peter Murray and Sheena Barclay for keeping me sane and listening to my problems and woes, thank you for putting up with me. Thanks also goes to all members of the Institute for Gravitational Research for making the institute such a welcoming and friendly place to work.

On a more personal note I would like to thank everyone in my life that has provided love, support and encouragement to help me throughout this degree. In particularly, I would like to thank my sister and especially my mum and dad without which I would not have been able to undertake this degree. The help, support and encouragement they have provided during the degree means more to me than you know.

Preface

This thesis is an account of the work carried out in the Institute of Gravitational Research at the University of Glasgow between October 2013 and September 2014. The research here contributes to the investigation into the validity of the fluctuation-dissipation theorem in non-equilibrium systems such as future cryogenic gravitational wave detectors. The method used in this thesis involved measuring the thermal noise associated with a thin film platinum resistor, known as Johnson noise, with a thermal gradient present across the resistor. This investigation was carried out at the suggestion of Dr. Giles Hammond.

Chapter 1 provides a description of gravitational waves as well as potential sources. It also describes methods of detection and noise sources associated with the detectors. This work has been derived from current literature.

In Chapter 2, the theory of thermal noise is discussed. The mechanism of thermal noise and how it is quantified is shown, as well as a brief explanation into the motivation behind investigating non-equilibrium systems. This work has also been derived from current literature.

Chapter 3 describes the experimental setup used in this investigation. The design of the apparatus used to produce a thermal gradient across the sample resistor is explained as well as the control system and computer code that was used to maintain the required temperatures across the resistor. The experimental setup was designed with the help of Dr. Giles Hammond. The apparatus was constructed with the help of Mr. Russell Jones and Mr. Colin Craig and the electronics were built with the assistance of Mr. Steven O'Shea.

In Chapter 4, provides a description of the modelling and testing of the experimental setup. Finite Element Analysis of the experimental setup were performed and compared to experimental results. A noise model of the amplification circuit was created to calculate the resistance required to ensure the thermal noise would be the dominant noise source and to compare the experimental results to the theoretical values. The experimental results were obtained by the author and the finite element analysis of the setup were carried out by the author with the help of Dr. Liam Cunningham.

In Chapter 5, the thermal noise at room temperature was investigated. A thermal gradient was produced across the sample resistor while recording the thermal noise at room temperature and at higher temperatures of $\sim$330 K. Comparisons were then made between the results that were obtained under a thermal gradient and when no gradient was present. The thermal noise measurements were conducted by the author.

Chapter 6 investigates the thermal noise of the thin film resistor at cryogenic temperatures. The issues that arose while operating at cryogenic temperatures and the solutions are discussed. The resistor was cooled down to $\sim$110 K and similarly to chapter 5 the thermal noise was recorded there was a thermal gradient present and also when there was no gradient and the values were compared.

Chapter 7 contains a summary of the conclusions drawn from the work presented in this thesis.

Appendix A contains a copy of the Labview code written to control the heater used to produce the thermal gradients. The code was written by the author with the help of Dr. Giles Hammond.

Appendix B contains a copy of the code used to control the Agilent spectrum analyser and also to automate the recording of the data onto the computer. The code was downloaded from the National Instruments website and modified by the author.

Summary

In 1916, Einstein predicted the existence of gravitational waves in his theory of general relativity. These waves can be described as ripples in the fabric of space-time. Indirect evidence of their existence was discovered by Hulse and Taylor in 1974 through the study of binary pulsars. There are a large number of scientists developing a network of gravitational wave detectors all around the world in an effort to directly measure these waves. Once these waves are detectable, gathering information on the astronomical systems that produce these waves will help scientists to further understand the universe.

Gravitational waves are quadrapole in nature and produce a strain on space. This strain can be imagined as a orthogonal stretching and squeezing of space. The fluctuations in the dimensions of space caused by gravitational waves produce a strain of the order of 10^{-22} in a frequency band of a few Hz to a few kHz. One method of detecting the strain caused by a gravitational wave is using a Michelson Interferometer.

There are currently a number of interferometers operating worldwide. In Germany, the folded 1.2 km GEO600 interferometer has been constructed by a collaboration between University of Glasgow, University of Hannover, Cardiff University and the Albert-Einstein-Intitut in Hannover and Gölm. Another European detector called Virgo was constructed near Cascina, Italy. Virgo is an interferometer with an arm length of 3 km and was constructed by a collaboration involving France, Italy and the Netherlands. There are also two detectors in the United States of America forming the LIGO project. One detectors on a site near Hanford, Washington with an arm length 4 km and another constructed near Livingston Louisiana whos arm length also measures

4 km. A future detector called KAGRA is currently under construction in the Kamioka mines in Japan which is designed to operate at cryogenic temperatures.

The current method of calculating thermal noise in a detector is using the fluctuation-dissipation theorem (FDT) which requires the system to be in thermal equilibrium, meaning that the temperature is constant and there is no heat flow through the system. This is an acceptable assumption for the current room temperature detectors as the thermal gradient is much smaller than the absolute temperature. However, for cryogenic detectors, the thermal gradients will be at a level that is comparable to the absolute temperature, and so this assumption is no longer valid. The work undertaken in this thesis is to assess the validity of the fluctuation-dissipation theorem when under non-thermal equilibrium conditions.

Chapter 1 starts by explaining the nature of gravitational waves, the sources expected to produce detectable signals, the methods of detecting these signals and the noise sources associated with interferometric detectors. Chapter 2 then provides an overview of thermal noise, which is one of the main limiting aspects of detector sensitivity. The fluctuation-dissipation theory is explained as well as the different sources of thermal noise. Finally a brief discussion on non-equilibrium systems is given as a motivation for the work presented in this thesis.

Chapter 3 provides a description and explanation of the experimental setup used in this investigation. The Johnson noise of a platinum thin film resistor is used to investigate thermal noise in a non-equilibrium system at cryogenic temperatures. A small vacuum chamber was built to facilitate inducing a thermal gradient across the resistor, in order to observe if the theoretical values calculated using the FDT coincide with the experimental results. A Labview code used to control the temperature of the resistor using a heater is also described.

Modelling and testing of the experimental setup is described in Chapter

4. Modeling was carried out before the construction of the setup to estimate thermal properties of the apparatus and also to aid in choosing certain aspects of the experiment. A noise amplification circuit was also designed for this experiment and a noise model was produced to create a situation where the thermal noise of the total signal was the dominant noise source.

In Chapters 5 and 6 the thermal noise at room temperature and cryogenic temperature, respectively, are investigated. Issues that arose when attempting to carry out the experiment at cryogenic temperatures, along with the solutions, are discussed. Measurements were taken when a thermal gradient was present and absent and compared to assess the effect of a thermal gradient on the Johnson noise.

The results presented in this thesis indicate that there was no measurable difference between the thermal noise in the presence of a thermal gradient and when the gradient was absent. Despite not seeing an effect, the experiment described in this thesis has the potential to provide much more accurate measurements with some small modifications.

Chapter 1

Gravitational Waves Overview

1.1 Introduction

In 1916, Albert Einstein proposed the existence of gravitational waves in his 'General Theory of Relativity' [1]. These waves can be described as ripples in the curvature of space-time and as a mode of transport for energy as gravitational radiation.

Experiments to detect these waves have been conducted as far back as 1960 when Joseph Weber conceived a resonant bar detector [2, 3]. Despite other scientists being unable to replicate his results, his attempt to measure the strain of a gravitational wave was the birth of a new field of experimental gravitational wave physics. Though not directly detected, there is strong evidence for the existence of gravitational waves through observing the orbital decay of some astronomical systems. In 1993, Hulse and Taylor were awarded the Nobel prize for Physics for their work involving Binary Pulsars. In 1974 they discovered PSR B1913+16 [4], a pulsar together with a neutron star orbiting a common center of mass to form a binary system. In their analysis of the system they discovered that the orbits of the neutron star and the pulsar were decaying, an assumption made by observing the pulse period of the pulsar, shown in figure 1.1. This decaying of the orbits was thought to be due to the emission of energy in the form of gravitational waves, as predicted by Einstein's theory of general relativity. This discovery gave indirect evidence of the existence of

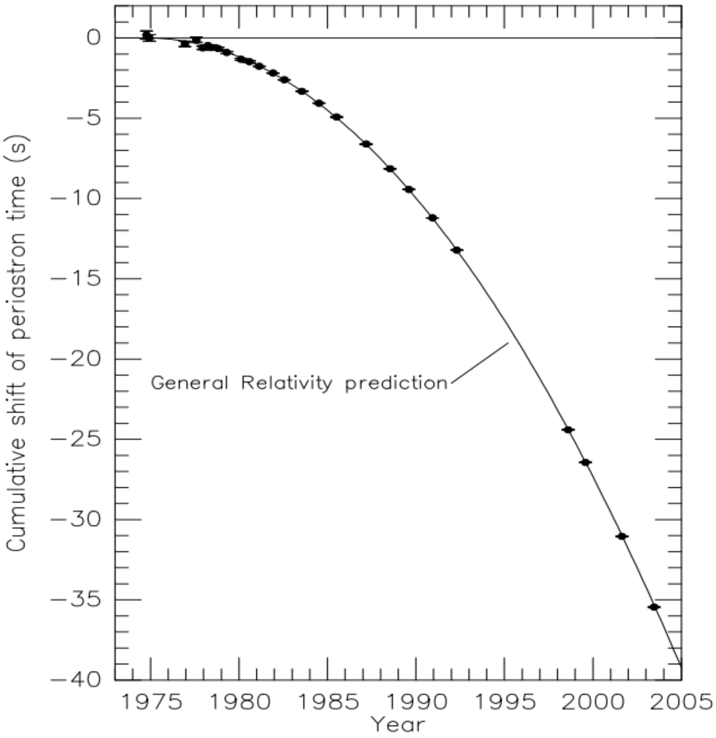

Figure 1.1: A plot of the shift of periastron time of pulsar PSR B1913+16 [4]

gravitational waves [5].

There is currently a worldwide network of interferometric gravitational wave detectors in North America [6] , Europe [7, 8] and future detectors in India [9, 10] and Japan [11]. Currently the network is being upgraded to improve performance and sensitivities. The ability to detect gravitational waves would open up a new area of astrophysics and allow us to investigate aspects of the universe that were previously unaccessible. The nature of black holes could be observed through the gravitational waves produced by these objects and information concerning pulsars and neutron stars could be discovered by studying the gravitational waves emitted from these phenomenon.

This chapter explores the different aspects of gravitational wave research. There will be an explanation of the theory behind Gravitational waves (Section 1.2), the sources that can produce them (Section 1.3), detection methods and the currently operating detectors throughout the world (section 1.4) and finally sources of noise associated with these detectors (section 1.5).

1.2 Theory of gravitational waves

The gravitational force is the weakest of the four fundamental forces. As such gravitational waves are extremely weak and only appear at detectable levels when extreme interactions occur. Gravitational waves are described as being ripples in the curvature of space-time with the curvature being caused by a mass. The greater the asymmetric mass present the larger the curvature of space-time and so the stronger the wave. The strength of the wave is also affected by the velocity of the system itself and as the speed approaches the speed of light, the stronger the wave that is produced.

The effect of gravitational waves on an area of space can be visualised by a two dimensional circle of test particles of diameter L. When a gravitational wave interacts with the particles perpendicular to the plane of the circle, the particles will oscillate in a certain manner. Depending on the amplitude of the wave, the diameter of the circle will increase by ΔL in one axis and decrease by ΔL in the other perpendicular axis. In Fig 1.2 an image of the effect of a gravitational wave of two orthogonal polarisations, h_+ and h_x is shown.

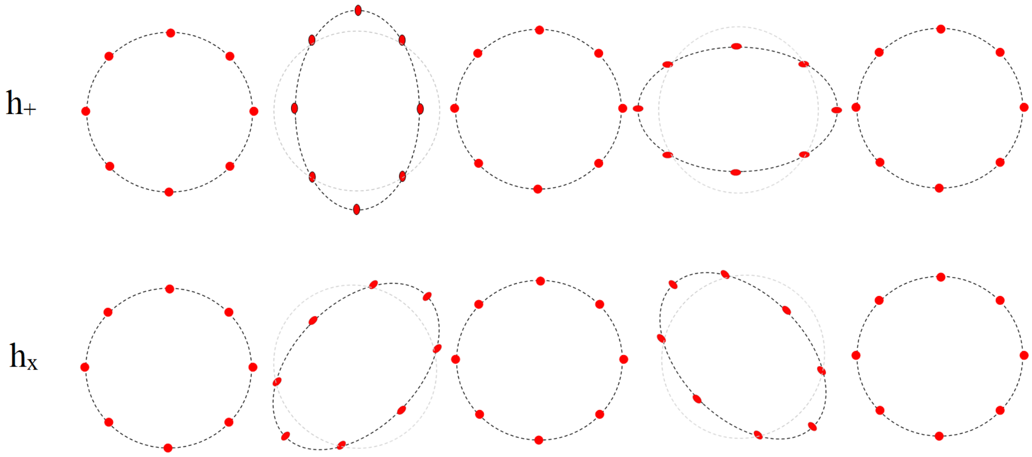

Figure 1.2: The effects of a gravitational wave perpendicular to the plane of a ring of free particles. The top line shows the effects of a + polarised wave and the bottom line shows the effect of a × polarised wave.

Gravitational radiation is different from electromagnetic radiation in that it is quadrupolar in nature and not dipole like electromagnetic radiation.The mass monopole related to gravitational waves represents the mass of a system which is conserved and so does not produce monopole radiation. The mass dipole represents the center of mass of the system and its first derivative represents momentum which is also conserved and so does not radiate. The mass quadrupole is not conserved and can vary with time and so can radiate gravitational waves. This also means that gravitational waves will only be produced by an asymmetrical acceleration of mass [12]. The amplitude 'h' of a gravitational wave is a dimensionless value that can be expressed in the strain that it exerts on the space it is traveling through, given by:

$$h = \frac{2\Delta L}{L}, \tag{1.1}$$

where $\frac{\Delta L}{L}$ is the strain.

1.3 Sources of gravitational waves

There are a number of assumed sources of gravitational waves which would theoretically be strong enough to detect. The following are a few examples.

1.3.1 Binary Systems.

Binary systems are described as two stellar objects orbiting a common center of mass. When these systems involve compact objects such as neutron stars or black holes they are called compact binary systems. These systems are thought to produce gravitational waves which have a large enough amplitude to be measured and are a standard source for aLIGO and Advanced VIRGO. These systems can come in the form of black hole / black hole (BH / BH), neutron / neutron star (NS / NS) and neutron star / black hole (NS / BH) combinations. As mentioned before with pulsar B1913+16, the orbits of the two stars can decay and cause the pulse period of the stars to decrease. This is caused by the system losing energy in the form of gravitational waves with the amplitude of the gravitational wave produced by binary systems estimated to be

$$h \sim 1.5 \times 10^{-19} \left(\frac{f}{1\,Hz} \right)^{2/3} \left(\frac{M_b}{M_\odot} \right)^{5/3} \left(\frac{r}{1\,kpc} \right)^{-1}, \tag{1.2}$$

where f is the frequency of the gravitational wave, r is the distance from the source to the observer and M_b is given by $M_b = (M_1 M_2)^{3/5}/(M_1 + M_2)^{1/5}$ and is also know as the 'chirp mass' where M_1 and M_2 are the masses of each star [13].

1.3.2 Neutron Stars

In the early stages of the formation of a neutron star, the crust of the star will solidify [14]. The shape of this crust is dependent on the forces involved in the dynamics of the star and due to the star spinning rapidly it will take an oblate form. If the angular momentum of the star varies from the preferred symmetry axis this will cause the star to 'wobble' and would produce a gravitational wave. The amplitude of the gravitational wave emitted by the star is given by

$$h \sim 4.2 \times 10^{-24} \left(\frac{ms}{P} \right)^{2} \left(\frac{r}{10\,kpc} \right)^{-1} \frac{I}{10^{45} g\, cm^2} \left(\frac{\epsilon}{10^{-6}} \right), \tag{1.3}$$

where P is the rotation period, r is the distance to the star, I is the moment of inertia and ϵ is the oblateness of the star [13]. For the Crab Pulsar it is thought that $\epsilon \leq 7 \times 10^{-4}$ and h $\sim \leq 10^{-24}$ [15].

1.3.3 Supernovae and Accretion-Induced Collapse of White Dwarfs.

Supernovae are some of the most energetic events known to astronomers. Type Ia supernova can occur in binary systems when a white dwarf star accretes mass from the companion star [16]. When the white dwarf accretes enough mass and starts to approach the Chandrasekhar limit (approximately 1.4 solar masses), carbon fusion ignites and releases a vast amount of energy in a supernova explosion. A fraction of the energy expelled in this explosion is thought to be in the form of gravitational waves.

The amplitude of a gravitational wave produced in this type of supernova is given by

$$h \sim 5\times 10^{-22}\left(\frac{E}{10^{-3}M_{\odot}c^{2}}\right)^{-1/2}\left(\frac{\tau}{1\,ms}\right)^{-1/2}\left(\frac{f_{gw}}{1\,KHz}\right)^{-1}\left(\frac{r}{15\,Mpc}\right)^{-1}, \quad (1.4)$$

where E is the total energy emitted mainly at frequency f_{gw}, τ is the timescale of the waves propagation and the source is at a distance r from the observer [17].

Figure 1.3 shows a graph which shows both the sensitivity curves of various current and future interferometric detectors and the region of the spectrum that various sources are believed to emit at.

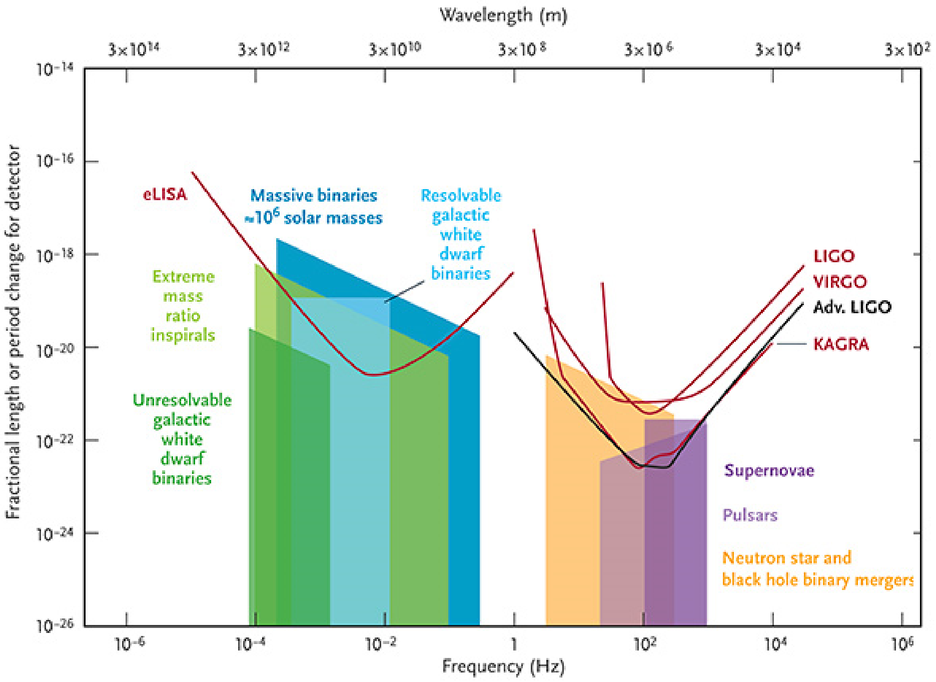

Figure 1.3: A graph showing a sensitivity curves for various detector sensitivities and the regions of the spectrum where sources would produce gravitational waves [18].

1.4 Methods of detection

The first experimental attempts at detecting gravitational waves started in 1960 when Joseph Weber utilised the assumption that strain in a large aluminium bar caused by a gravitational wave could result in electrical polarisation caused by the piezoelectric effect. By measuring these voltages, information concerning gravitational waves could be determined. Though Weber published what he perceived to be positive results, his experiment was repeated a number of times by other groups and always failed to produce any results. Since then there have been a number of different experiments designed by various groups in the US [6] and across Europe [7, 8] in the pursuit of direct detection of gravitational waves.

1.4.1 Resonant Mass Detectors

Developed by Weber in 1969, the resonant mass detector was the first experimental attempt to detect gravitational waves. These bars are designed to be vibrated at specific frequency by an interaction with a gravitational wave. These vibrations were originally measured using piezo-electric elements which produced signals that can be amplified to detectable levels.

Figure 1.4: An image of Weber working on his Resonant detector bar. The piezoelectric sensors can be seen attached to the large Aluminium cylinder.

Various upgrades were made to the original design to improve the sensitivities such as operating at cryogenic temperatures to lower thermal noise and replacing the piezo-electric elements with superconducting transducers to improve the sensitivity of the detectors. MiniGRAIL was a resonant mass antenna located in Leiden University in the Netherlands [19]. This was a spherical mass of a copper/aluminium alloy. This mass was 68 cm in diameter with a mass of 1600 kg. The spherical nature of this detector allowed it to detect gravitational waves arriving from any direction and also allows it to be sensitive to polarisation of the incoming wave. It was designed to resonate at a frequency of 2.9 KHz with an intended operational temperature of 20 mK. It was tested at 5 K and has a strain sensitivity of $1.5 \times 10^{-20}\, Hz^{-1/2}$ with the sensitivity expected to improve by an order of magnitude when the detector is operating at 50 mK. Similar to MiniGRAIL was the Mario Schenberg detector in Brazil [20]. It was also a spherical mass detector made of copper/aluminium alloy with a diameter of 68 cm, a mass of 1600 kg and an intended operating temperatire of 1600 mK. The main difference between these two detectors was that the Mario Schenberg detector used parametric transducers with resonant cavities. The cavities were pumped with a 10 GHz microwave signal that modulated with the oscillations of the transducer allowing the modulations to be analysed. AURIGA was an ultracryogenic resonant bar detector located a the Istituto Nazionale di Fisica Nucleare (INFN) in Italy [21]. This was a resonant bar detector with a 3 m long aluminium bar weighing 2.3 tones. Like MiniGRAIL and Mario Schenberg, it was also designed to operate at ultra low temperatures (< 1 k).

1.4.2 Space-based eLISA

eLISA(Evolved Laser Interferometer Space Antenna) is a planned space project where an interferometer will be launched into a heliocentric orbit 50 million km behind the Earth. The benefits of having an interferometer in space are numerous. The space environment produces a natural vacuum along the arm lengths, the seismic noise and gravity gradient noise are almost eliminated and it also allows for much larger arm lengths than is possible on Earth [22]. The planned launch date is 2034 [23].

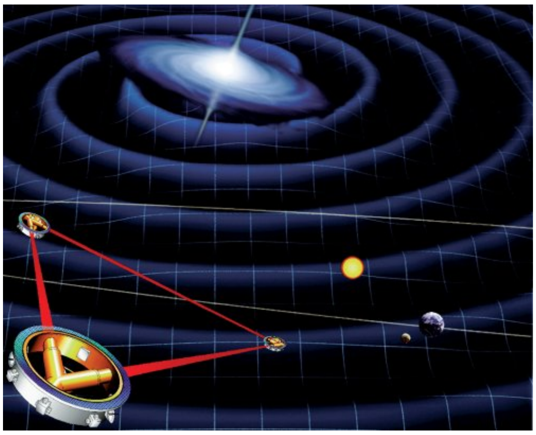

Figure 1.5: An artists impression of the Laser Interferometer Space Antenna(LISA). This detector will orbit around the sun at the same distance as the Earth with an effective arm length of $5 \times 10^9 m$.

The aim of the eLISA project is to create an interferometer with arm lengths of 5 million km arranged in a equilateral triangle with the test masses at the corners of this triangle as shown in Figure 1.5. It is hoped that once operational, eLISA will observe a frequency range of 10^{-4}Hz to 1Hz and to be able to detect gravitational waves produced by coalescence of massive black holes and resolved galactic binaries, objects that are impossible to observe on earth.

1.4.3 Interferometric detectors

Detecting gravitational waves through interferometry was first conceived by Weiss in 1972 [24] where he proposed a Michelson interferometric setup to attempt to replicate Weber's results. These interferometric setups attempt to detect the effects of gravitational waves on the position of test masses. Figure 1.6 shows a simplified schematic of a Michelson interferometer.

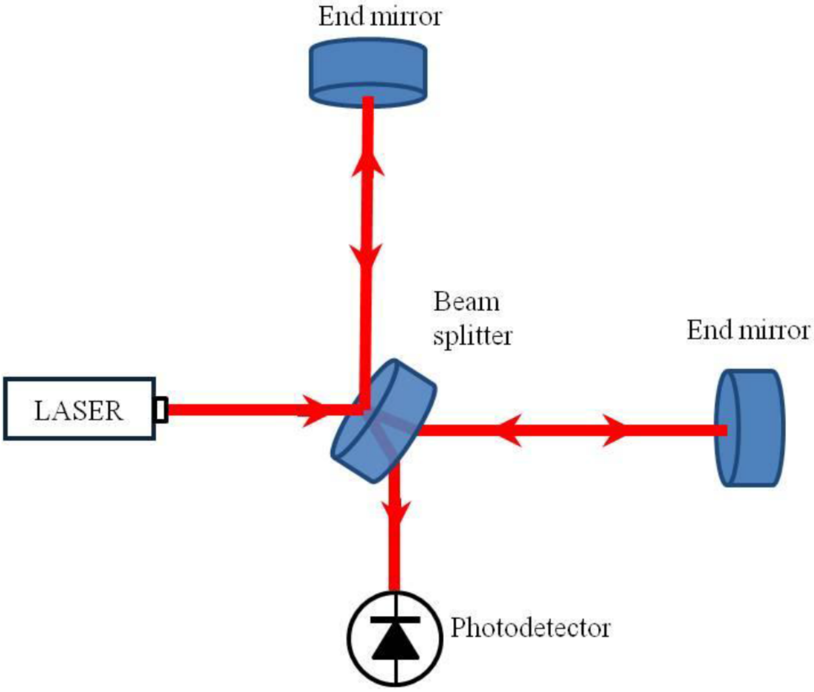

Figure 1.6: A simple schematic of a Michelson Interferometer [25].

A Michelson interferometer operates by observing interference fringes caused by the optical path the laser beam follows. The laser light is passed through a beam splitter where it is partially transmitted and partially reflected into perpendicular arms. The laser light then reflects off a mirror at the end of each arm. Once the light recombines at the original beam splitter an interference effect occurs. By monitoring the change in the interference pattern observed with a detector, normally a photodiode, changes in arm length can be inferred. Currently the arm length of ground based interferometers are limited to 4km due to practical concerns. The cost of longer arm lengths is prohibitively large and also issues such as the curvature of the earth becomes important with longer arms. The optimum arm length is proportional to the frequency of the gravitational wave you want to detect which can be calculated to be [12],

$$L_{optimum} = \frac{\lambda_{gw}}{4}, \tag{1.5}$$

It is possible to increase the effective arm length of an interferometer by using delay line setup in the interferometers. This creates a cavity in each arm length which reflects the light between two mirrors a number of times before it is sent back to the beam splitter. This increases the interferometers effective arm length as shown in figure 1.7.

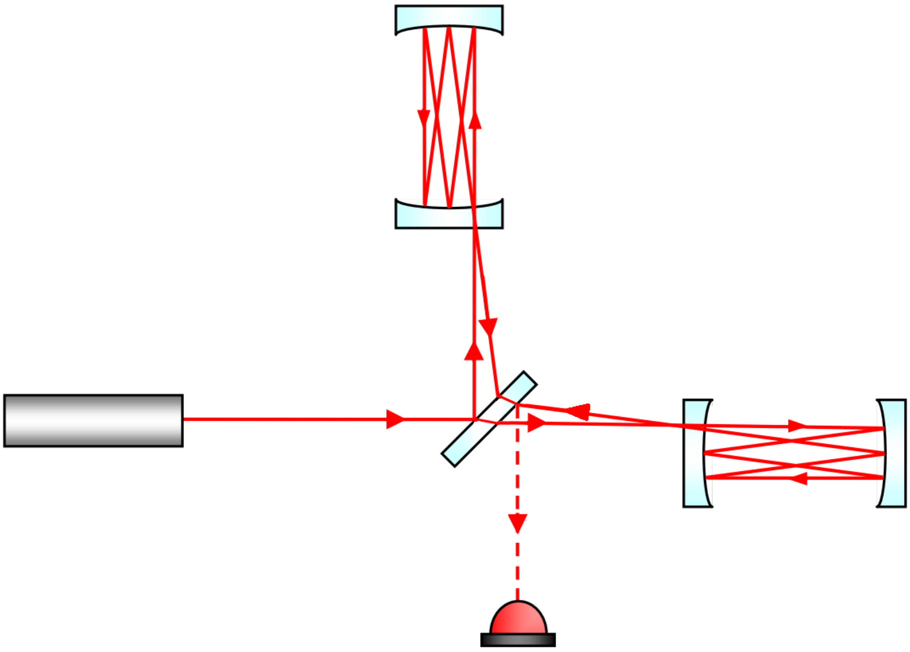

Figure 1.7: A schematic for a delayline setup for a Michelson Interferometer [26].

Another method for increasing the effective arm length is by using Fabry-Perot cavities as shown in Figure 1.8. These cavities work by being held at the carrier frequency of the laser light using a combination of actuation systems and electronic feedback. This causes the laser light to undergo multiple reflections along the same spatial path which increases the arm length similarly to the delay line setup. Despite the additional control systems required to hold the cavities in resonance, the fabry-perot setup does reduce noise introduced by scattered light which is an issue in delay line setup.

Further modifications can be made to increase the sensitivity of the interferometer through processes called power and signal recycling. Power recycling is a technique where a partially reflective mirror is placed between the laser source and the beam splitter as seen in figure 1.9. The purpose of this mirror

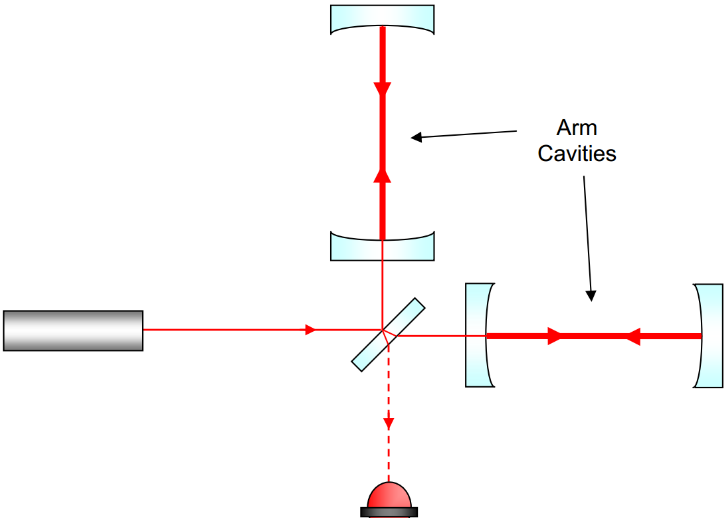

Figure 1.8: A schematic for an interferometer utilising Fabry-Perot cavities [26].

is to re-use the light that is returning from the interferometer to effectively increase the laser power. Signal recycling is similar to power recycling but the mirror is placed between the beam splitter and the detector. This mirror will recycle the laser light that has been altered by a gravitational wave back into the interferometer and so enhance the signal produced by the incoming gravitational wave.

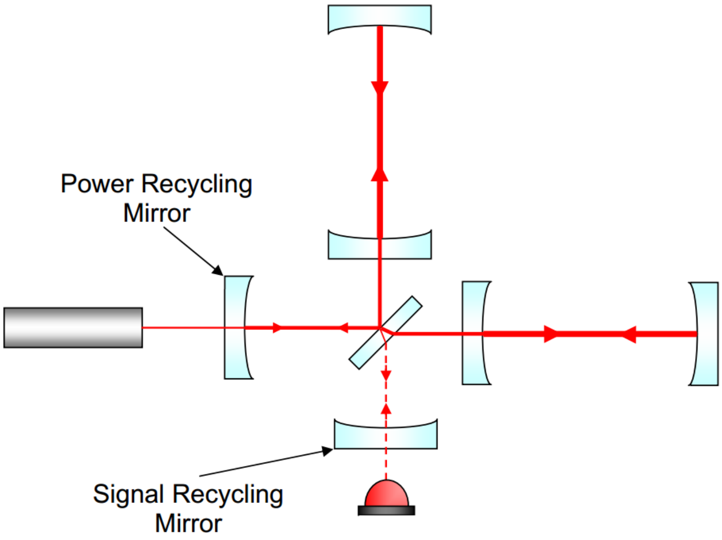

Figure 1.9: A schematic of an interferometer utilising Fabrey-Perot cavities. A signal recycling mirror and a power recycling mirror are also shown [26].

Ground based gravitational wave detectors are predominantly interferometric in design as they are broadband detectors that have superior sensitivities to other designs. There is currently a worldwide network of interferometric gravitational wave detectors which are situated in various different continents as shown in figure 1.10.

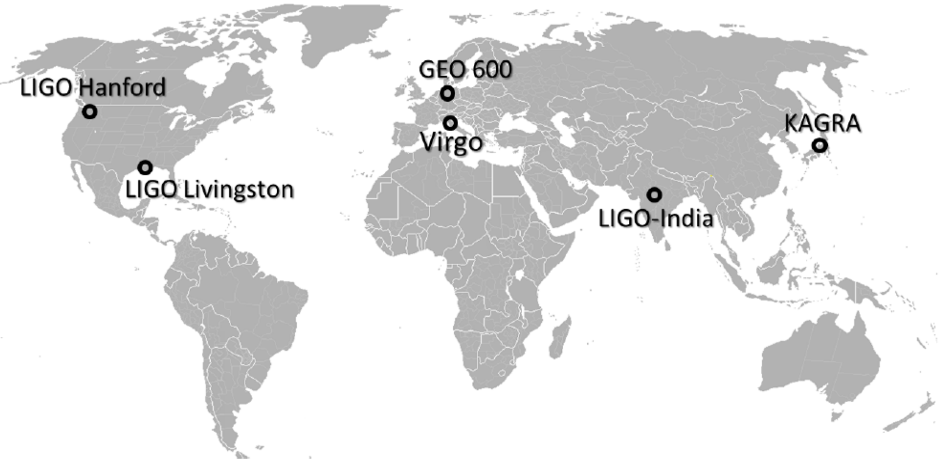

Figure 1.10: An overview of the current network of interferometric gravitational wave detectors [27].

The largest detectors are currently the Laser Interferometer Gravitational-wave Observatory(LIGO) in North America. There are two LIGO detectors, one situated in Livingston, Louisiana with an arm length of 4km and another situated outside Hanford, Washington also with a 4 km arm length. Currently the LIGO detectors are being upgraded to Advanced LIGO (aLIGO) to improve the sensitivity of the detectors. These upgrades [28] include an increase in size and weight of the suspension test mass elements which reduces thermal noise contributions and also lowers the radiation pressure noise to be comparable with the thermal noise. These upgrades allowed aLIGO to reach an amplitude strain sensitivity of $\sim 10^{-23} Hz^{-1/2}$ at a frequency of $\sim 100\, Hz$ [6]. There is the a future LIGO observatory being built in India called LIGO-India. Once this detector is functioning it it will be possible to localise the source of gravitational-wave signals to a few square degrees using only gravitational wave detectors [29].

Currently in Europe there are two detectors, GEO600 which is a German-British collaboration situated in Hannover, Germany and Virgo which is an Italian-French collaboration situated near Piza in Italy. The GEO600 detector is a 600m arm length interferometer which uses folded arms to produce an effective arm length of 1.2km. Despite not using a Fabry-Perot cavity GEO600 does utilise dual recycling, which consists of both signal and power recycling which allows the detector to achieve a peak sensitivity of $\sim 4 \times 10^{-22} Hz^{-1/2}$ [30] at a frequency of around 400 Hz. GEO600 is being upgraded in a project called "The GEO-HF Project". This involves a number of upgrades such as increasing the bandwidth of the signal recycling cavity and increasing the laser power on the recycling cavity from 3 W to 20 W to increase the sensitivity of GEO600 [31].

Virgo has a 3km arm length and is similar to LIGO in that it utilities both Fabry-Perot cavities and power recycling. It differs from LIGO in the fact that it has additional seismic isolation system called the super attenuator. This involves suspending the mirrors on an elastic suspension which filters out the mechanical vibrations in all degrees of freedom which allows Virgo to perform better at lower frequency ranges and produce an expected sensitivity of $\sim 4.5 \times 10^{-22} Hz^{-1/2}$ at a frequency of $\sim 260\, Hz$ [32]. Advanced Virgo is an upgrade to the Virgo detector with the intended goal of improving the sensitivity by an order of magnitude. To achieve this improvement many of the subsystems are being upgraded including upgrading the optical components to a dual recycled interferometer, new larger mirrors and an increase to the laser power [33].

In Japan the Kamioka Gravitational Wave Detector (KAGRA) is currently bring built. KAGRA is planned to be a Michelson interferometer setup with Fabrey-Perot cavities of arm length 3km and dual recycling. The main difference with KAGRA is that the test masses will be cryogenically cooled down to

20 K to reduce thermal noises. With this addition to KAGARA the sensitivity is expected to be $\sim 3 \times 10^{-24} Hz^{-1/2}$ at ~100 Hz [34].

1.5 Noise Sources

In order for the detectors to reach the sensitivities required to observe the effects of gravitational waves, the sources of noise must be accounted for in the design of the interferometers. Sources such as photon shot noise, seismic noise and thermal noise are important to understand. Figure 1.11 shows the projected sensitivity of aLIGO for each noise source. A number of these sources will be discussed in this section.

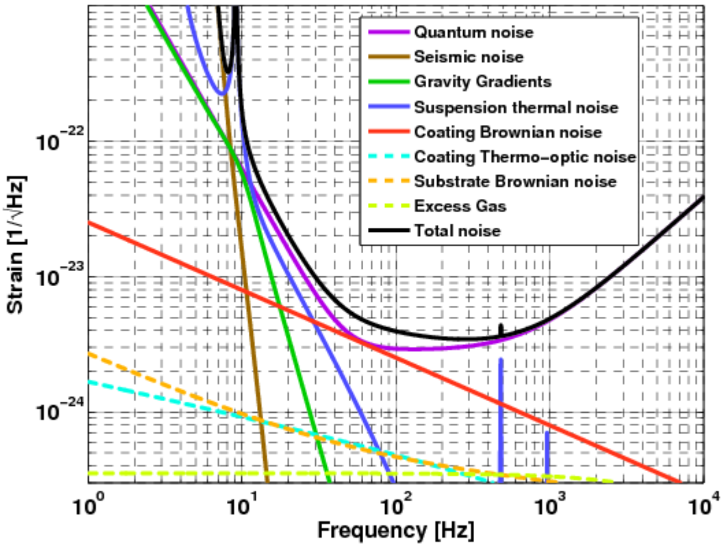

Figure 1.11: A plot of the projected noise sensitivity of aLIGO [35].

1.5.1 Gravity Gradient Noise

Gravity Gradient Noise is caused by seismic waves passing through the ground close to the interferometric detector. These waves cause density variations under the test masses. This will alter the gravitational forces acting on the mirrors and can cause effects on the mirror that can mimic the stochastic background of gravitational waves. As such this effect is a source of noise that needs to be accounted for [36]. The RMS motion of the test masses due to this effect can be calculated using

$$\tilde{x}(\omega) = \frac{4\pi G\rho}{\omega^2}\beta(\omega)\tilde{W}(\omega), \tag{1.6}$$

where ρ is the earth's density near the interferometer, G is the gravitational constant, ω is the angular frequency of the seismic spectrum, $\beta(\omega)$ is a dimensionless reduced transfer function that takes into account the movement of the test masses in addition to the reduction due to the seperation of the test masses and the earths surface and $\tilde{W}(\omega)$ is the displacement rms-averaged over 3-dimensions [37]. There are schemes being developed that attempt to compensate for this noise by estimating fluctuations in the local Newtonian gravitational field and subtracting these perturbations from the data [38].

1.5.2 Seismic Noise

Seismic Noise is caused by vibrations of the ground. These can be man-made through nearby traffic, trains, or movement close to the detector. Seismic noise can also come from natural sources such as earthquakes and waves hitting the shore(microseismic noise). The level of the seismic disturbances can be minimised by choosing the location for the interferometer to be in a seismically quiet area and far from urban locations.

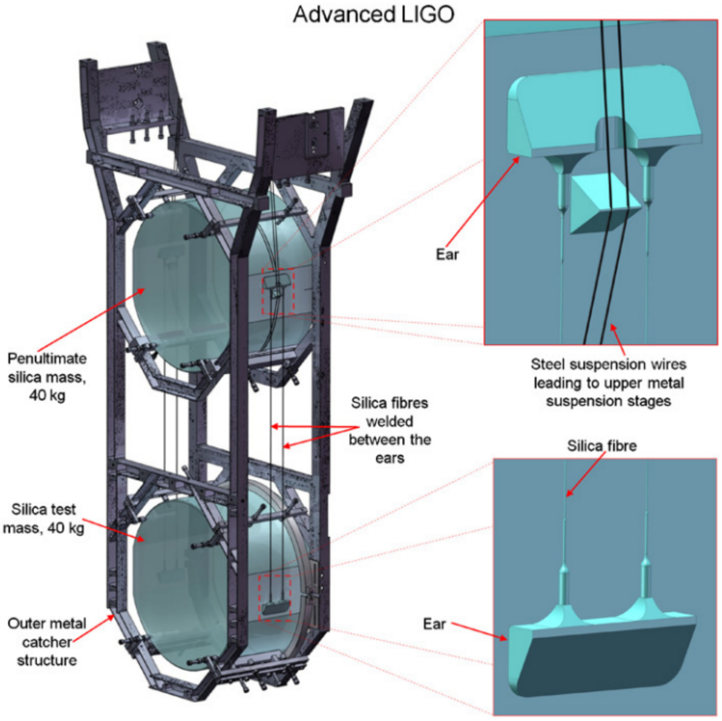

Figure 1.12: An image showing a section of the suspension design for aLIGO. The penultimate mass allows for further reduction in the seismic noise [39].

To further reduce seismic noise the optical elements are suspended using a multi-stage pendulum suspension to further seismically isolate the components of the interferometer [39]. Figure 1.12 shows the lowest section of the suspension design for aLIGO to seismically isolate the test masses.

1.5.3 Quantum Noise

1.5.3.1 Photon Shot Noise

Photon shot noise occurs at the output of the interferometer and is due to a fluctuation of the number of photons arriving at the photodetector. From Poisson statistics we know that for N traveling through the beam-splitter, there is an uncertainty of $\sqrt{N}$ in the number of photons in each arm of the interferometer. This in turn gives rise to a source of noise in the photodetector which limits the sensitivity of the detector. To reduce this noise the ideal solution would be to increase the laser power but this has the additional effect of increasing the radiation pressure on the elements which increases their noise due to low frequency motions. As such the laser power must be tuned to minimise the noise from both radiation pressure and photon shot noise. The shot noise limited sensitivity of a delay-line design interferometer is given by [40],

$$h_{shot}(f) \approx \left(\frac{h\lambda}{2\epsilon I_o c}\right)^{\frac{1}{2}} \frac{f}{sin(\pi\tau)} \frac{1}{\sqrt{Hz}}, \tag{1.7}$$

where h on the right hand side is Planck's constant, λ is the wavelength of light, ϵ is the quantum efficiency of the photodetector, I_o is the power of the input laser, c is the speed of light, f is the bandwidth of the detector and τ is the storage time.

1.5.3.2 Radiation Pressure Noise

Radiation Pressure noise arises from the momentum carried by the photons and which is imparted to the test masses. When the laser light is seperated in the beamsplitter there is a statistical uncertainty in the distribution of the photons into each arm. This variation in the number of photons, N in each arm results in a proportional $\sqrt{N}$ fluctuating force in the radiation pressure. For a simple Michelson interferometer, the power spectral density of the fluctuating motion of each test mass m due to the fluctuating radiation pressure at angular frequency ω is,

$$\delta x^2(\omega) = \left(\frac{4Ph}{m^2\omega^4 c\lambda}\right) \tag{1.8}$$

where P is the laser power at wavelength λ, h is Planck's constant and c is the speed of light [37].

1.5.4 Standard Quantum Limit

Due to photon shot noise decreasing with increased laser power and radiation pressure noise increasing with laser power there is a fundamental limit to the quantum noise. This is known as the Standard Quantum limit(SQL). Figure 1.13 demonstrates the effect of increasing the laser power.

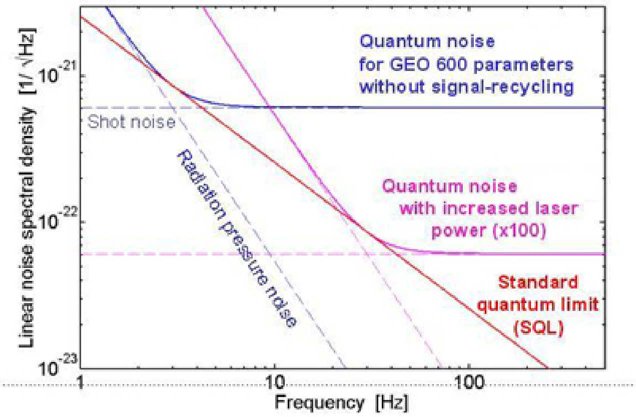

Figure 1.13: A plot demonstrating the effect of increasing the laser power in GEO600 [41].

From this plot it can be seen that for a cetain operational frequency of a gravitational detector, theres is an optimum laser power to minimise both of these quantum noise sources.

1.5.5 Thermal Noise

Thermal noise arises from the random motion of atoms due to their thermal energy. This occurs in the test masses and in the suspension elements of the interferometer and is calculated using the fluctuation-dissipation Theorem [42]. Sources of thermal noise include Brownian noise which is a product of the brownian motion of the atoms in the material in question and thermoelastic noise which is due to the small deformations in the material caused by thermal expansion of different areas of the material. To reduce thermal noise in the future gravitational wave detector KAGRA, the components of the detector will be cooled to cryogenic temperatures. As thermal noise is dependant on the temperature of the components, reducing the temperature will also reduce the thermal noise. Further methods are being implimented in upgrades to aLIGO, advanced VIRGO and GEO, using fused silica fibres in the suspension stage to create a quasi-monolithic suspension stage, shown in figure 1.12. By careful design of the geometry of these fibres, it is theoretically possible to cancel out thermoelastic noise in the silica fibers [43]. Chapter 2 will explore these aspects of thermal noise in more detail.

1.6 Conclusion

Scientists have been searching for gravitational waves for several decades. There has been a variety of methods for attempting to detect these elusive waves, but the most recent detectors are large scale interferometers. There are a large number of groups all over the world collaborating to both design and build these detectors in various countries. Through collaboration the gravitational wave community has managed to reach sensitivities that should allow direct observations of gravitational waves by 2016/17 using these advanced detectors. More research is still being conducted and improvements are still being made to current detectors. Future detectors are also being constructed such as KAGRA in Japan which is designed to be operated at cryogenic temperatures in order to further reduce noise. There are still areas that are not well understood such as the effect of non-equilibrium conditions in these cryogenic detectors, therefore more research is required in order to optimise these detectors. Once we have the ability to detect and study these waves we will gain a new window in which to observe the universe and gain a better understanding of the cosmos.

Chapter 2

Thermal Noise

2.1 Introduction

Thermal noise is one of the most significant sources of noise in gravitational wave detectors. It manifests mainly through Brownian motion resulting from the random movement of the atoms in the experimental setup, and also through thermoelastic noise. In this chapter the derivation of the mechanical form of the fluctuation-dissipation theorem will be explained and related to thermal noise involved in gravitational wave interferometers. In the second part of this chapter, the electrical form of the fluctuation-dissipation theorem will be explained and related to the processes that will be further investigated in this thesis.

2.2 Brownian Noise

In 1827, botanist Robert Brown observed pollen grains moving in water but could not determine the mechanism which was causing these grains to move [44]. This phenomenon was not fully understood until 1905 when Einstein demonstrated that this movement was caused by collisions with the surrounding water molecules [45]. Einstein also demonstrated that the pollen grains were losing kinetic energy through friction with the water, demonstrating that fluctuations in the position of an object were related in some way to the dissipation of energy. This idea was further developed by Callen and Welton in

1951 into the fluctuation-dissipation theorem [46]. The theorem states that any linear system in equilibrium undergoing dissipation will have fluctuations of measurable parameters. This provides a method of calculating the thermal displacement noise in gravitational wave detectors.

2.3 Fluctuation-dissipation theorem

The fluctuation-dissipation theorem (FDT) states that any linear system in equilibrium undergoing dissipation will have fluctuations of measurable parameters. It can be used to model any thermodynamical system but is used here to calculate displacement noise in gravitational wave detectors. In a mechanical system, it relates the power spectral density of the mechanical driving force $S_f(\omega)$ to the displacement part of the mechanical impedance $\Re[Z(\omega)]$ i.e the real part. This can be shown by the following equation [46],

$$S_f(\omega) = 4k_bT\Re[Z(\omega)]. \tag{2.1}$$

By defining the mechanical impedance as F/v, where F is the force acting on an object and v is the velocity of said object, the fluctuation-dissipation theory can be written in a form that gives an expression for the spectral density of thermal displacement $S_x(\omega)$,

$$S_x(\omega) = \frac{4k_bT}{\omega^2}\Re[Y(\omega)] \tag{2.2}$$

where $Y(\omega)$ is the mechanical admittance ($Y(\omega) = 1/Z(\omega)$). This allows the fluctuation-dissipation theorem to calculate the amplitude spectral density of the thermal noise from the real part of the mechanical impedance

2.4 Sources of Dissipation

2.4.1 External sources of Dissipation

In gravitational wave detectors there are a number of external sources of noise which contribute to the total thermal noise. Examples of these are:

- Frictional damping - where the suspension elements meet the test mass and at the suspension point, known as “slip-stick” losses [47];
- Recoil damping - Energy dissipating into the support structure from the suspension [48];
- Gas damping - friction caused by residual gas molecules colliding with the suspension elements providing a viscous damping effect [48].

These and other external sources should be considered in the design of the detector and minimised as much as possible across the operational frequency of the detector.

2.4.2 Internal Sources of Dissipation

Once the external noise sources are sufficiently minimised then the noise and damping effects produced by friction inside the mirrors and suspension fibres becomes important. Internal damping occurs in a material that is said to exhibit anelasticity. An ideal elastic material obeys Hooke’s law which states that a force exerted on a material causes a stress, σ. This stress results in an instantaneous strain, ϵ, inside the material. In an anelastic material this process is not instantaneous and instead reaches a new equilibrium state after a finite relaxation time. This means that a periodic stress that is applied to an anelastic material at frequency ω will produce a periodic strain at the same angular frequency as the stress but with a phase lag of ϕ with respect to the applied stress. This phase lag is known as the mechanical loss factor (or loss angle) of the material.

This mechanical loss can be caused by a number of processes in the material, for example, stress can cause changes in temperature at different points inside the material. This will cause a heat flow and require time to return to a state of equilibrium. Because the mechanical loss can be dependant on the temperature and frequency of the stress, it is sometimes written as $\phi(\omega, T)$ to denote that the loss is dependant on these factors.

Any resonant mode of the suspension, e.g pendulum or violin mode of the suspension fibres or the internal modes of the test mass, can be described as a damped harmonic oscillator represented as a mass, m, suspended on a spring of constant, k. The mechanical loss can be incorporated into this model by adding an imaginary term into the spring constant [49] producing the equation,

$$F_{\text{spring}}(\omega) = -k(1 + i\phi(\omega))x, \tag{2.3}$$

where F_{spring} is the force of the spring and x is the displacement of the spring from its equilibrium position.

Using the equation of motion, an expression for the motion due to the internal thermal driving force $F_{\text{thermal}}(\omega)$ can be obtained,

$$F_{\text{thermal}}(\omega) = m\ddot{x} + k(1 + i\phi(\omega))x, \tag{2.4}$$

which can also be expressed in terms of velocity,

$$F_{\text{thermal}}(\omega) = i\omega m v - i\frac{k}{\omega}(1 + i\phi(\omega))v. \tag{2.5}$$

The fluctuating force $F_{\text{thermal}}(\omega)$ is divided by velocity to obtain an expression for impedance, such that,

$$Z(\omega) = i(\omega m - \frac{k}{\omega}) + \phi(\omega)\frac{k}{\omega}. \tag{2.6}$$

The admittance can then be calculated to be,

$$Y(\omega) = \frac{1}{Z(\omega)} = \frac{\frac{k}{\omega}\phi(\omega) - i(\omega m - \frac{k}{\omega})}{(\frac{k}{\omega}\phi(\omega))^2 + (\omega m - \frac{k}{\omega})^2}, \tag{2.7}$$

This can then be substituted into the fluctuation-dissipation theorem (Equation 2.2) to obtain the power spectrum of thermal motion,

$$\begin{aligned} S_x(\omega) &= \frac{4k_bT}{\omega^2}\Re[Y(\omega)], \qquad (2.8) \\ &= \frac{4k_bT}{\omega^2}\frac{\frac{k}{\omega}\phi(\omega)}{(\frac{k}{\omega}\phi(\omega))^2 + (\omega m - \frac{k}{\omega})^2}. \qquad (2.9) \end{aligned}$$

This form of the fluctuation-dissipation theorem shows that the power spectral density thermal noise can be calculated when the temperature, mass and resonant frequency of the material is known.

2.5 Interferometer Thermal Noise Sources

Resonant frequencies will occur due to the geometry of the suspension structure and are excited by the the thermal motion of the atoms in the materials to driving these resonances. This means care must be taken regarding where the resonant frequencies lie with-respect-to the frequency range of the detector band. Materials with a high Q-factor, the inverse of mechanical loss, allow the energy contained in them to be focused in the resonant modes. This reduces the off resonance noise and providing a low noise frequency range for the detector to operate in.

2.5.1 Pendulum Modes

The test masses in interferometers are suspended to reduce the seismic noise. This suspension design must take into account the pendulum modes which exist in this design. These pendulum modes, if excited in the direction of the arm length, can change the position of the mirror and so limit the dynamic range of the interferometer. This can be minimised by designing the suspension so the resonant frequencies occur outside the operational frequency of the detector [50]. The frequency of the pendulum mode can also be lowered by increasing the length of the suspension fibres.

2.5.2 Bounce Mode

Vertical bounce modes occurs as another consequence of suspending the test masses. The test mass will bounce in a vertical direction which will change the position of the laser beam on the mirror. If the arm lengths of an interferometer are long enough then the test mass will not hang parallel to the beam splitter due to the curvature of the earth. When the test masses are parallel with the beam splitter, the directions of the local gravitational accelerations are not parallel and so can introduce a horizonal motion of approximately 0.1% of the effect of the vertical component of the bounce mode [51]. This is illustrated in figure 2.1. The suspension setup can be designed so, like the pendulum mode, it can occur outside the operational frequency of the detector.

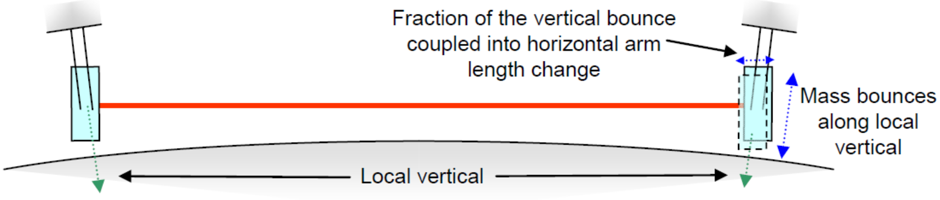

Figure 2.1: An illustration of how the bounce mode couples into horizontal motion of the test mass. [52].

2.5.3 Violin Modes

Violin modes occur in the suspension fibres of the structure and unfortunately lie in the operational frequency bandwidth of the detectors, which occurs at 450 Hz for aLIGO . Due to the suspension being designed to minimise the loss in the system, most of the thermally induced motion is concentrated in a small bandwidth centring on the resonant frequency. This means that the resonant frequencies are most likely the only frequencies to contribute substantially to the total thermal noise level. Since these peaks are narrow, it allows for them to be removed from the signal [50].

2.6 Thermoelastic Noise

Thermoelastic noise occurs in the suspension fibres [53] and also in the test masses and mirror [54]. This noise occurs due to statistical thermal fluctuations in the material. This results in movement of the mirror surface which is due to the coefficient of thermal expansion, α, of the substrate material. By assuming a half-infinite (a large mirror size compared to the laser beam diameter) at room temperature, the thermoelastic noise, $S_{\mathrm{TE}}(\omega)$, can be expressed as [54],

$$S_{\mathrm{TE}}(\omega) = \frac{16}{\pi}\frac{k_B T^2 \alpha^2 (1+\nu)^2 \kappa}{\rho^2 C^2 r_0^3 \omega^2}, \tag{2.10}$$

where k_B is the Boltzmann's constant, T is the temperature of the material, ν is Poisson's ratio, κ is the thermal conductivity, ρ is the density, C is the specific heat capacity and r_0 is the radius of the laser beam when the intensity has dropped to $1/e$ of the maximum intensity.

From the equation above, it can be seen that the dissipation is greater for materials with a larger coefficient of thermal expansion and as such is an important property to consider when designing suspension fibers.

2.7 Combined thermal noise in detectors

In order to estimate the sensitivity of a gravitational wave interferometer, the thermal noise contributions from all sources must be combined. This includes noise from suspension fibers, reflective coatings and internal noise sources in the test masses. Figure 2.2 shows an expected thermal noise value plot of the aLIGO interferometer.

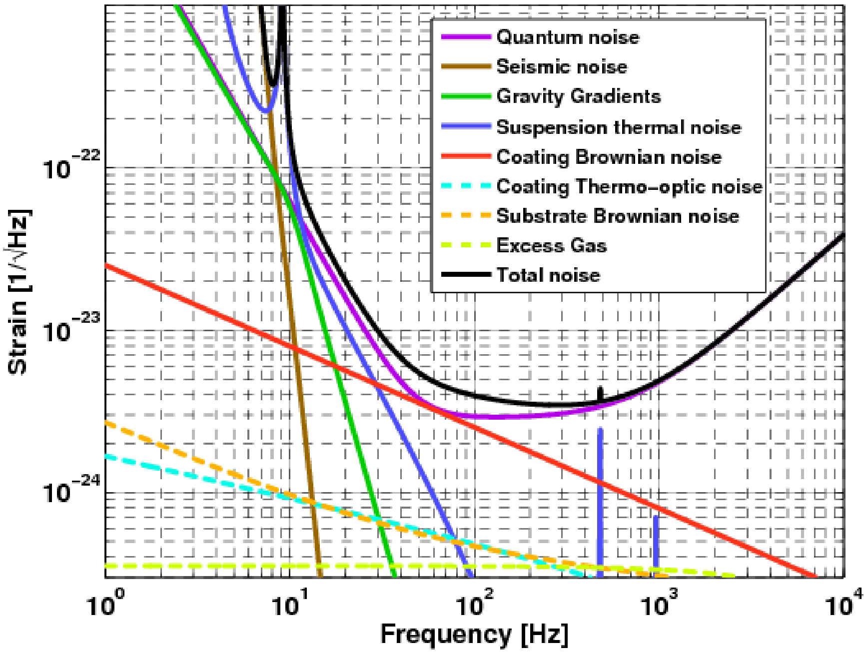

Figure 2.2: A plot of the projected noise levels in aLIGO [35].

2.8 Johnson Noise

In 1926, Johnson measured statistical fluctuations of electrical charge in a resistor [55]. Further discussions with Nyquist [56] then led to the development of the idea of Johnson-Nyquist noise. This noise occurs in electrical conductors where the charge carriers in the circuit are thermally agitated and produce electronic noise regardless of any applied voltage.

In order to derive an expression for Johnson noise, a hypothetical circuit containing a resistor with two terminals connected to either side of a capacitor, shown in figure 2.3, is utilised.

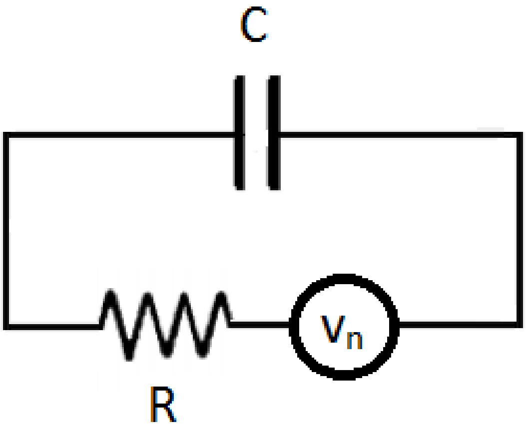

Figure 2.3: A circuit diagram showing the circuit setup for the alternate derivation of Johnson noise

Assuming thermal equilibrium, a Boltzmann distribution can be used to describe the probability P of a system having energy E to be,

$$P(E) \propto e^{\frac{-E}{k_B T}}, \tag{2.11}$$

where k_B is the boltzmann constant and T is the temperature of the system. Using this distribution and an expression for the energy stored in a capacitor, $\frac{1}{2}CV^2$, the probability of finding a voltage between V and $(V + dV)$ can be expressed as,

$$dP = K_0 e^{-\frac{CV^2}{2k_B T}} dV, \tag{2.12}$$

where K_0 is a normalisation constant, C is the capacitance, R is the resistance, k_B is the Boltzmann constant and T is the temperature. By using the change of variables $x^2 = \frac{CV^2}{2k_bT}$, integrating between ∞ and -∞ and setting the integrated probability to 1, the value of K_0 can be calculated to be,

$$K_0 = \sqrt{\frac{C}{2\pi k_B T}}. \tag{2.13}$$

This can be substituted into equation 2.12 and integrated from $-\infty$ to ∞ to gain an expression for the mean square voltage,

$$\overline{V^2} = \sqrt{\frac{C}{2\pi k_B T}} \int_{-\infty}^{\infty} \mathrm{V}^2 \mathrm{exp}(-\frac{\mathrm{CV}^2}{2\mathrm{k_B T}})\, \mathrm{d}V. \tag{2.14}$$

By performing the same change of variable for this equation it can be reduced down to,

$$\overline{V^2} = \frac{k_B T}{C}. \tag{2.15}$$

The next step of this derivation is to gain an expression for the mean square voltage, $S_v(0)$, of the source v_n per interval of frequency. The mean square voltage of the circuit can be expressed as,

$$|V_c| = \underbrace{|v_n|^2}_{S_v(0)} \frac{1}{1 + (\omega RC)^2}, \tag{2.16}$$

of which the derivative is then taken,

$$d\overline{V_c^2} = \frac{S_v(0) df}{1 + (\omega RC)^2}. \tag{2.17}$$

By integrating and using the change of variable, $x = \omega RC$, the equation then becomes,

$$\overline{V_c^2} = \frac{S_V(0)}{2\pi RC} \int_0^{\infty} \frac{\mathrm{dx}}{1 + \mathrm{x}^2} \tag{2.18}$$

which then can be expressed in the form,

$$\overline{V_c^2} = \frac{S_V(0)}{4RC}. \tag{2.19}$$

Equating equation 2.19 to equation 2.15 and rearranging gives the equation,

$$S_v(0) = 4k_BTR. \tag{2.20}$$

It can be seen that equation 2.20 is independant of frequency as this equation is measured across the entire frequency spectrum. By specifying a frequency bandwidth, $S_v(0)\Delta f$ is $|v_n|^2$ across the frequency bandwidth of Δf, so taking this into account, equation 2.20 then becomes,

$$v_n = \sqrt{4k_BTR\Delta f}, \tag{2.21}$$

which is the equation for Johnson noise.

2.9 Non-Equilibrium Systems

The fluctuation-dissipation theorem is a very useful tool when investigating thermal noise in a system but it is formed assuming the system is in thermal equilibrium, meaning that the temperature is constant and there is no heat flow through the system. In current gravitational wave detectors, the operational temperatures can be significantly larger than the thermal gradients present allowing the assumption that the system is in equilibrium. Future gravitational wave detectors such as KAGRA [34], the 3rd generation proposal, the Einstein telescope [57] and possible upgrades to LIGO [42] are all planned to operate at cryogenic temperatures. In this situation the thermal gradients across materials will be comparable to the operational temperature of the system. This prevents the previous assumption being valid and as such, the system can no longer be descibed as being in equilibrium. This brings into question the validity of the FDT in non-equilibrium systems. Despite the large volume of theoretical work conducted, there has only been a small number of experiments to investigate this question [58–60]. This thesis will describe an experiment designed to investigate the validity of the FDT in a non-equilibrium system. As the FDT was formalised by Nyquist and Johnson using an electrical system, this experiment will observe the johnson noise of a platinum thin film resistor while under the effects of a thermal gradient at cryogenic temperatures.

2.10 Conclusion

Thermal noise is an important factor in the construction of gravitational wave detectors. Thermal coating noise is now the main limiting factor to the sensitivity of current detectors. Using the fluctuation-dissipation theorem it is possible to estimate the thermal noise for a variety of sources at thermal equilibrium. Future detectors are planned to operate at cryogenic temperature to further reduce the thermal noise and so increase the sensitivity of the interferometers, but this would mean that the thermal gradients present in the materials will be large compared to the absolute value of the temperature and so can no longer be assumed to be in thermal equilibrium. Thus this experiment and others [58] are underway to investigate if the fluctuation-dissipation theorem still holds under thermal non-equilibrium conditions.

Chapter 3

Experimental setup

3.1 Introduction

The aim of the experiment was to investigate the thermal noise in a thin film platinum resistor at cryogenic temperatures. This was carried out by maintaining a constant temperature across the resistor, and also with a large thermal gradient relative to the absolute temperature of the resistor to investigate wether or not the fluctuation-dissipation theory, explained in chapter 2, holds when the system is not in thermal equilibrium. In this chapter, the experimental setup will be discussed. There were a number of factors that were important to consider in the design of the experiment, such as minimising the additional noise from external sources and circuit components in order to maintain the thermal noise as the dominant noise source. Another important factor was the careful control of the heaters to hold the resistor at the required temperatures and thermal gradients.

3.2 Apparatus

3.2.1 Vacuum Chamber

The vacuum chamber used to build this experiment was designed to allow for a copper bar to pass into the chamber without breaking the vacuum. The copper bar also passed outside the chamber as a means of cooling the system.

Another requirement was a sufficient number of access points for electrical connections to be made between the interior and exterior of the chamber. This provided the means for controlling a heater, measuring the internal thermometers for monitoring thermal gradients and connecting the sample resistor to the amplification circuit.

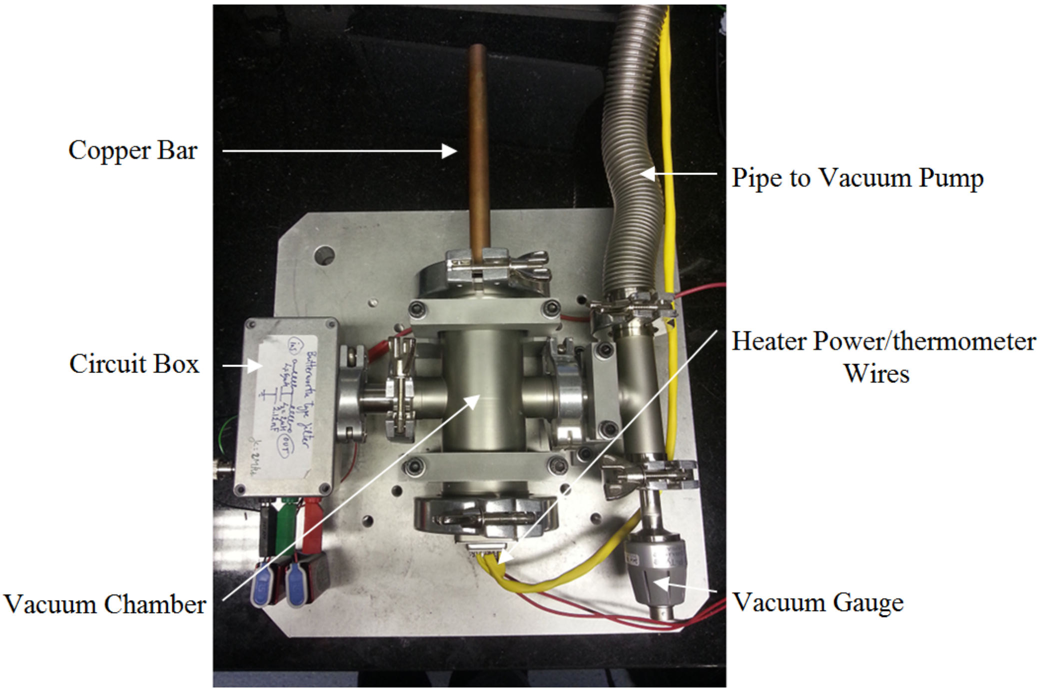

Figure 3.1: A picture of the experimental setup with labels indicating the various sections of the setup.

Figure 3.1 shows the vacuum setup used; one cross piece with a tee piece attached to one side and the connection to the circuit attached to the other side. A Varian 8H-110 rough vacuum pump that reached a pressure of ∼0.7 mbar was used to evacuate the chamber. The large section was used to house the copper bar with flanges either side; one holding the copper bar and the other with a 15 pin through connector for the wires for two PT1000 thermometers, used to monitor the resistor temperature, and the power cables for one of the heaters. From the tee piece, one side was the outlet connection where the air would be pumped out and the other was used for a magnetron vacuum gauge to monitor the pressure inside the chamber. The flange holding the copper bar was originally a blank flange where a hole the diameter of the copper bar was drilled. The bar was then welded into place. This facilitated the bar used to be one solid piece of copper, in order to aid heat flow into and out of the chamber, while still maintaining the seal on the chamber. Another modification was made to a flange beside the circuit box. In a further attempt to prevent any additional noise being introduced into the system, the wire connecting the thin film resistor inside the chamber to the circuit sitting outside the chamber was kept as one continuous piece of coaxial cable. A small hole was drilled in the blank flange, large enough to allow the coaxial cable to pass through and then sealed using an epoxy resin.

During initial testing, this vacuum was adequate for room temperature testing. When the experiment proceeded to cryogenic temperature tests a lower vacuum was required. An Agilent TV-301 Navigator turbo pump was attached to the chamber and used to achieve a vacuum of $\sim 5 \times 10^{-4}$ mbar.

3.2.2 Circuit

As the value of noise that was expected for the platinum resistor was of the order of a few $nV/\sqrt{Hz}$, an amplification circuit was needed to raise the noise level to a detectable range. The circuit was designed using surface mounted components to keep the circuit board as small as possible with the intention of placing the board inside the vacuum chamber. When this was put into practice, excess noise was seen when the copper bar was heated to higher temperatures. This implied there was an issue with a thermal exchange between components inside the chamber and the circuit board. To prevent this, it was decided to separate the components and the copper bar such that there is no thermal link between the two. Figure 3.2 shows a schematic of the final design for the circuit.

The thin film resistor was connected between ground and the input of the circuit using a single core coaxial wire. The signal was then fed through an initial buffer amplifier.

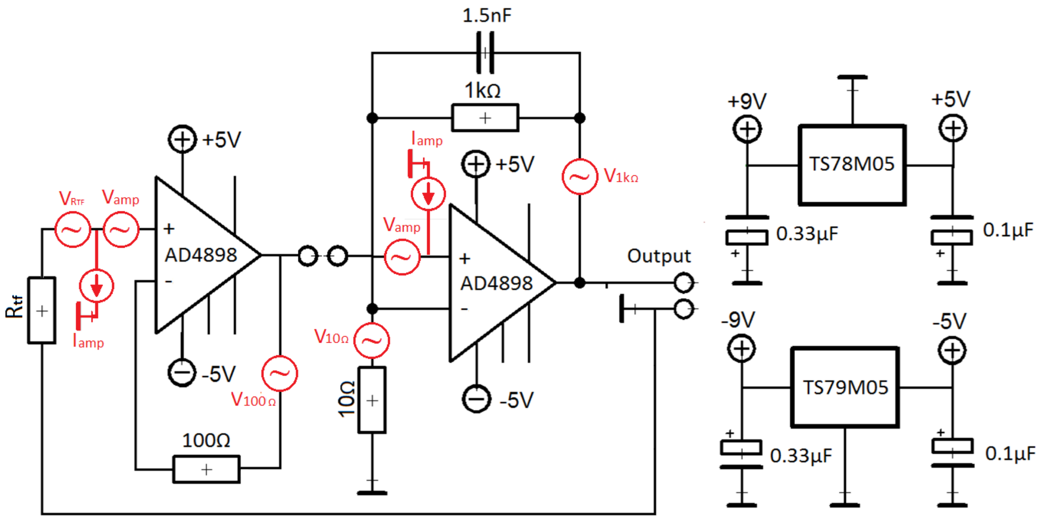

Figure 3.2: A schematic of the amplification circuit. On the left are the buffer and amplification sections and on the right are the voltage regulators powering the op amps. Symbols shown in red indicate the noise sources associated with the circuit.

The buffer amplifier creates a copy of the input voltage without drawing any current from the input source. The output of the source then can provide a current according to the capabilities of the amplifier in question. A 100 Ω resistor was placed across the negative input and the output at the suggestion of the manufacturer with the purpose of helping to stabilise the amplifier [61]. A break in the circuit was then introduced, between the output of the first amplifier and the input of the second opamp. This was to facilitate testing of the different stages of the circuit independent of the other stage and would be reconnected once the testing of the circuit was complete. In the second amplification stage, the signal was fed through an opamp with a gain of 101. This gain value was carefully chosen with the noise floor of the Agilent 35670A spectrum analyser taken into account. The lowest possible noise floor of the Agilent was approximately 20 nV/$\sqrt{Hz}$ and with a gain of 101 applied to the signal, the levels of the noise in the platinum resistor would be in the range of hundreds of nV/$\sqrt{Hz}$. This gain sufficiently increased the noise level of the platinum resistor to a readily measurable range. Finally, the output was then fed into an Agilent spectrum analyser where the amplitude spectral density was recorded. The power for the opamps was transmitted through a pair of voltage regulators; one with positive and one with negative voltage. This reduced the input voltage from approximately 9V to 5V which protects the opamps from surges and provides stable drive voltages. Tantalum and ceramic capacitors were placed on the output and input of the regulators and connected to ground. This is recommended on the manufacturer's data sheets of the regulators, and helped to filter both high and low frequency noise from the power supply. Once the circuit was tested and worked as expected, it was placed into an aluminium container to further shield the circuit from external effects.

3.2.3 Noise Model of Circuit

With the circuit designed, a model of the expected noise levels could be constructed. Using the values for the voltage and current noise for the amplifiers stated in their data sheet, and calculating the Johnson noise for each resistor, the total noise expected in the system could be calculated for a range of resistances for the sample resistor.

Referring back to figure 3.2 and focusing on the buffer section, the noise terms are,

$$V_b = \sqrt{(V_{R_{tf}})^2 + (V_{amp})^2 + (I_{amp}R_{tf})^2 + (V_{100\Omega})^2}, \tag{3.1}$$

where V_b is the power spectral density(PSD) from the buffer section, $V_{R_{tf}}$ is the thermal noise from the thin film resistor, V_{amp} and I_{amp} are the voltage and current noise from the amplifier, R_{tf} is the thin film resistance and $V_{100\Omega}$ is the thermal noise of the 100 Ω resistor. This provides the total PSD of the noise that is produced on the output of the buffer amplifier.

The second stage of the circuit is a non-inverting amplifier with a gain of 101. In this stage the noise terms from the buffer amplifier are then amplified by a gain of 101 in the second amplifier to produce the total PSD of the circuit,

$$V_{tot} = \sqrt{\underbrace{(V_b G)^2}_{\text{buffer section}} + \underbrace{(V_{amp}G)^2 + (V_{10\Omega}(G-1))^2 + (I_{amp}R_{tf})^2 + (V_{1k\Omega})^2}_{\text{amplifier section}}}, \tag{3.2}$$

The first term in equation 3.2 is the PSD of the noise on the output of the buffer amplifier. The following terms are the noise sources from the second stage of the amplifier circuit including the current and voltage noise of the second amplifier and the PSD the two resistors, $V_{10\Omega}$ and $V_{1k\Omega}$. The current noise term is calculated this way as the buffer amplifier creates a virtual image of the thin film resistor on the output, allowing the current noise of the second amplifier to be calculated in a similar way to the first amplifier. Note that the current noise from the second amplifier and the 1k Ω terms are not multiplied by the gain as these noise terms are added to the output of the amplifier and hence are not amplified. The gain applied to the 10Ω resistor is 100 which required the noise of the resistor to be multiplied by G-1.

The next step is to substitute V_b from equation 3.1 into equation 3.2 and rearrange,

$$\begin{aligned} V_{tot} = [((V_{R_{tf}}G)^2 + 2(V_{amp}G)^2 + (I_{amp}R_{tf})^2(G^2+1) \\ + (V_{10\Omega}(G-1))^2 + (V_{100\Omega}(G))^2 + (V_{1k\Omega})^2)]^{\frac{1}{2}}, \end{aligned} \tag{3.3}$$

And finally, to achieve the final noise model used, $V_{R_{tf}}$ is substituted with the Johnson noise equation shown in equation 2.21,

$$\begin{aligned} V_{tot} = [((4k_BTR_{tf}G^2) + 2(V_{amp}G)^2 + (I_{amp}R_{tf}(G+1))^2 \\ + (V_{10\Omega}(G-1))^2 + (V_{100\Omega}(G))^2 + (V_{1k\Omega})^2)\Delta f]^{\frac{1}{2}}, \end{aligned} \tag{3.4}$$

where V_{tot} was the total RMS voltage noise, Δf is the bandwidth, k_B is the Boltzmann constant, T is the temperature, R_{tf} is the thin film resistance, G is the gain of the circuit, V_{amp} is the voltage noise of the amplifiers, I_{amp} is the current noise of the first amplifier and $V_{10\Omega}, V_{100\Omega}$ and $V_{1k\Omega}$ are the noise of the $10\Omega, 100\Omega$ and $1k\Omega$ resistors respectively.

By taking into account the various components that would contribute to the noise levels, the noise model shown in figure 3.3 was produced by varying the thin film resistance value.

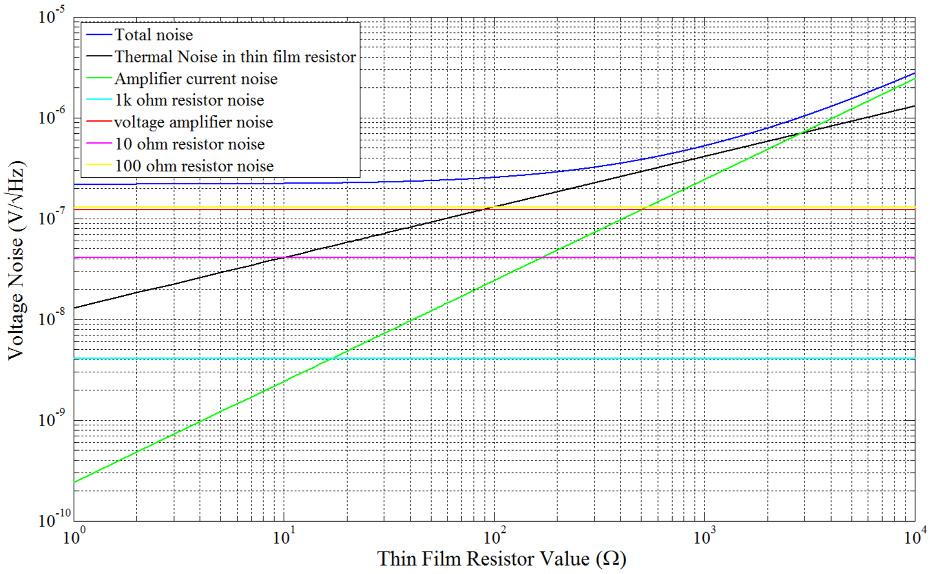

Figure 3.3: A Noise model created from the design/components of the circuit.

This model was used to test out the circuit's performance and also to determine the correct value of resistance of the thin film resistor to ensure its thermal noise was dominant.

3.2.4 Thin film resistor/copper bar mount

From the model above, it was decided that a value of 500 Ω would be acceptable. This value was chosen as it was a resistance where the thermal noise in the thin film resistor was the dominant noise source. The resistors were then made by Dr. Stuart Reid and Dr. Ross Birney in the University of the West of Scotland through a physical vapour deposition (PVD) method [62].

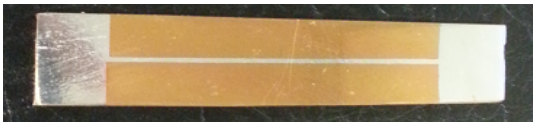

Figure 3.4: An early production of a platinum thin film resistor. The silicon layer on this resistor was too thin. This resulted in the copper substrate being in contact with the platinum which produced the wrong resistance. Later productions used a thicker layer of silicon to avoid this.

Thin Film deposition is a method of laying down layers of material which can range from nanometers to microns thick. The method that was used to create the resistors used in this experiment was DC magnetron sputtering. An illustration of this method is shown in figure 3.5. A small flow of the order of several sccm of gas (typically Argon) is directed into a vacuum chamber. Using a high impulse current applied to the cathode (the target), the neutral gas is ionised. These ions are then directed at the target due to the magnetic field produced by the magnets beneath the target which then ejects material from the target onto the substrate. This condenses to form a thin film on the substrate, with a thickness that can be controlled via process parameters inclusing power, pressure, gas flow and deposition time.

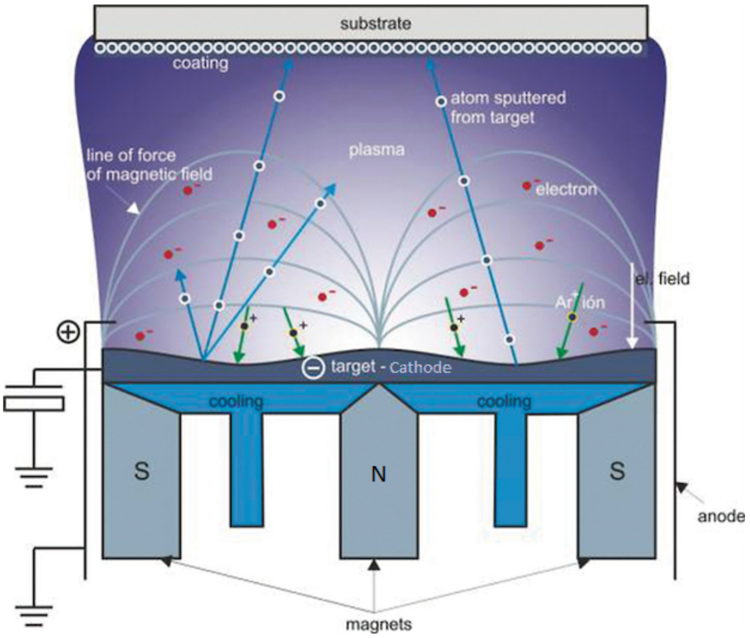

Figure 3.5: An illustration of the DC magnetron sputtering method of thin film deposition [63].

For this experiment a copper substrate was used and an initial silicon layer was laid down as an insulation layer. On top of this layer, using a mask, a layer of platinum was laid down in the required dimensions to produce a resistor of $\sim 500\,\Omega$. An attempt to measure the thickness of the platinum layer of the resistor was made using a Wyko NT1100 Optical surface profiler. It was discovered that the layer of platinum had sunk into the silicon layer, which prevented the profiler from calculating the thickness of the platinum. Instead, the thickness was calculated from the resistivity of the platinum and the known dimensions of the resistor using the following equation,

$$R = \frac{\rho x}{wt} \tag{3.5}$$

where R is the resistance, ρ is the resistivity of platinum, x is the length, w is the width and t is the thickness. The length of the resistor was 4 cm, the width was 0.5 mm, the resistance was 480 Ω and the resistivity was $1.06 \times 10^{-7}\Omega m$. Rearranging the above equation and using the values stated the thickness of the platinum was calculated to be $\sim 14\,nm$ which was approximately what was expected.

3.3 Control System

3.3.1 PID control

To control the temperature of the thin film resistor, a heater was placed inside the copper bar. A cartridge heater was chosen as it can be inserted into the copper bar and can produce a power of up to 40 watts to aid in the production of a range of temperatures and gradients. This design was modelled with ANSYS FEA to determine the range of thermal gradients that were possible, which will be explained further in Chapter 4. To control the power dissipated by this heater, it was decided that a PID control system would be used.

A Proportional-Integral-Derivative (PID) control is a feedback mechanism which can control a system. The PID system calculates an error signal which is the difference between the current measured value and the set point which is stated by the user. The PID algorithm is expressed as

$$u(t) = K_p e(t) + K_i \int_0^t e(\tau)\,\mathrm{d}\tau + K_d \frac{d}{dt} e(t) \tag{3.6}$$

where $u(t)$ is the controller output, K_p is the proportional gain, K_i is the integral gain, K_d is the derivative gain, e is the error signal, t is time, τ is the variable of integration (values from 0 to t) and $d\tau$ is the time difference of the loop, $\Delta\tau$ [64]. The error signal was produced by measuring the temperature with the PT1000 thermometers and calculating the difference between the current temperature and the setpoint. By tuning the different gains in the algorithm, the response of the algorithm could be fine-tuned to provide the optimum control response to minimise the error signal. The following sections will explain the function of the different parts of the algorithm and also give examples of the effects of the various gains. This data was recorded during the tuning of the PID used in this experiment.

3.3.2 Proportional Term

The proportional term in the algorithm takes the current error signal and produces a proportional output signal. This output signal can be adjusted by altering the value of the proportional gain; a larger gain increasing the response of the control. A gain that is too high can cause the algorithm to become unstable, and as a result the PID may oscillate out of control. Conversely, a gain that is too low will give a small enough response that the control will not be able to compensate for variations in the system. When tuning the proportional gain care must be taken to set it to a value that produces a large enough response that provides fast reactions to changes in the system, yet not large enough to destabilise the control.

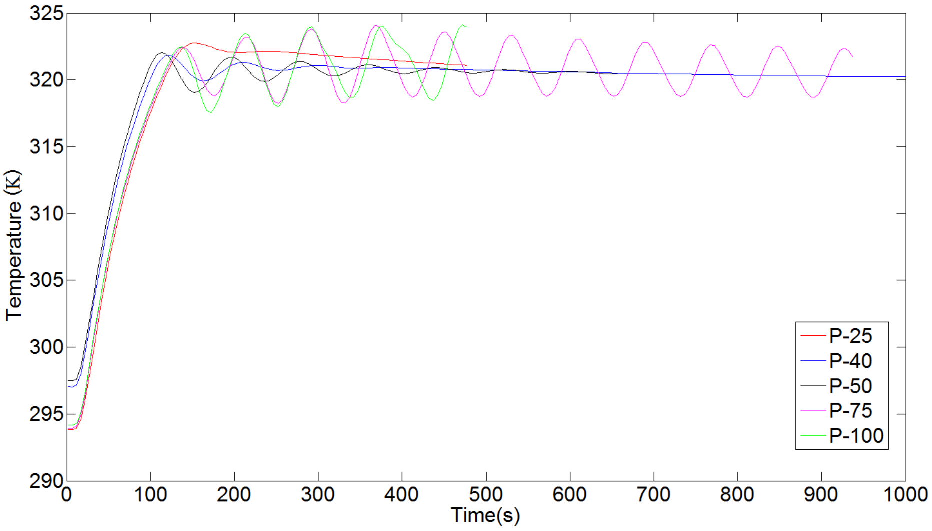

Figure 3.6: A graph showing the effect of different proportional gain values over time.

In figure 3.6 a graph of the response of the algorithm over time with a range of proportional gains is shown. For this data the integral and differential gains were kept constant. It can be seen that the high gains did not converge on the set point and continued to oscillate without decaying to the set point of 320 K, which is symptomatic of positive feedback. If the gains were set any higher than 50, the signal would ring indefinitely. The lower gain of 25 had a very slow response and, though it does decay towards the set point, it takes much longer than the other gains. It was therefore decided that a gain of 40 would be used. It gives a balance between not overshooting and the time it takes for the sample temperature to reach the set point.

3.3.3 Integral Term

The integral term in the algorithm is a summation of all the instantaneous error signals over time. This part of the algorithm integrates over the previous error values until the error value itself is zero. As with the proportional term, if the gain for the integral is set too high it can also destabilise the control and cause the output to increase out of control; if the gain is too small it will increase the time taken to reach the set point.

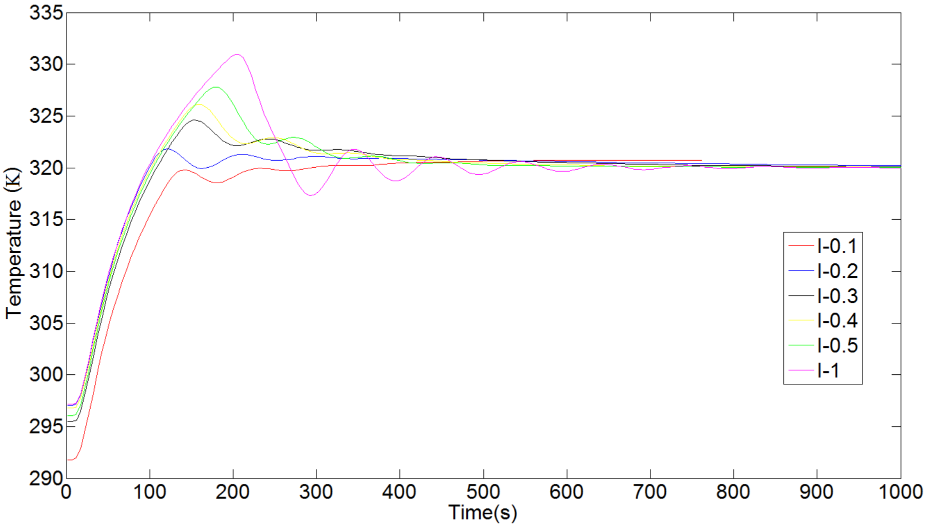

Figure 3.7: A graph showing the effect of different integral gain values over time.

In figure 3.7, the effects of different integral gains can be seen on the output of the PID over time. High integral gain can be seen to overshoot and cause the PID to take longer to reach the set point while low integral gain is shown to give a small response to the system and so takes longer to reach the set point. A gain of 0.2 was used, as it gave a fast response to the system and quickly reached the set point with minimal overshoot.

3.3.4 Derivative Term

The derivative term in the algorithm monitors the rate of change of the error signal and compensates for any large changes. As this is a differential, the error signal is also sensitive to noise. It applies a damping term, which tends to stabilise the system against PI control. A high derivative gain will provide a response that could overcompensate for the changes in the system and destabilise the control, so once again the gain of the derivative must be tuned carefully.

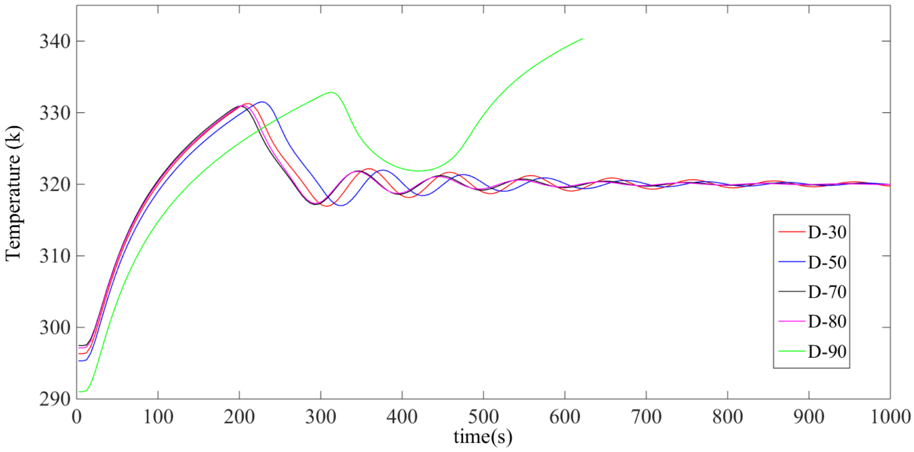

Figure 3.8: A graph showing the effect of various differential gain values over time.

In figure 3.8, the effects of different derivative gains on the output over time are shown while keeping the proportional and the integral gains constant. The high gain signal (D=90) can be seen to become unstable and eventually increase far beyond the setpoint of 320 K. Lower gain signals can also be seen to take longer to stabilise at the setpoint. The value of 80 was chosen as it gave the shortest response time, though a gain of 70 would also have been acceptable. Using these values the system would take approximately 5 minutes to stabilise to within 1 K of the set point and 10 minutes to stabilise to within 0.1 K of the setpoint.

3.4 Feedback control system

Combining a PID control with a Pulse Width Modulation (PWM) technique would allow for the automated control of the power of the heater to produce the required temperature across the resistor. A PWM control is a technique where the power of an electronic device is controlled through pulsing the power on and off. When the power supply is set to its maximum value, the power of the heater can be set to any value between the minimum power and the maximum power. This is done by applying a waveform to the power supply with a frequency higher than the response time of the heater. The frequency used was 490 Hz which was the standard PWM frequency of the Arduino Mega board which is high enough to control a heater with a time constant of ~3 minutes. The duty cycle is the percentage of a period that the signal is active. This means that a 0% duty cycle produces a signal that is never active and so gives zero power in this system, a 25% duty cycle produces a signal that is active for a quarter of a period and as such produces 25% of the maximum power in this system; and a 100% duty cycle produces a signal that is always on and produces the maximum power possible for this control system.

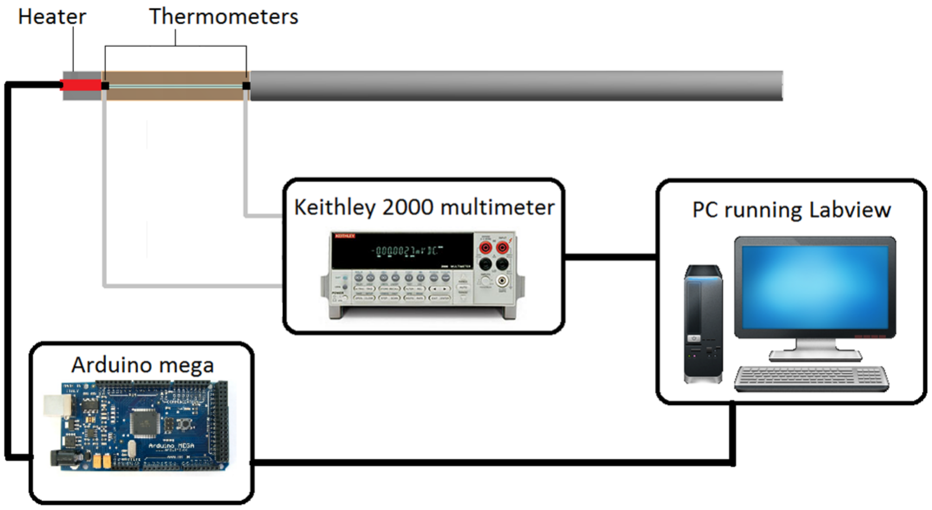

Figure 3.9: A diagram indicating the process of the feedback circuit used in this experiment.

Figure 3.9 demonstrates how the feedback control functioned. The Labview program performed three steps simultaneously; one step controlled the Keithley 2000 multimeter, another ran a PID control using least squares fitting, and the final used the output value of the PID control to run a PWM pin on the Arduino mega microcontroller. The initial input was read from the Keithley multimeter control and converted into the related temperature using the equation provided in the PT1000 data sheet [65]. This temperature was then recorded and then fed into the PID section and used as the PID input. In each iteration of the PID loop the new temperature measurement was added to the previous readings and a least square fit was performed and fed into a PID loop. This loop then calculated an output value which was used to alter the system in order to bring the measured temperature close to a controlled set point. The output of the PID was then converted into an 8-bit value relative to the chosen set point. This 8-bit value could then be used in the Arduino section of the code to drive a PWN pin on the Arduino board. A copy of the code can be found in appendix A.

By placing a transistor in the circuit providing power to the heater, the power level could be controlled by driving the transistor with the PWM pin on the Arduino board. This transistor could then switch at a rate that corresponded to the duty cycle of the PWM pin and provided the required power to the heater. The circuit for this section of the control system is shown in figure 3.10.

The MOSFET transistor works by applying a small voltage to the gate terminal which enables a current to flow between the source and drain terminals. This allows the use of a small voltage to switch the larger heater current on and off. Finally the heater will be set to a certain value which will in turn change the value on the initial thermometer. This completes the feedback control system.

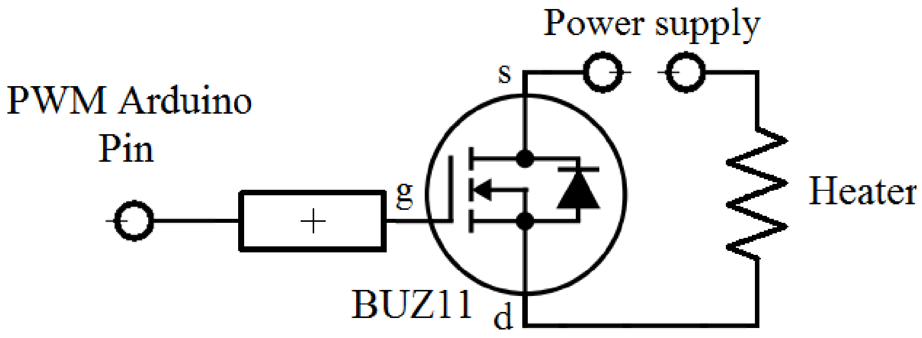

Figure 3.10: The circuit diagram of the simple transistor circuit used to control the power of the heater.

3.5 Cryogenic Setup

Once initial room temperature tests were conducted, a setup for submerging the copper bar in liquid nitrogen was conceived. Initial plans to place the copper bar through the side of a container, and so have it completely submerged to create a steady flow cryostat, were quickly replaced. Problems with creating a cost effective container that the copper bar could be inserted into, while still maintaining an adequate seal to hold in the liquid nitrogen, prevented this idea from moving forward. Any seal that would be available for this experiment would contract at low temperature and cause the seal to fail.

The first design involved using two clamp stands to suspend the vacuum chamber over the polystyrene Dewar containing the liquid nitrogen. The Dewar was placed on top of a platform with an adjustable height. This allowed safe submersion of the copper bar by raising the platform the Dewar sat on in a controlled manner. However, due to the addition of the turbo pump the clamp stands were not strong enough to hold the setup.

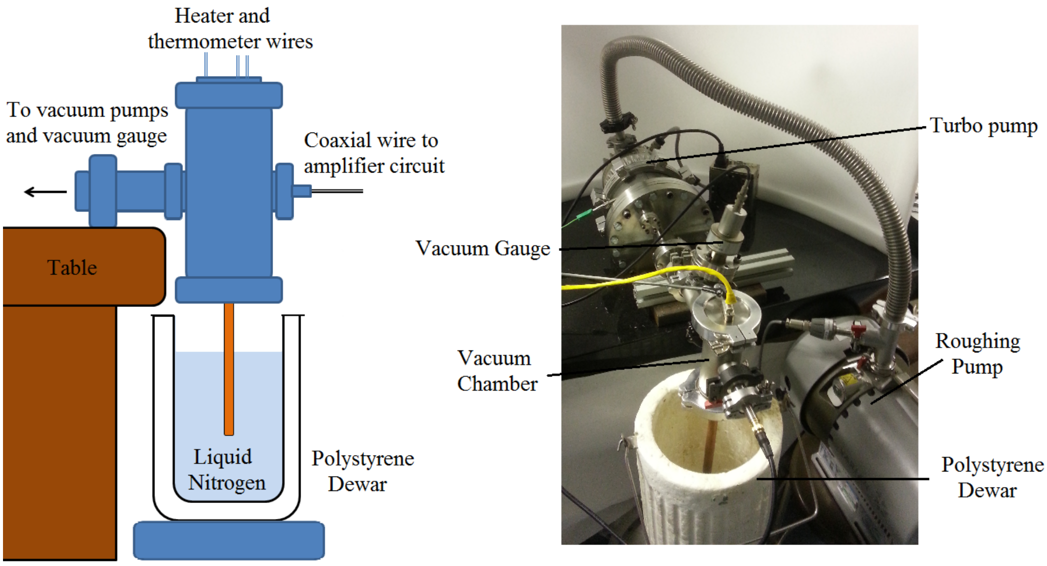

Figure 3.11: The vacuum chamber and setup suspended over a polystyrene Dewar. The Dewar is filled with liquid nitrogen and placed on a surface that can be raised until the copper bar is submerged in the nitrogen.

Fig 3.11 shows the final setup. The safest way to maintain the design was to place the turbo pump on the edge of a table and allow the copper bar to suspend over the Dewar which would sit beside the table. Again, for safety, the Dewar was placed on a rising platform to allow the copper to submerge. This setup takes approximately 6-7 minutes to cool to its lowest temperature. The minimum temperature achievable using this setup varied between 100 K and 120 K depending on the level of liquid nitrogen present in the Dewar.

3.6 Conclusion

Due to the sensitive nature of the measurements that were required for this experiment, the design and construction of the setup had to be planned carefully. The circuit used to measure the noise in the sample needed to amplify the noise above the noise floor of the spectrum analyser while minimising the additional noise from each of the components in the circuit. Once the design was finalised, a noise model was created to choose the optimum value for the thin film resistor sample. The rest of the setup was then constructed with the aim of being able to control the temperature gradient across the sample using a heater controlled by a PID controller. Using this setup, it was possible to measure the thermal noise of a thin film resistor while under a desired temperature gradient at cryogenic temperatures.

Chapter 4

Modelling and Testing of the Experimental Setup

4.1 Introduction

Before the experiment was set up, a number of models were created to estimate the thermal properties of the apparatus and also to help choose certain aspects of the setup. For the thermal aspects of the experiment, a finite element analysis (FEA) was created to predict the temperature gradients of the system. The requirements for producing different gradients (for example, heater power and copper bar dimensions) could then be understood, and the equipment to produce the required gradients could then be constructed, which will be discussed in sections 4.2. Various tests were also conducted to assess the performance of the amplification circuit, and the physical components of the circuit which will be discussed in sections 4.3 and 4.4.

4.2 FEA Thermal Model

4.2.1 Simple Copper Bar

Chapter 3 described the physical design of the system and how the thermal gradients at cryogenic temperatures were going to be achieved. To perform this modelling, the finite element analysis package ANSYS was used [66], which is a multiphysics simulator. This allowed for the modelling of the experimental setup and the ability to place conditions on the model such as initial temperature, heat flow, radiation and convection.

A simple model of just the copper bar was created to test how the prediction of the model held up to real experimental data. Small alterations to the properties of copper in the program were required, as values such as thermal conductivity and specific heat were only provided for room temperature. Since these properties depend on the temperature of the copper, a range of values from 1 K to 300K were added for specific heat, thermal conductivity and thermal expansion coefficients [67]. A plot of the thermal conductivity for different materials is shown in figure 4.1.

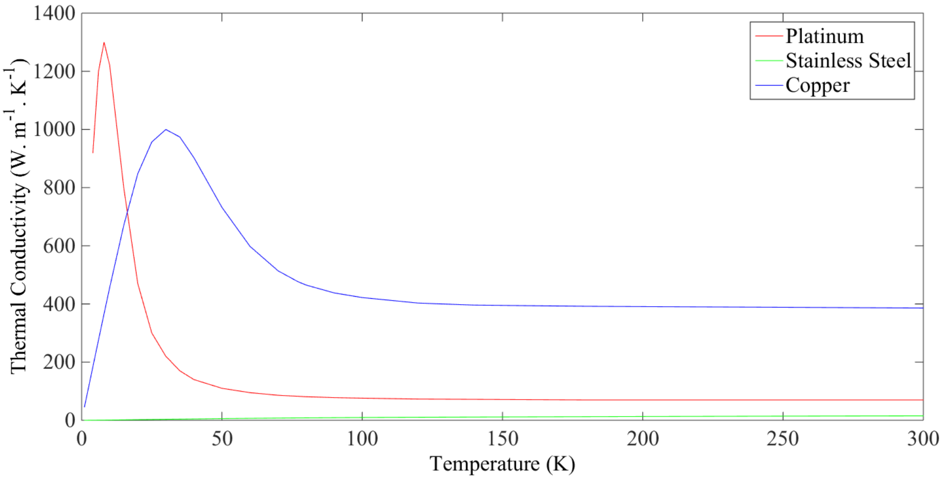

Figure 4.1: A plot of thermal conductivity at various temperatures for platinum, stainless steel and copper.

An initial temperature of 293 K was set, since the copper bar would initially be at room temperature. The flat end of the bar was set to 77 K, to simulate the end of the bar being in contact with liquid nitrogen. The final parameter that was set was a heat flow into the opposite end of the copper bar to represent the heater. By varying the value of the heat flow, different gradients were produced in the model, which could then be compared to experimental results. For the experiment, platinum resistance thermometers were to be placed on the area of the copper bar on which the thin film resistor would be mounted. They were placed at either side of this area to observe the gradients in question. In the model, temperature probes were placed in areas where the thermometers would actually be situated, in order to observe the temperatures expected to occur. This is shown in the model and can be seen in figure 4.2.

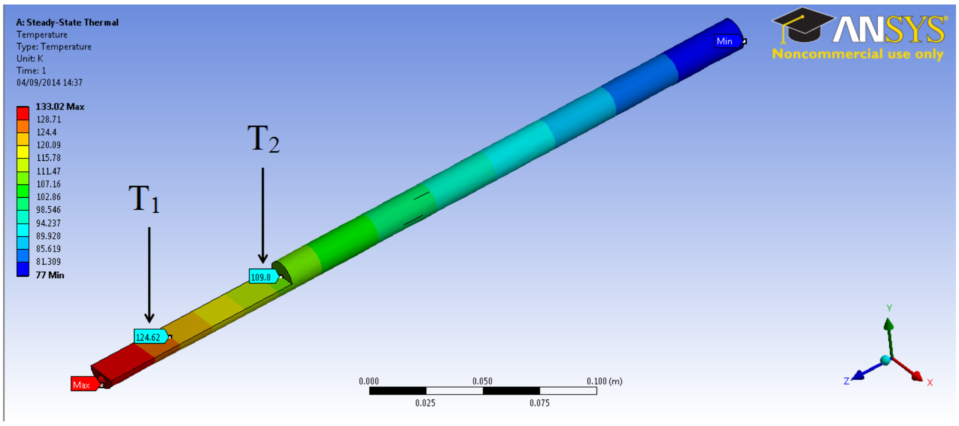

Figure 4.2: An ANSYS model of the temperature of the copper bar with a heat flow of 10 W.

Convergence tests were performed in order to optimise the level of meshing and, thereby, ensuring optimal model performance. There was a variation of 0.5 K between the values using a coarse mesh and a fine mesh. As this difference was small, a coarse mesh was used to reduce the time taken to solve the model. This then produced a model with 499 elements, with the solver being program-controlled; this allows the program to choose the most suitable options for the solver.

Power	Predicted Results			Experimental Result		
	Max Temp (K)	Min Temp (K)	Temp Difference (K)	Max Temp (K)	Min Temp (K)	Temp Difference (K)
10	117	99	18	138	126	12
20	165	122	43	161	139	22
30	212	146	66	191	159	32
40	261	171	90	218	177	41

Table 4.1: Comparison between experimental results and predicted results from ANSYS model for simple copper bar model.

By comparing the predicted temperatures to the experimental results, shown in table 4.1, the model is seen to closely resemble the real data at low powers, but quickly diverging as the power increases (also shown in figure 4.3). The divergence of the values can be attributed to experimental factors that were not introduced into the model. These include;

- The effect of the surrounding air could have introduced an additional convective heat flow.
- Liquid nitrogen evaporating during experiment and changing the point of contact of the liquid nitrogen on the copper bar, thus altering the boundary conditions.
- Not modelling the chamber

The results implied that a more complex model was required to better simulate the effects seen experimentally.

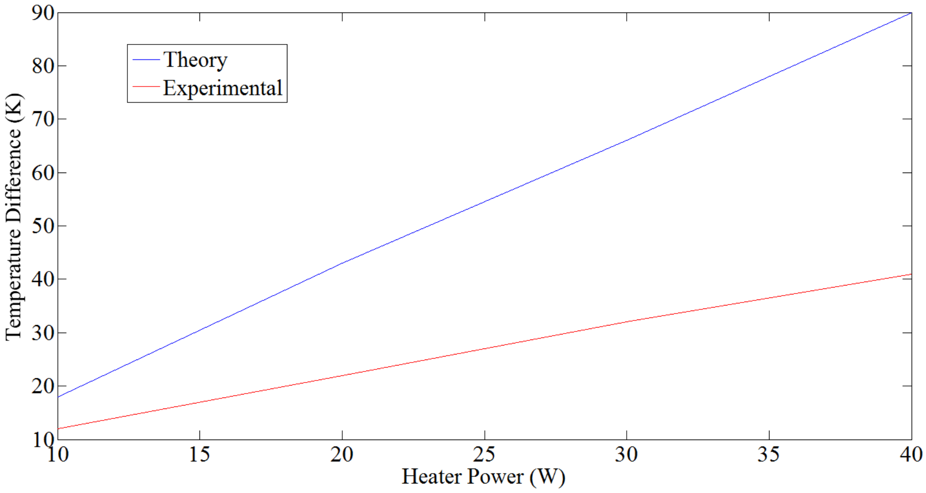

Figure 4.3: A plot of dependence of thermal gradient on heater power for simple copper bar model.

4.2.2 Model of complete experimental setup

Since the previous model did not compare well to the experimental data, a new model was required. The next model that was built more closely represented the real experimental setup, where both the stainless steel vacuum chamber and the thin film platinum resistor were included. Figure 4.4 shows the copper bar and the stainless steel vacuum chamber, where the platinum resistor lies inside the chamber.

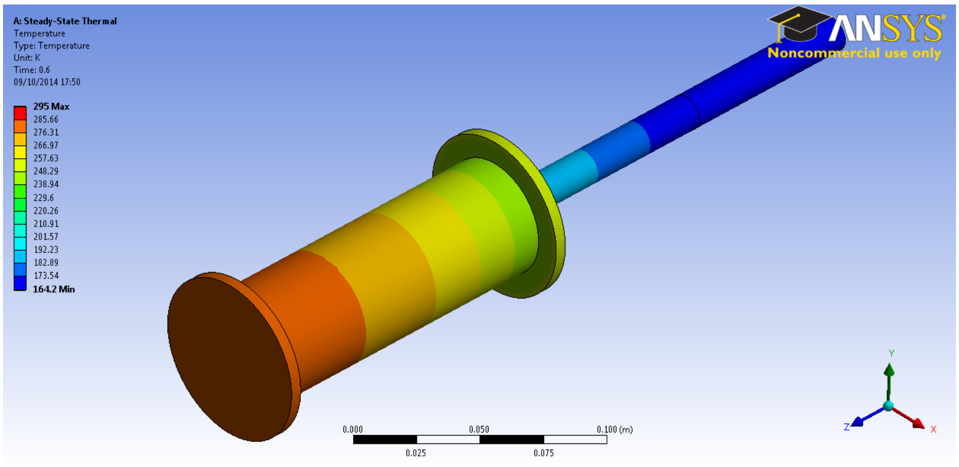

Figure 4.4: An ANSYS model of the temperature of the full setup model with a heat flow of 10 W.

Figure 4.5 shows the model that was produced. Connections between the different components were made in the model using the bonding function to indicate where surfaces were in thermal contact with other sections of the setup. Without doing this the ANSYS program will not recognise that they are in contact, and so will not calculate the thermal conduction between the two materials in question. The stainless steel container is hidden in this picture to allow for the viewing of the copper bar inside.

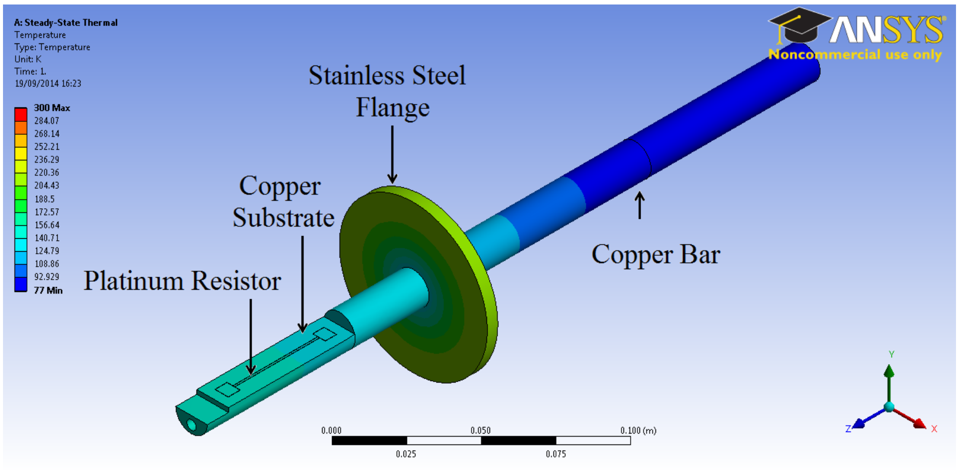

Figure 4.5: An ANSYS model of complete setup with a heat flow of 10 W. The stainless steel container has been hidden in order to observe the gradient across the platinum section.

Further improvements to the model were made by adding in radiation terms for heat transferred between the inner surface of the vacuum chamber and the copper bar/thin film resistor, and for convection components for thermal exchange between the metals and atmosphere. The vaues of emissivity used for the radiation terms were 0.54 for the copper and platinum resistor and 0.05 for the stainless steel [68]. Convection terms for the effect of air outside of the tank was estimated to be 5 $W/(m^2K)$.

Power	Predicted Results			Experimental Results		
	Max Temp (K)	Min temp (K)	Temp Difference (K)	Max Temp (K)	Min Temp (K)	Temp Difference (K)
10	146	137	9	138	126	12
20	173	156	17	161	139	22
30	201	174	27	191	159	32
40	227	192	35	218	177	41

Table 4.2: Comparison between experimental results predicted by ANSYS model of copper bar and vacuum chamber.

The experimental data shown in table 4.2 showed a much better agreement with the values from the updated model, as it was constructed to be closer to the real experimental setup. Table 4.3 shows the difference between the predicted value for each model and the experimental value and clearly shows that although the full model has not reached an acceptable agreement, it has greatly improved upon the simple model values.

Power (W)	Experimental Temperature Difference (K)	Percentage Difference	
		Simple model	Full model
10	12	34	25
20	22	49	23
30	32	52	16
40	41	55	14

Table 4.3: Table showing the percentage difference from model values to experimental value.

Further improvements to the model could be envisaged, such as wires connecting the end flange to the copper bar, heat sink paste placed to improve thermal contact between heater and copper bar, and accounting for the effects of residual gas in the vacuum chamber. These additions could improve the model to align more closely with experimental observations, or they could indicate that presence of phenomena that were not accounted for, and thus indicate that further investigation is required. Using this model, small details such as position of heater in copper bar and geometry of mounting surface for the thin film resistor were optimised to provide the best possible control of the absolute temperature and temperature difference across the resistor.

Modelling is a very useful tool in aiding the design process of an experiment and also in providing a prediction of what is expected from an experimental setup. Through refinement of the constructed models, refinements of the experimental setup are possible; thus, the experiment itself can be improved through modelling.

4.3 Circuit Testing

With the circuit built, a range of tests were conducted on the setup in order to better understand the physical components of the circuit and the noise they added to the total voltage noise. As described in chapter 3, the circuit used op-amps, to buffer/amplify the Johnson noise of the thin-film resistor. These had both a current and voltage noise associated with them that can be found on the data sheet, [61]. The following tests were conducted to ensure that the values stated in the data sheet were infact the correct values, and to determine accurate values for the voltage and current noise for use in the final analysis.

4.3.1 Current and Voltage noise

In chapter 3, the design of the circuit was discussed briefly. The circuit comprised a buffer stage and an amplification stage. When deciding on the components for the circuit, it was important to choose low-noise amplifiers. The final choice for these amplifiers were ADA4898-1 op-amps, described as ultralow noise. The specifications for this amplifier stated that the typical voltage noise was $\sim 0.9\,nV/\sqrt{Hz}$, and the typical current noise was $\sim 2.4pA/\sqrt{Hz}$ [61].

To measure these values, it was possible to utilise equation 3.2. In this equation, a number of terms are dependent on the resistance of the thin film resistor. By rearranging equation 3.2 and ignoring the noise levels from the other resistors, the equation was expressed in the form,

$$\frac{V_{tot}^2}{\Delta f} = (I_{amp}G)^2R^2 + (4kTG^2)R + 2(V_{amp}G)^2. \tag{4.1}$$

Using this form of the equation, the amplitude spectral density of the voltage noise squared was plotted against the resistance. By fitting a second order polynomial to the data, the coefficients of the fit can be used to calculate both the current noise and voltage noise associated with the amplifiers. To do this, a number of wire-wound resistors with a value of between $10\,\Omega$ and $100\,k\Omega$ replaced the thin film resistor. For each resistance, a number of noise values were taken in order to gain an average value for the noise of that resistance. Once a full range of noise levels were recorded, they were plotted against the resistance. Figure 3.3 in chapter 3 shows that at low resistance values, the voltage noise dominates, and at high resistances the current noise dominates.

Due to this, two plots were made; one for voltage noise, which focuses on the lower value resistors, and one for current noise, which includes the higher value resistors. This was done in order to give more accurate coefficients on the fit for each noise source.

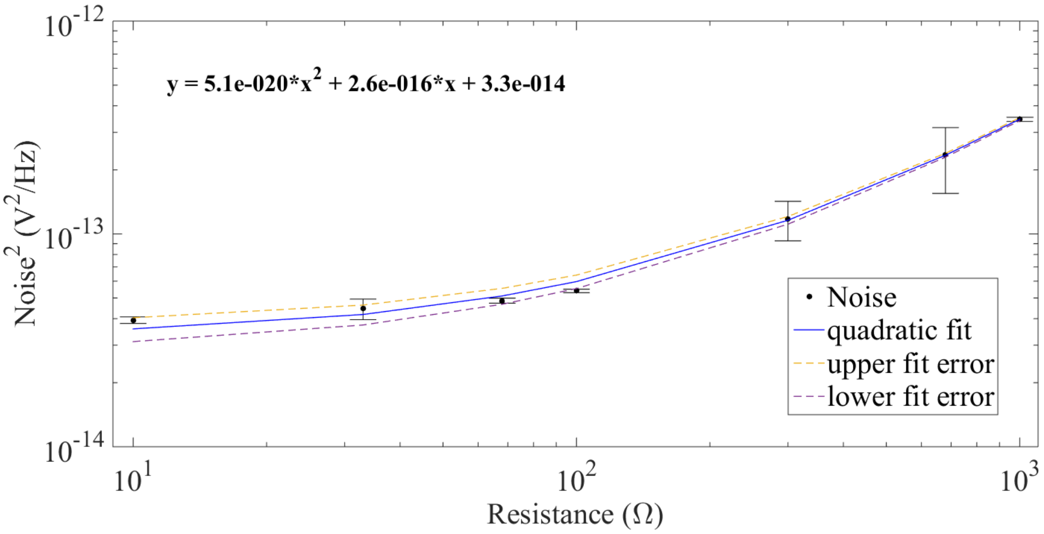

Figure 4.6: Data for determining voltage noise using various low value resistors.

Figure 4.6 shows the data together with a second order polynomial fit. For the voltage noise, referring back to equation 4.1, the coefficient of interest is the constant, $3.31 \times 10^{-14} V^2$. This equates to the value of the final term in equation 4.1 giving,

$$2(V_{amp}G)^2 = 3.31 \times 10^{-14} \tag{4.2}$$

Rearranging with G=101, the equation gives the measured value of $1.2\, nV/\sqrt{Hz}$ for the voltage noise. The value stated in the data sheet for the amplifier stated that the voltage noise was $0.9\, nV/\sqrt{Hz}$. This value was slightly higher than expected but still at an acceptable level.

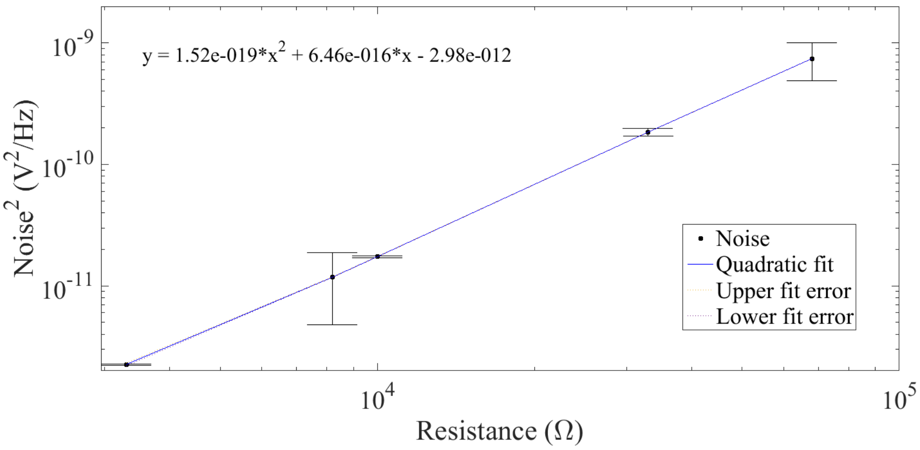

Figure 4.7: Data for determining current noise using various resistor values.

Figure 4.7 shows the upper range of resistances and the fit to the data. For this measurement the term that is associated with the current noise is the first term in equation 4.1. With the value of $1.52 \times 10^{-19} A^2$ for the quadratic term then translates to,

$$(I_{amp}G)^2 = 1.52 \times 10^{-19}. \tag{4.3}$$

Once again rearranging and using the value of 101 for G, the value for the current noise was $3.8\, pA/\sqrt{Hz}$ with the value stated in the data sheet being $2.4\, pA/\sqrt{Hz}$. Once again, the value is higher than expected but still at an acceptable level.

The values for the current noise and the voltage noise calculated in this section will be used in later analysis. This will provide a more accurate theoretical value of future noise level measurements in chapters 5 and 6.

4.4 Johnson Noise test

A final test was run was to investigate the performance of the apparatus by using a $1.5\, k\Omega$ resistor at various temperatures. $1.5\, k\Omega$ was chosen as, at the time, it was believed that this was when the thin film noise was dominant. Further improvements to the model shown in figure 3.3 showed that the thin film noise was dominant when the resistor value was $\sim 500\Omega$. Ideally, a value of 500 Ω would have been optimal, but 1.5 $k\Omega$ was adequate for this test. The setup was programmed to increase the sample wire wound resistor to a specified temperature and record a number of noise spectra. This was performed for a range of temperatures between room temperature and approximately 380 K. By assuming the wirewound resistor used in this test was the dominant noise source, we can rearrange equation 4.1 to give,

$$\frac{V_{tot}^2}{\Delta f} = 4kRG^2T \tag{4.4}$$

By plotting the square of the measured amplitude spectral density against temperature of the resistor, a value for the gradient of the fit of the data can be compared to the theoretical value of the gradient.

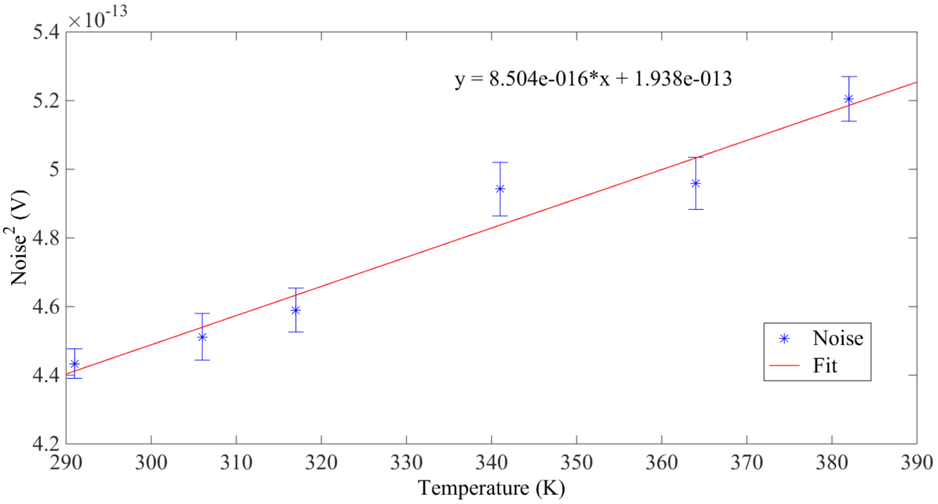

Figure 4.8: Data from the initial test using a $1.5k\Omega$ wirewound resistor at various temperatures.

The gradient of the fit is measured to be $8.50 \times 10^{-16} J\Omega/K$. Using the values for resistance R, Boltzmann constant K, and Gain G of 101, the theoretical value for the gradient was $8.44 \times 10^{-16} J\Omega/K$. This shows a good agreement between measured and theoretical values, which indicates that the circuit design was adequate for its purpose, and also that the construction of the circuit was good enough to minimise the addition of extra noise into the system.

4.5 Conclusion

Modelling is a very useful tool in the design and testing of an experimental setup. It allows the testing of various designs of the setup without having to physically build multiple versions. In designing this experiment, the FEA package ANSYS was used to perform thermal analysis of the design for the copper bar mount and the vacuum chamber. This provided an estimation of the temperatures at each point of the setup, and thus of the thermal gradient across the sample resistor. By varying the heat flow into the system, the model provided information on the required power of the heater to produce certain thermal gradients.

Tests were also performed on the amplification circuit to assess its performance. By recording a range of noise spectra with varying resistances, a model of the total noise could be used to calculate the voltage and current noise. By measuring these values and comparing them to the stated values in the data sheets, the performance of the circuit was assessed and showed to perform well.

Further modification to the FEA thermal model could be made to further resemble the physical setup. This would improve the accuracy of the model and allow for more fine-tuning in the design of future experimental setups.

Chapter 5

Room Temperature Results with the Thin-film Resistor

5.1 Introduction

Initial data runs were conducted with the thin-film resistor at room temperature, with the intention of observing how the presence or absence of a thermal gradient across the resistor affected the total noise in the system. During this process, the experimental setup was further modified to improve the sensitivity by addressing issues that arose; these will be detailed later in this chapter. Before proceeding to the cryogenic tests a number of data runs at room temperature and above were conducted. The intention was to gain an understanding of the behaviour of the total noise in the thin film resistor when the thermal gradient was small compared to the absolute temperature across the whole resistor.

5.2 Thermal Gradient Noise Calculations

In order to understand the data that is produced, the expected values for the noise level from the resistor when under the effect of a thermal gradient were calculated using the equation for Johnson noise, shown in equation 2.21. The resistor was split into 10 equal parts, as shown in figure 5.1. Assuming that each part contributes equally to the total resistance, a quadrature sum was used to calculate the total noise of the sample resistor. This also involved taking into account the change in the temperature and also the change in resistance due to temperature.

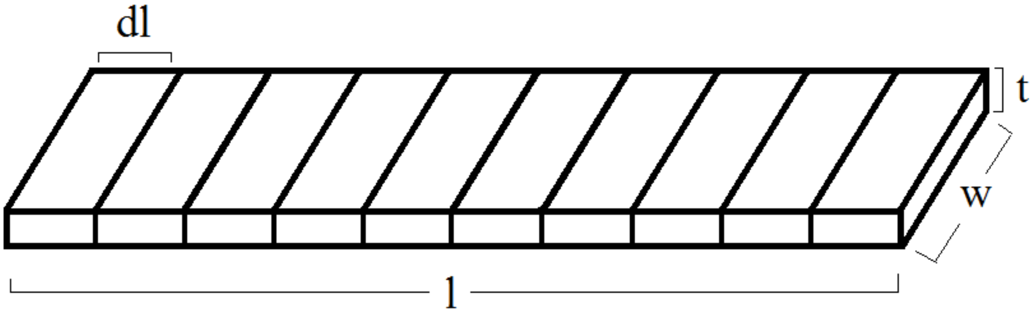

Figure 5.1: A schematic showing how the resistor was theoretically split for noise calculations.

The total resistance for the thin film resistor sample was 480 Ω, thus each section was taken to be an individual resistor with a resistance of 48 Ω. The platinum had a thickness of $\sim$ 14 nm, a width of 0.5 mm, a length of 4 cm (subsequently dl would be 4mm) and a resistivity of $1.06 \times 10^{-7}\,\Omega m$

Due to the resistance of a material being dependent on its temperature, the resistance of each section of the resistor was different due to the thermal gradient across it. By plotting the absolute temperature of the resistor against its related resistance and creating the plot shown in fig 5.2, it was possible to relate the two variables. Using this relation, the resistance of one section was calculated by dividing the total resistance at a given temperature by the total number of sections. This provided both the temperature and the resistance of each section.

Since the temperature and resistance was accurately known, the thermal noise of each section could be calculated using ($4kTRG$) where k is the Boltzmann constant, T and R are the temperature and resistance of each section and G was the gain of 101. The 10 noise values from each section of the resistor were then added in quadrature to gain the total noise contribution from the

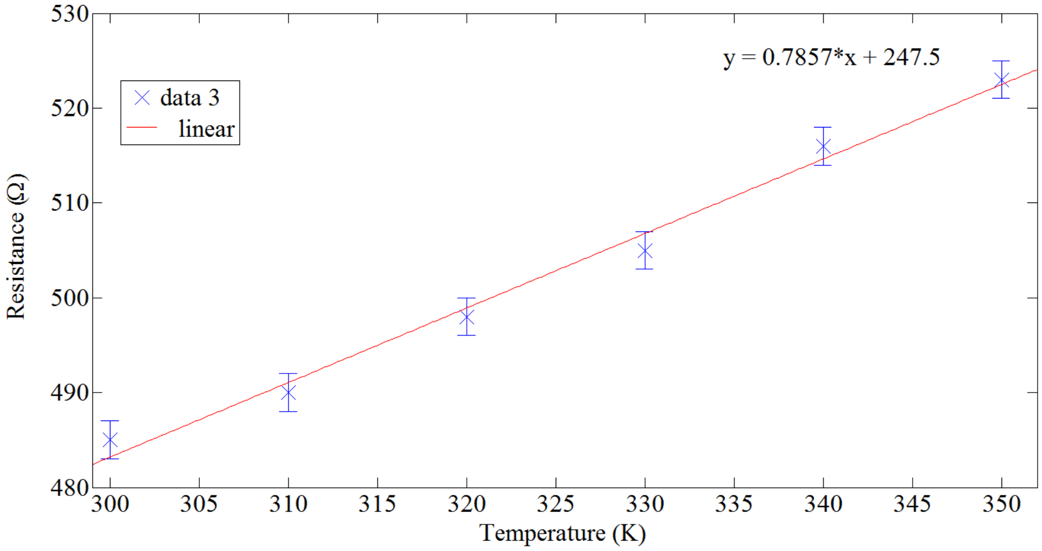

Figure 5.2: A plot of measured resistance against temperature used to gain a linear fit for noise calculations. Each resistance was measured with the most uniform temperature achievable across the resistor.

individual sections of the resistor shown in the equation 5.1

$$\frac{v_{resistor}}{\sqrt{\Delta f}} = \sqrt{(\sum_{i=1}^{10}(4kT_iR_iG)^2)}, \tag{5.1}$$

The final stage of this calculation is to add the total noise contribution from the sample resistor to the other noise produced in the circuit to then produce the total noise value which is once more added in quadrature and shown in equation 5.2,

$$\begin{aligned}\frac{v_{tot}}{\sqrt{\Delta f}} = ((v_{resistor})^2 + 2(V_{amp}G)^2 + (I_{amp}R_{tf}G)^2 + (V_{10\Omega}(G-1))^2 \\ +(V_{100\Omega}(G-1))^2 + (V_{1k\Omega})^2)^{\frac{1}{2}},\end{aligned} \tag{5.2}$$

Using this method, the calculation of the total theoretical noise of the resistor when its temperature is 300 K with a thermal gradient of 6 K gave a value of 354.29 $nV/\sqrt{Hz}$. From experimental data, the noise level was measured to be $\sim 359 \pm 5.6 nV/\sqrt{Hz}$. This shows that the theoretical value is within the error of the measured value and that it is reasonable to use this method when calculating expected noise levels during the analysis.

5.3 Recording/Processing Data

The noise data was initially recorded using the Agilent spectrum analyser and transferred onto the computer using a floppy disk. This was time consuming as the limited space on the disk required data to be transferred frequently. To address this, the spectrum analyser was connected to the computer through a GPIB port, and a Labview interface was downloaded from the National Instruments website to allow direct control of the analyser from the computer. This code is shown in appendix B. The analyser was set to record the power spectrum of the signal coming from the amplification circuit with a resolution of 1600 lines and a bin width of 1 Hz. The frequency bandwidth used to record data was varied for different measurements, as at times there was excess noise present in the spectrum, the source of which could not be identified. Various bandwidths were utilised to find a frequency range that showed the minimum interference. The signal was averaged over 100 iterations and would take roughly 10 minutes to gain one spectrum. Small alterations were made to the Labview code to allow both recording of the data onto a .txt file, and also a function to automatically record a defined number of data sets. With this function it was possible to remotely control the setup and automate the data recording.

Figure 5.3 is a spectrum that shows that the noise was white above 100 Hz. The noise spectrum also has $\frac{1}{f}$ and 50 Hz mains pickup noise, and a number of the 50 Hz harmonics are also still at a level where they occurred above the white noise floor. The circuit was placed inside a metal box to shield it from sources of 50 Hz, such as the lights and the mains power. This reduced the pickup noise substantially, but did not completely remove it. If the harmonics were not at a level where they appear above the noise floor, the simplest solution to remove this noise would have been to measure above ~ 60 Hz. However, as they were still observable above the white noise level, a solution was required after the data was recorded. As part of the analysis of

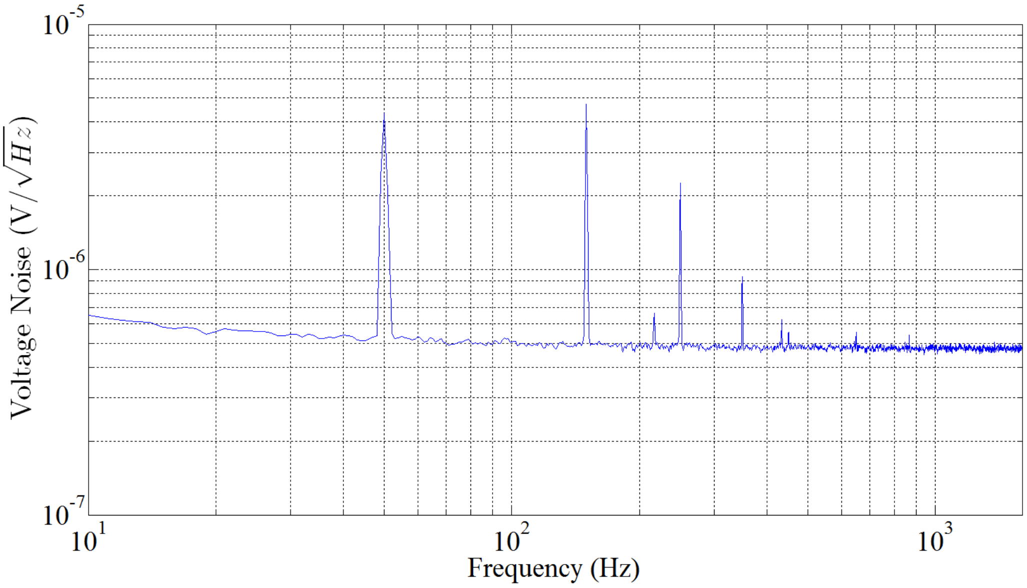

Figure 5.3: An early noise spectrum taken using the Agilent spectrum analyser showing a bandwidth between 1 Hz and 1.6 kHz. Spikes in the spectrum are mainly due to 50 Hz pickup noise and the rise in noise level at low frequency is due to amplification $\frac{1}{f}$ noise.

the data, a Matlab code was written to remove the 50 Hz noise signal. This was done by writing a code that read each value of the noise level, and any points lying above a stated value are assumed to be external noise, and are replaced with the average of the previous and following values. This assumed that, if the 50 Hz noise and external noise was not present, that the value at that point would have approximately the same value as the points lying on either side. The value for the upper noise limit was chosen to be $100nV/\sqrt{hz}$ above the theoretical noise level for a given temperature and resistance. This value was chosen as it would represent a temperature increase of roughly 150 K and a corresponding increased resistance of 130 Ω, which was extremely unlikely due to the control system used. The code was also designed to produce a line of best fit, and gives the value of its intercept and gradient. Assuming the signal is white noise, then there should be zero gradient to the fit and the intercept will correspond to the value of the white noise level. Also, to remove the $\frac{1}{f}$ noise, the bandwidth that the spectrum is recorded over was changed from between 10 Hz and 1.6 kHz to between 1.8 kHz and 3.4 kHz since the $\frac{1}{f}$ noise is dominant at low frequencies. Figure 5.4 shows a noise spectrum after it has been processed.

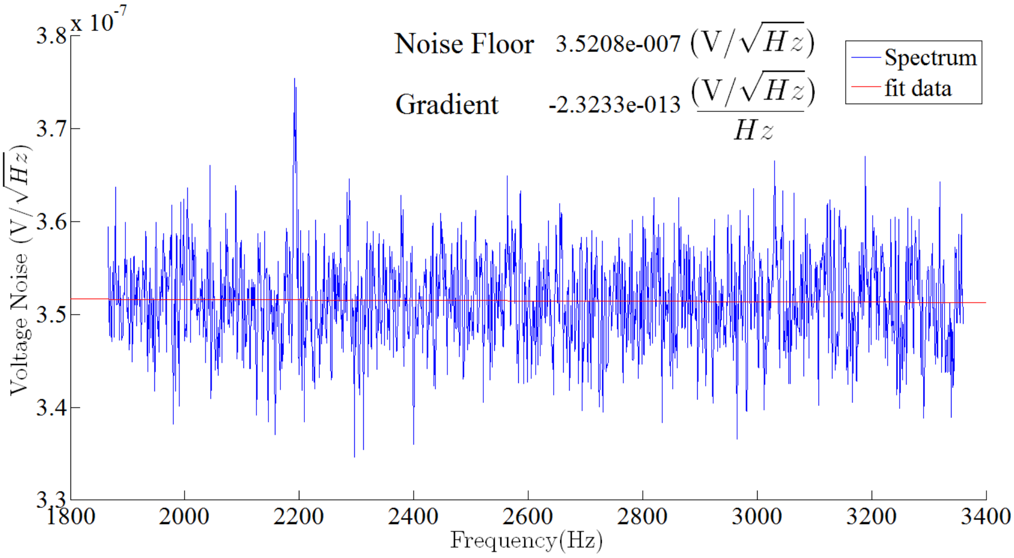

Figure 5.4: A noise spectrum taken at room temperature, post-processing.

5.4 Noise variance test at 330 K

The initial data runs were conducted overnight at 330 K with a ~6 K thermal gradient across the resistor. By observing the measured noise value and comparing it to the theoretical noise value, it was possible to determine whether or not there was evidence of excess noise when the thermal gradient was much smaller than the absolute temperature. Approximately 500 data runs were taken consecutively, to prevent any possible change in excess noise from changes in the setup. Once these were recorded and processed, the distribution of the noise floor values were plotted as shown in figure 5.5.

Figure 5.5 shows a Gaussian distribution with a peak at $\sim 373\,nV/\sqrt{Hz}$ and standard deviation of the data of $4.7\,nV/\sqrt{Hz}$. From theory the noise value was expected to be $\sim 376\,nV/\sqrt{Hz}$ which indicates that the theoretical value lies within the error of the experimental data. This suggests that when

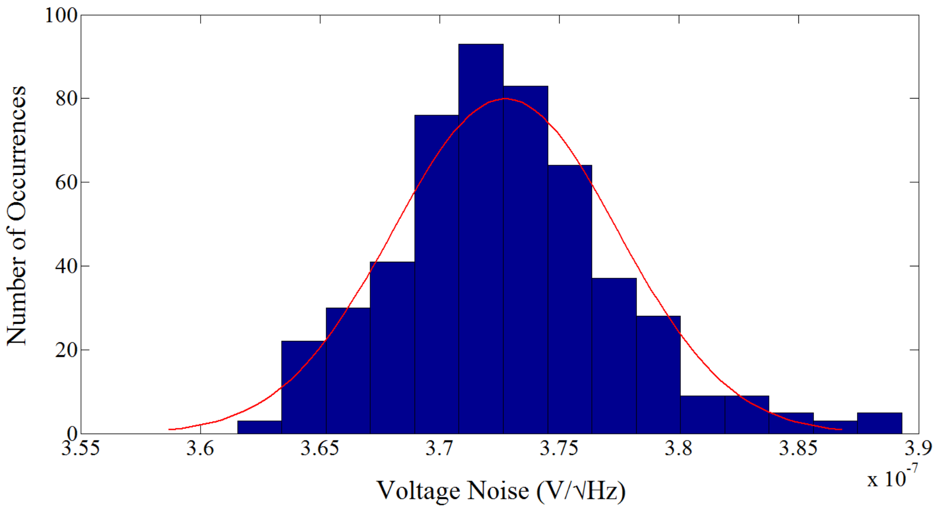

Figure 5.5: A plot of the distribution of ∼500 runs of the noise level of the thin film resistor at 330 K. The peak occurs at $\sim 373 \pm 4.7\, nV/\sqrt{Hz}$.

there is a thermal gradient across the resistor, the noise measued by the setup compares well with the theoretical value of the thermal noise and there is no evidence of excess noise. These results provided a reference frame for looking for excess noise when the system is in a non-thermal equilibrium condition. Taking these results into account, it is reasonable to assume that a noise level which was different from the theoretical noise by more than the error on the measurement, could have possibly indicated evidence of excess noise in the resistor.

5.5 High Temperature Tests

To further investigate the effects of thermal gradients on the noise levels in the thin film resistor, a range of noise spectra were taken at various temperatures to ascertain if excess noise can be seen when in a state of non-thermal equilibrium. To do this, the PID control was used to keep the resistor at a specified temperature to allow for a range of measurements to be taken. An issue that arose and required attention was excess noise caused by the power cables of the heater. When the PWM switched the transistor on and off, it was believed to be causing a current surge each time it switched which, in turn, created an electric field, inducing a current in the metals of the setup. This caused the noise level to be substantially higher than it should have been. To remedy this issue, the power cables were replaced with shielded coaxial cables both inside and outside of the vacuum chamber, which removed a large amount of the excess noise from the spectra. Subsequently, the data was recorded at temperatures from 300 K to 350 K in 10 K intervals with a thermal gradient of ∼ 6 K. At each temperature, 10 spectra were recorded at a frequency bandwidth of 2 kHz to 3 kHz. This bandwidth was chosen as additional unidentified noise had appeared in the spectrum since the previous data runs and this bandwidth contained the lowest level of excess noise at that time. The same process as used to record the room temperature measurements was used to analyse the high temperature data set. Each spectrum had external interference removed, and then a fit of the data was used to extract the value of the noise floor. This was done for each spectrum where an average of all spectra for that temperature was taken. Figure 5.6 shows a graph of both the theoretical values for the noise at various temperatures, and also the measured noise at each temperature.

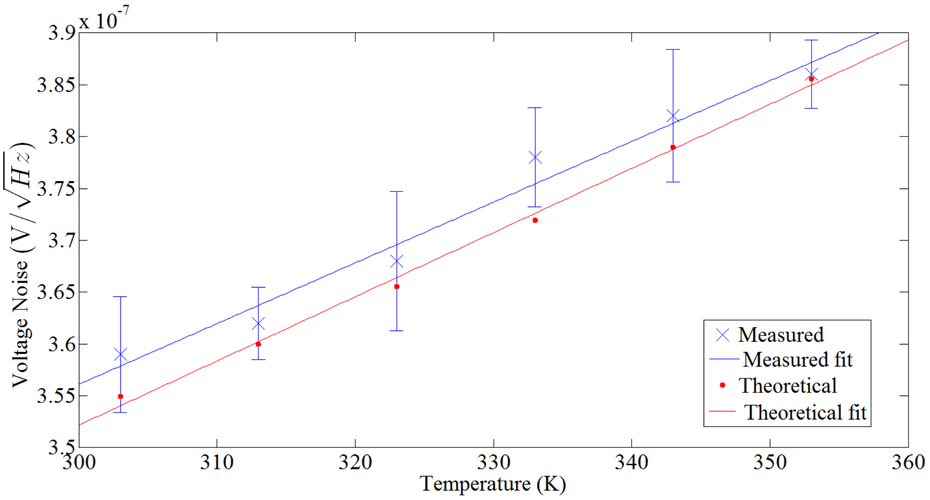

Figure 5.6: A plot of the theoretical and measured noise of the thin film resistor at various temperatures.

The measured noise was between 0.5 and $7\,nV/\sqrt{Hz}$ higher than the theoretical noise levels. As can be seen in figure 5.6, this still lies within the error of the measurement. This result implied that at higher temperature when the thermal gradient is small compared to the average value of the temperature, there did not appear to be any additional noise compared to the theory, assuming thermal equilibrium. Further analysis is required to understand the systematic shift in the data.

5.6 Conclusion

The initial noise spectra were recorded at room temperature with the intention of gaining an understanding of the performance of the experimental setup. Spectra were recorded with the sample resistor at room temperature, with no thermal gradient present, and also at higher temperatures with a thermal gradient of ∼6 K. The results of the analysis of the data with no gradient present produced a Gaussian spread of data to which the noise floor was shown to be $\sim 373 \pm 4.7\,nV/\sqrt{Hz}$. This compared favourably to the theoretical noise value of $376\,nV/\sqrt{Hz}$. This was corroborated when spectra of a range of temperatures provided noise floors that were comparable to the theoretical values within the error of the measurements. From this set of data, a reference frame was achieved which could be used to investigate whether there is excess noise in future cryogenic data compared to theoretical noise values.

Chapter 6

Cryogenic Temperature Results

6.1 Introduction

The next stage in this experiment was to cool the thin film resistor to cryogenic temperatures. By conducting the experiment with the temperature as close to liquid nitrogen temperatures as possible the thermal gradients achievable ($\sim$ 10 K) were much larger relative to the absolute temperature ($\sim$ 77 K) of the sample. This provided the opportunity to observe the noise levels in a non-thermal equilibrium system and investigate how that affected the Johnson noise. The effect of the non-thermal equilibrium state on the system is not well know, as such the aim of this experiment was to look for any consistent increase in the thermal noise above the theoretical noise value calculated through the johnson noise equation. If there were noise values that occurred above the systematic errors of the experiment then this could indicate the presence of excess noise.

6.2 Cryogenic Thermal Noise Calculations

As with the room temperature results, the effects of the thermal gradient on the total noise were calculated from theory for a temperature difference of 6 K across the resistor, at a temperature of 110 K. Using the method of splitting the resistor into a number of sections and assuming a contant temperature in each section, as explained in chapter 5, the total noise value was 239.9 $nV/\sqrt{Hz}$. Alternatively, calculating the noise from a single average temperature and resistance across the whole resistor gave a value of 239.5 $nV/\sqrt{Hz}$. Once more this shows a difference of less than 1 $nV/\sqrt{Hz}$ which allowed the use of average value calculations in the analysis.

6.3 Initial Tests

Before conducting full data runs, a number of tests to identify any unforeseen issues with the setup were performed. The main issue that had to be addressed was related to the vacuum. When the copper was placed into the liquid nitrogen, the flange that the copper bar was welded into was also cooling to very low temperatures of approximately 120 K. This was causing the rubber o-ring to solidify, breaking the seal and causing a slow leak. With this leak the vacuum could never get below $\sim 5 \times 10^{-3}$ mbar. A number of solutions were attempted to correct this problem such as wrapping the rubber in PTFE tape to attempt to reinforce the seal. Cryogenic grease was also placed around the rubber ring to attempt to maintain the seal which did not work. The final solution was to introduce enough heat into the flange to prevent the seal breaking but not enough to affect the copper inside. Due to the time restrictions on the project the solution was to use a heat gun placed at a distance to maintain a small heat flow onto the flange to prevent the seal from breaking. If there was more time available, a solution such as a resistance wire wrapped around the rubber o-ring would have been preferable as it would have been easier to maintain the minimum power required to keep the rubber from freezing while minimising any additional heat flow into the copper.

Another issue was related to the liquid nitrogen. Due to the surrounding room temperature environment and the copper bar itself, the nitrogen would evaporate at a steady rate. As a result the nitrogen had to be regularly replenished in the dewar which meant that long data runs that were usually left overnight were not possible. Additionally, replenishing the liquid nitrogen too fast could result in large jumps in temperature and cause the PID control to destabilise. This resulted in the data runs having to be kept to a small number of samples to maintain the control required.

6.4 110 k Cryogenic Data

During the time between the room temperature data runs and the cryogenic data runs, small alterations were made to the setup such as re-soldering broken wires and changing the coaxial cable between the circuit board and the spectrum analyser for a longer cable. As this could alter the noise levels another distribution measurement was taken to gain an average noise value at room temperature with no gradient present using this altered setup to verify if the alterations have changed the intrinsic noise level of the system.

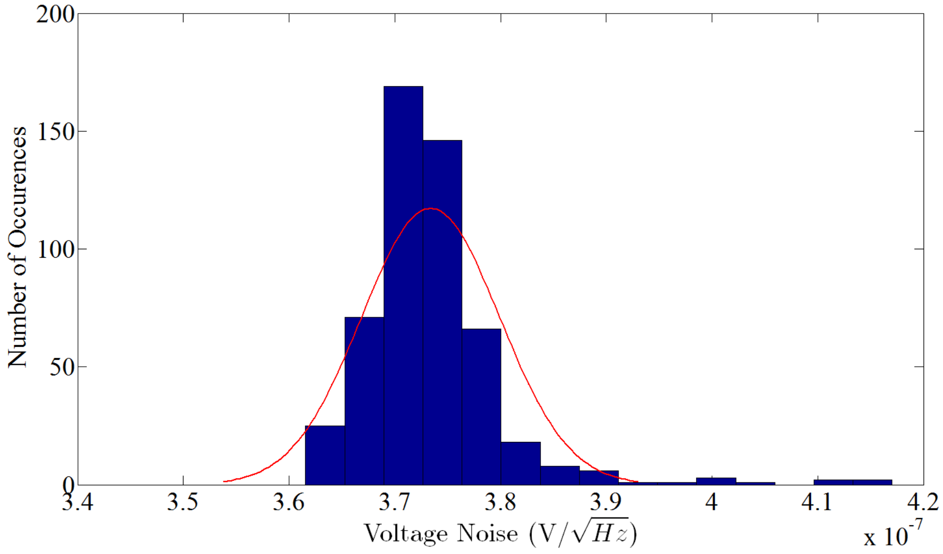

Figure 6.1: A plot of the distribution of 500 runs of the noise level of the sample resistor at room temperature. The peak occurs at $\sim 373 \pm 6.5\, nV/\sqrt{Hz}$.

This time the peak occurred at $\sim 373\, nV/\sqrt{Hz}$ with a standard deviation of 6.5 nV. This measured value is 25 nV higher than theory predicts. This suggests that the alterations had increased the intrinsic noise in the results and so must be taken into account in the future data.

To compare the room temperature results to the cryogenic results, 150 data runs were taken at a temperature of 110 K with a thermal gradient of ~6 K across the resistor. The purpose of these measurements was to look at the distribution of noise values. Ideally it would have been useful to take the same number of data runs for the low temperature measurements as the room temperature. This was not possible as maintaining the temperature at 110 K requires constant monitoring of the temperature and refilling of the dewar of liquid nitrogen so data could only be taken during the day.

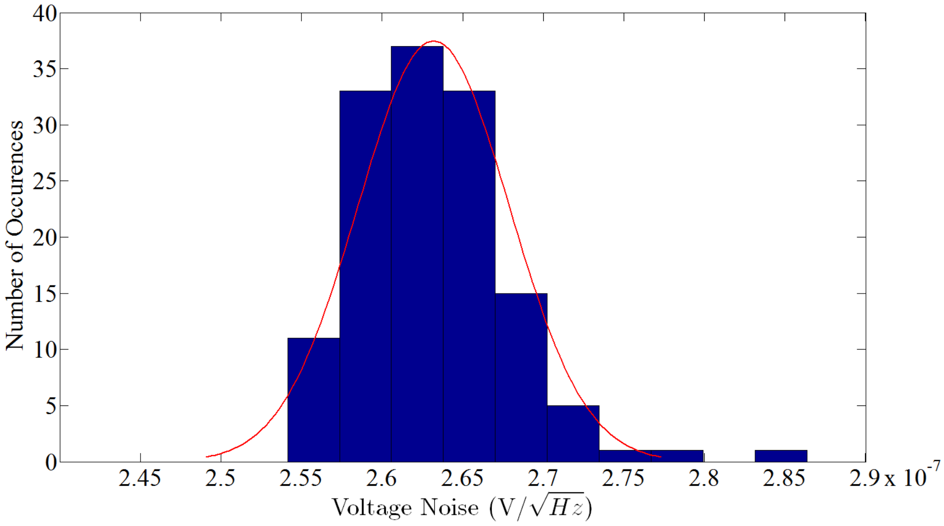

Figure 6.2: A plot of the distribution of ~150 noise level data runs of the sample resistor at ~110 K. The peak occurs at $\sim 263 \pm 4.7nV/\sqrt{Hz}$.

As with the room temperature data, the cryogenic results in figure 6.2 show a Gaussian distribution with the peak occurring at $\sim 263nV/\sqrt{Hz}$ with a standard deviation of $4.7nV/\sqrt{Hz}$. The expected value for the noise calculated from theory was $\sim 239nV/\sqrt{Hz}$ which results in the noise floor being $\sim 20nV$ higher than the expected theoretical value. This indicates that with the additional noise introduced from the alterations mentioned previously, the measured noise lies within the error of the theoretical value and suggests that there was no excess noise present.

6.5 Low Temperature Results

The next stage of the investigation was to take a range of noise floor measurements for various cryogenic temperatures. Temperatures ranging from 124 K to 170 K were recorded in a similar manner to the high temperature data. The sample resistor was set to the required temperature and 10 runs of each temperature were recorded, analysed to remove external noise and averaged to produce a value for the noise level at that temperature.

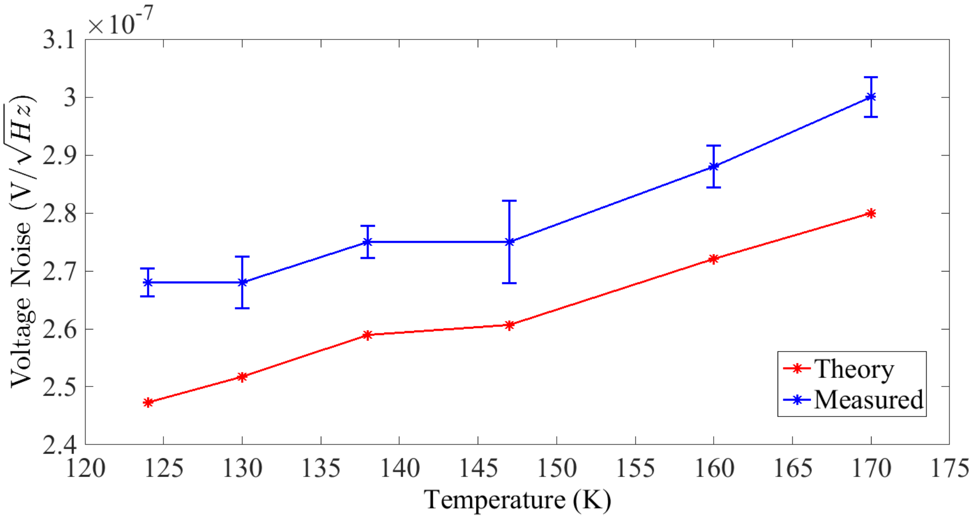

Figure 6.3: A plot of voltage noise for a number of cryogenic temperatures.

Figure 6.3 shows a plot of the voltage noise for various temperatures. Each measured value is 14-21nV/$\sqrt{Hz}$ above the theoretical values which agrees well with the previous cryogenic measurement. This result indicated that the theoretical value for the noise lay within the error of the experimental value, once the excess noise form the alterations to the setup were taken into account.

6.6 Conclusion

When transitioning to cryogenic measurements there were a number of issues that had to be addressed. One of these issues was the design of the setup causing the rubber seal on a flange to solidify and develop a slow leak in the vacuum system. This issue was solved by adding enough heat into the flange to prevent the rubber from solidifying but not adding any significant heat into the copper bar. Once the issues were identified and addressed, a number of data runs were carried out. As there were minor alterations to the setup another room temperature data run with no gradient present was performed and the noise floor produced by that data was $\sim 20nV$ higher than expected. This lead to the conclusion that the minor alterations to the setup increased the intrinsic noise in the circuit. The results produced by the cryogenic measurements stated that the noise floor with a gradient present was $\sim 263 \pm 4.7\,nV/\sqrt{Hz}$ which was $\sim 20\,nV$ higher than expected which, when compensating for the $\sim 20\,\mathrm{nV}$ increase due to alterations, the theoretical noise lay within the error of the experimental results.

Taking this into account the data suggests that there was no evidence of excess noise at cryogenic temperatures when there was a temperature difference of 6 K across a resistor with an absolute temperature of 110 K. This nul result provides a limiting factor for a thermal gradient that will not create excess thermal noise above the theoretically calculated levels. Further investigation is required to further constrain thermal gradient levels that will maintain the validity of the fluctuation dissipation theorem.

Chapter 7

Conclusions

As current interferometric gravitational wave detectors reach their design sensitivity, it is now only a matter of time before the first direct detection of gravitational waves occurs. Despite this, research will continue into methods to upgrade current interferometers and to further reduce noise, thereby increasing their detection range. Some of the next generation of interferometers, such as KAGRA, are designed to operate at cryogenic temperatures. This opens up an area of investigation as there are still aspects of non-equilibrium systems that are not well understood.

The current method of calculating the thermal noise in an interferometers is to use the fluctuation-dissipation theorem (FDT). This theorem requires the system to be in thermal equilibrium, which is a valid assumption for room temperature detectors. The aim of this experiment was to investigate if the FDT is still valid when the system it is being used to analyse is no longer in thermal equilibrium, such as a cryogenic temperature detector where the thermal gradient is comparable to the absolute temperature.

In this experiment, instead of looking at thermal noise in a mechanical system, an electrical method was devised. By measuring the Johnson noise of a thin film resistor, which is temperature dependent, with and without the presence of a thermal gradient, it was possible to compare the noise values to look for any variations due to the thermal gradient. As the effects of a thermal gradient on a system are not fully understood, this experiment concentrated on looking for excess noise that occured above the statistical errors of the set up. If there were noise levels which were consistently higher than the theoretical noise levels, then that would indicate the presence of excess noise. There were many different aspects of the experiment that had to be taken into consideration during the design process. The signal from the Johnson noise had to be amplified to a level that was measurable and the design of the thin film resistor needed to provide a method of inducing a thermal gradient across it. The development of a control system was also required to monitor and control the heater, in order to produce the required thermal gradients at different temperatures.

The results that were produced in this thesis indicated that there was no excess noise produced. When maintaining a thermal gradient of 6 K across the resistor at a temperature of 330 K, the Johnson noise was measured to be $373 \pm 4.7nV/\sqrt{Hz}$ compared to the theoretical value of $376 \pm 4.7nV/\sqrt{Hz}$. This indicates that there was no excess noise when the resistor was under a small thermal gradient relative to the absolute temperature.

Further tests were conducted for a low temperature of 110k with a 6 K thermal gradient. In this result, the measured Johnson noise was measured to be $263 \pm 4.7nV/\sqrt{Hz}$ compared to the theoretical value of $239nV/\sqrt{Hz}$. This result appeared to indicate an excess of $20nV/\sqrt{Hz}$ but due to alterations to the experimental setup, room temperature results were repeated with no thermal gradient to determine if this result was correct. The room temperature results produced a Johnson noise that was also $\sim 20nV/\sqrt{Hz}$ higher than the theoretical value. This implies that the alterations to the setup caused an increase of $\sim 20nV/\sqrt{Hz}$ to each measurement and therefore the low temperature results did not show any excess noise due to the present of a thermal gradient. This nul result provides a limiting factor for the level of thermal gradient where the fluctuation dissipation theorem remains valid. This could be further constrained with additional investigations and improvements to the current setup.

There are a number of areas that could be improved upon in future attempts at this experiment. Placing the copper bar into an established cryostat would improve the environment that the thin film resistor would be observed in, allowing for a greater control of both the pressure surrounding the resistor and the temperature of the resistor itself. By using higher accuracy thermometers and a greater number of them, a more complete picture of the thermal gradient would have been possible. This could allow for a higher level of control of the heater allowing for more accurate temperature measurements. A redesign to the dimensions of the resistor could allow for the thermal gradient to have a greater effect. This could involve increasing the length of the resistor or by designing a folded track with multiple passes through the thermal gradient to increase any possible effect on the Johnson noise.

With interferometric detectors reaching greater sensitivities, the first direct detection of gravitational waves is just over the horizon. This detection will begin a new age in astronomy and open a new window for which to observe the universe.

Appendix A

PID Labview Code

The labview code shown in this section was written to control the feedback system used to maintain the thin film resistor at the correct temperature. The code involved interfacing with an Arduino board which is used to control the power supplied to the heater, and to a keithley 2000 multimeter which was used to measure the temperature of the thin film resistor using platinum resistance thermometers. A section of the code is a programmed PID controller and was provided by Dr. Giles Hammond. The code reads the temperature of the thin film resistor and calculates the power required to heat or cool the thin film resistor to the stated set point temperature. There is also a section of the code which records the temperature of the thin film resistor and also states the thermal gradient which is present across the resistor.

Shown below are the ”front panel” and the ”block diagram” which are the user interface and the program code respectively.

A.1 Front Panel

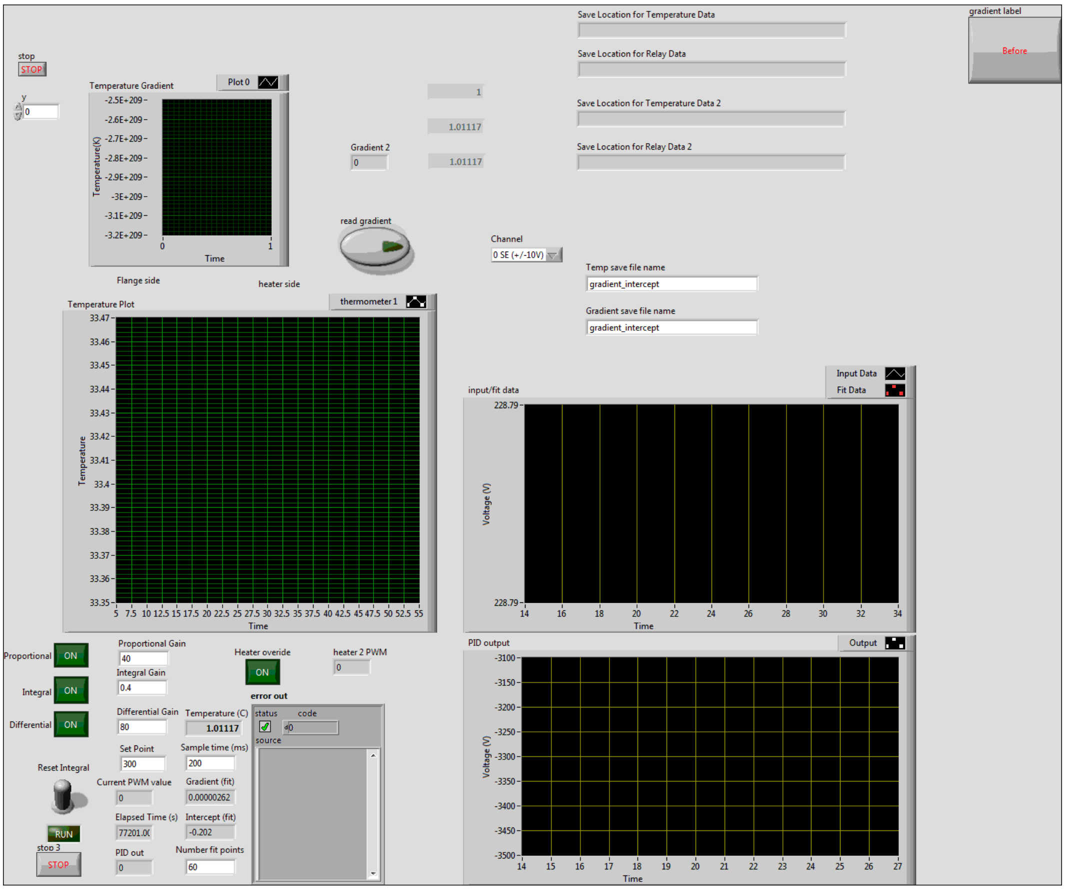

y: 0

Gradient 2: 0

1

1.01117

1.01117

Channel: 0 SE (+/-10V)

Temp save file name: gradient_intercept

Gradient save file name: gradient_intercept

Proportional: ON

Integral: ON

Differential: ON

Proportional Gain: 40

Integral Gain: 0.4

Differential Gain: 80

Set Point: 300

Current PWM value: 0

Elapsed Time (s): 77201.0(

PID out: 0

Temperature (C): 1.01117

Sample time (ms): 200

Gradient (fit): 0.00000262

Intercept (fit): -0.202

Number fit points: 60

Heater overide: ON

heater 2 PWM: 0

error out: status ☑ code 0

A.2 Block Diagram

The following section of code is where the feedback PID controller and the arduino loop which controls the power level of the heater through a PWM technique.

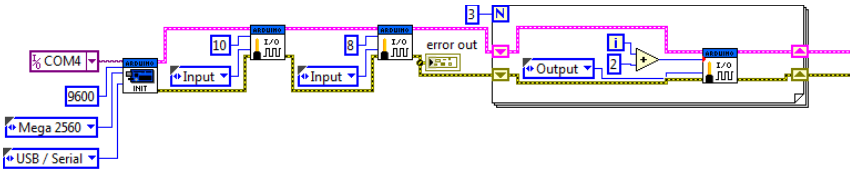

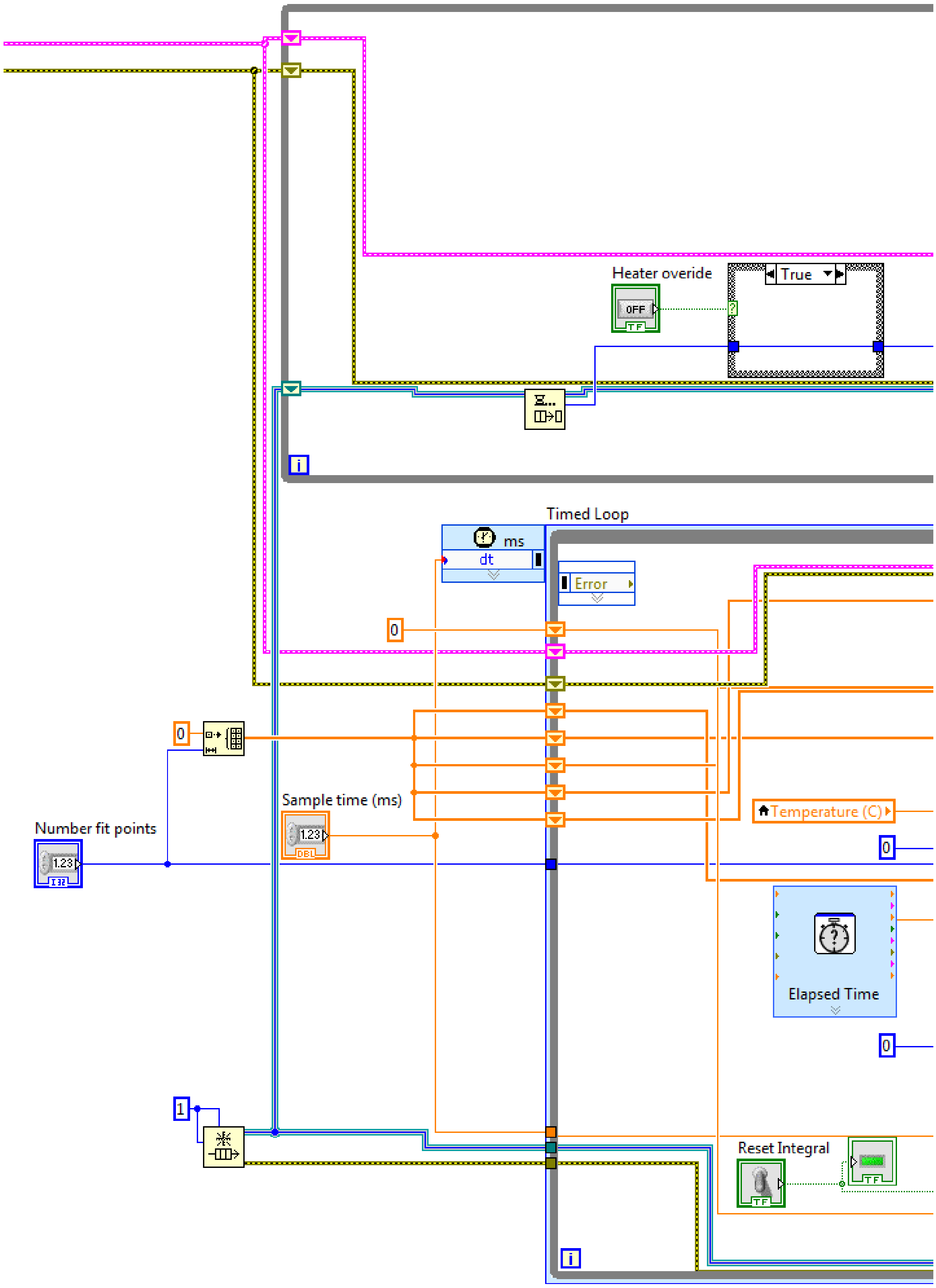
Heater overide
OFF
True
i
Timed Loop
ms
dt
Error
0
0
Sample time (ms)
1.23
DBL
Number fit points
1.23
I32
Temperature (C)
0
Elapsed Time
0
1
Reset Integral
i

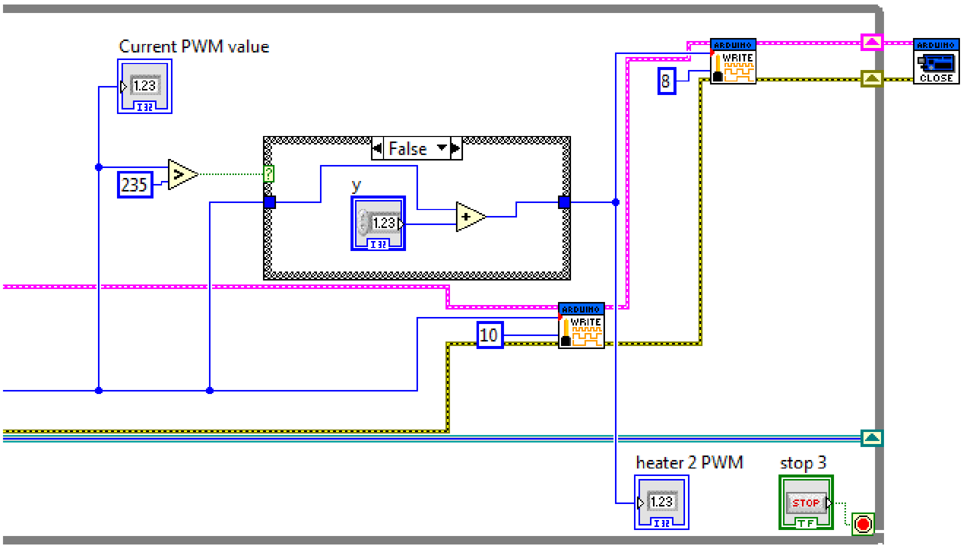
Current PWM value
1.23
I32
235
False
y
1.23
I32
8
ARDUINO
WRITE
ARDUINO
CLOSE
ARDUINO
WRITE
10
heater 2 PWM
1.23
I32
stop 3
STOP
TF

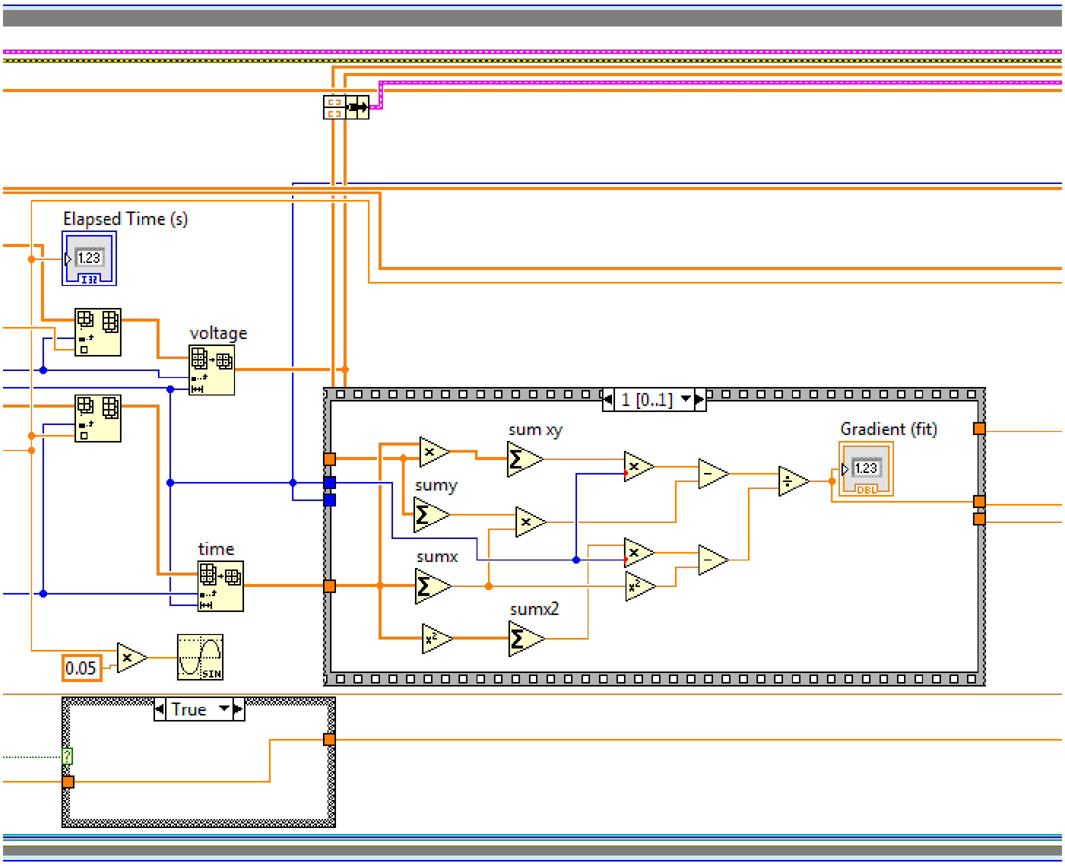
Elapsed Time (s)
1.23
I32
voltage
time
0.05
SIN
1 [0..1]
sum xy
sumy
sumx
sumx2
Gradient (fit)
1.23
DBL
True

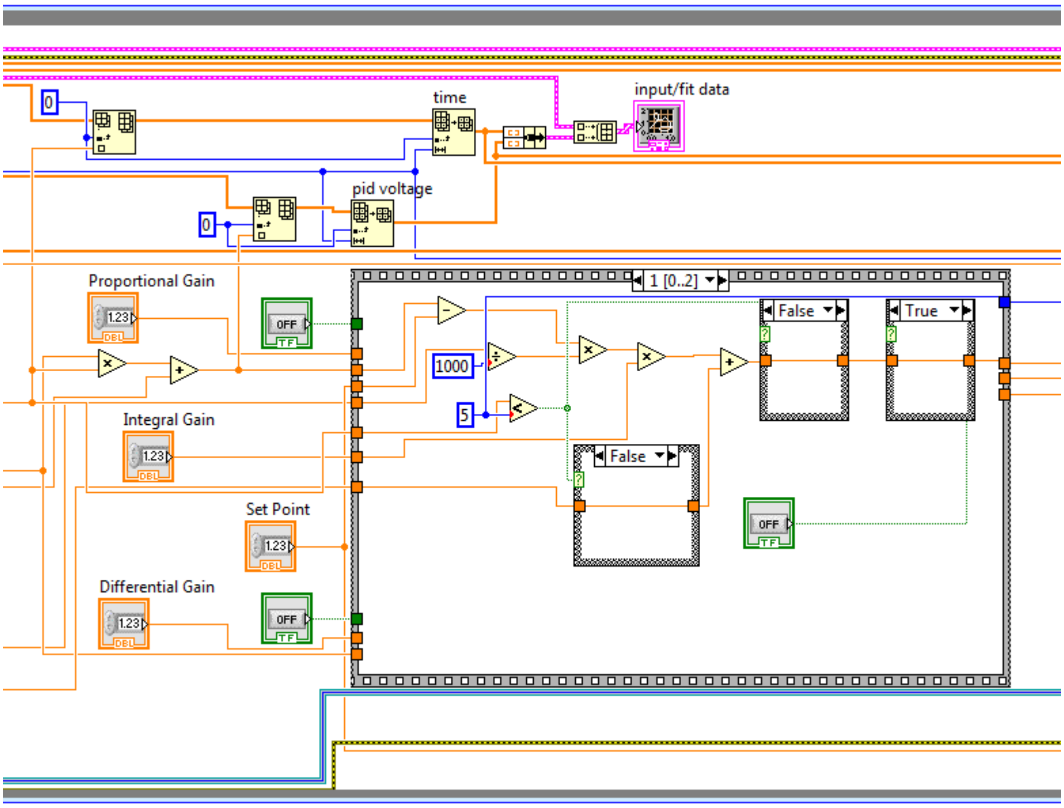
0
time
input/fit data
pid voltage
0
1 [0..2]
Proportional Gain
1.23
DBL
OFF
TF
1000
5
False
True
Integral Gain
1.23
DBL
False
OFF
TF
Set Point
1.23
DBL
Differential Gain
1.23
DBL
OFF
TF

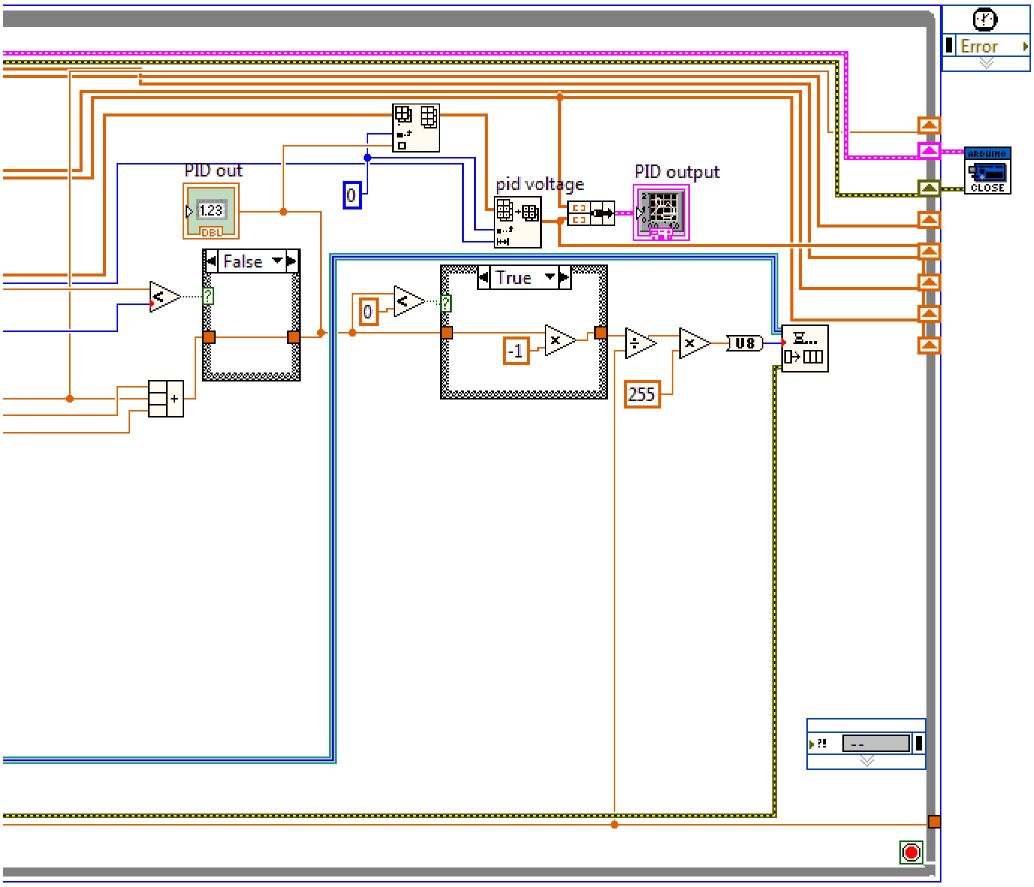
Error
PID out
1.23
DBL
0
pid voltage
PID output
False
True
0
-1
255
U8
ARDUINO
CLOSE

This section of the code controls the Keithley multimeter and records the temperture of the Thin film resistor. It also relays the values into the PID section of the code. It can either record the value of both the resistors to measure the thermal gradient or it can monitor the temperature of one thermometer.

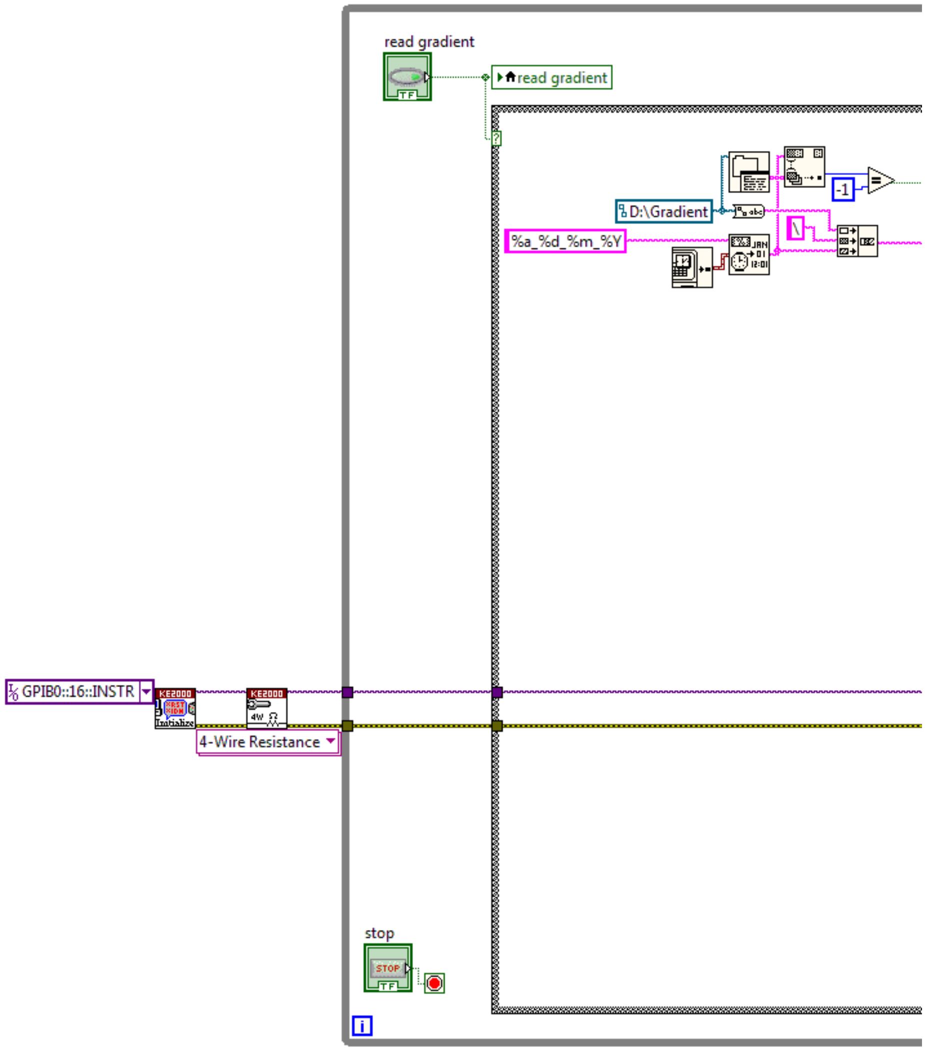

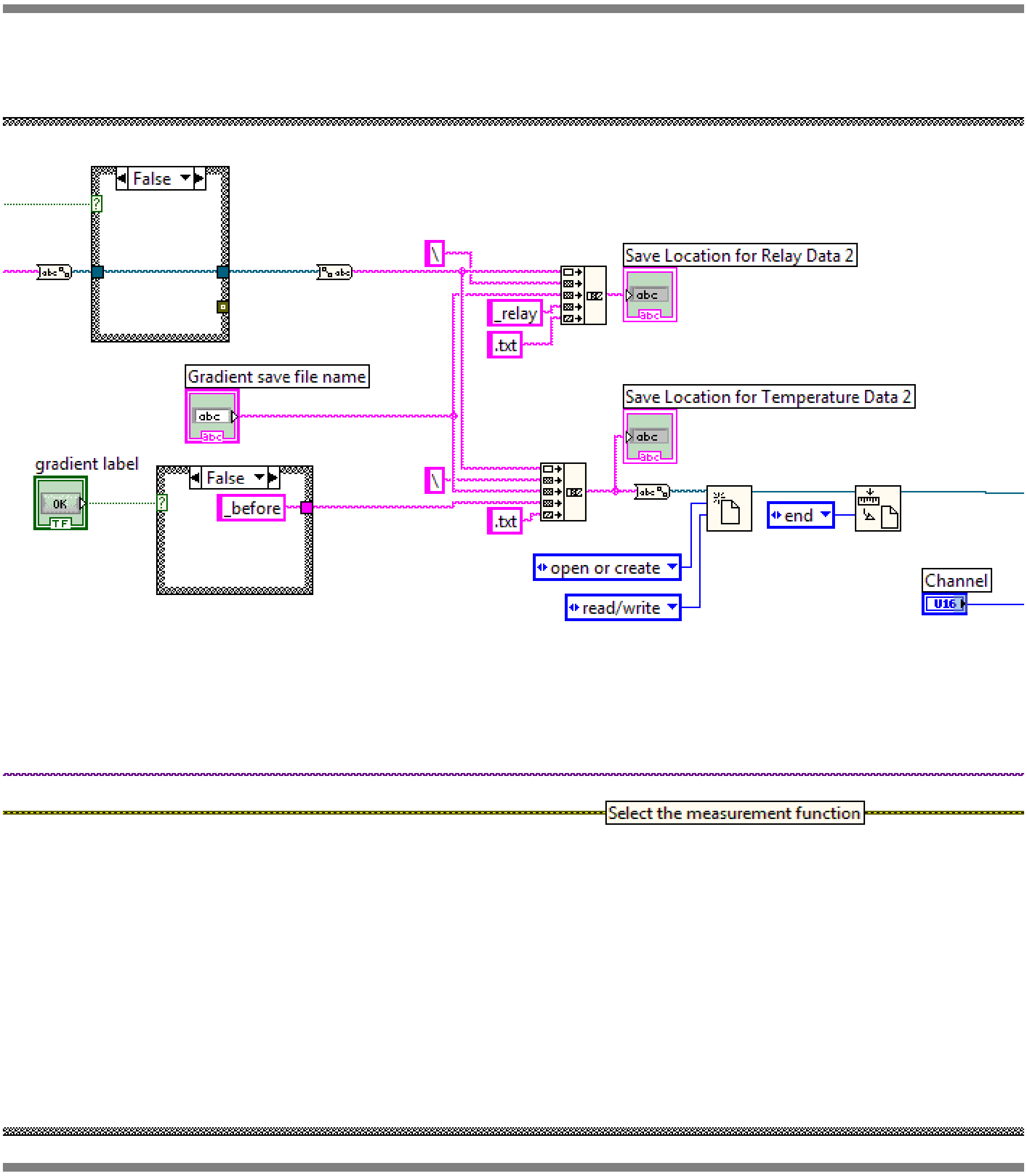
False
Save Location for Relay Data 2
_relay
.txt
Gradient save file name
Save Location for Temperature Data 2
gradient label
OK
False
_before
.txt
open or create
read/write
end
Channel
U16
Select the measurement function

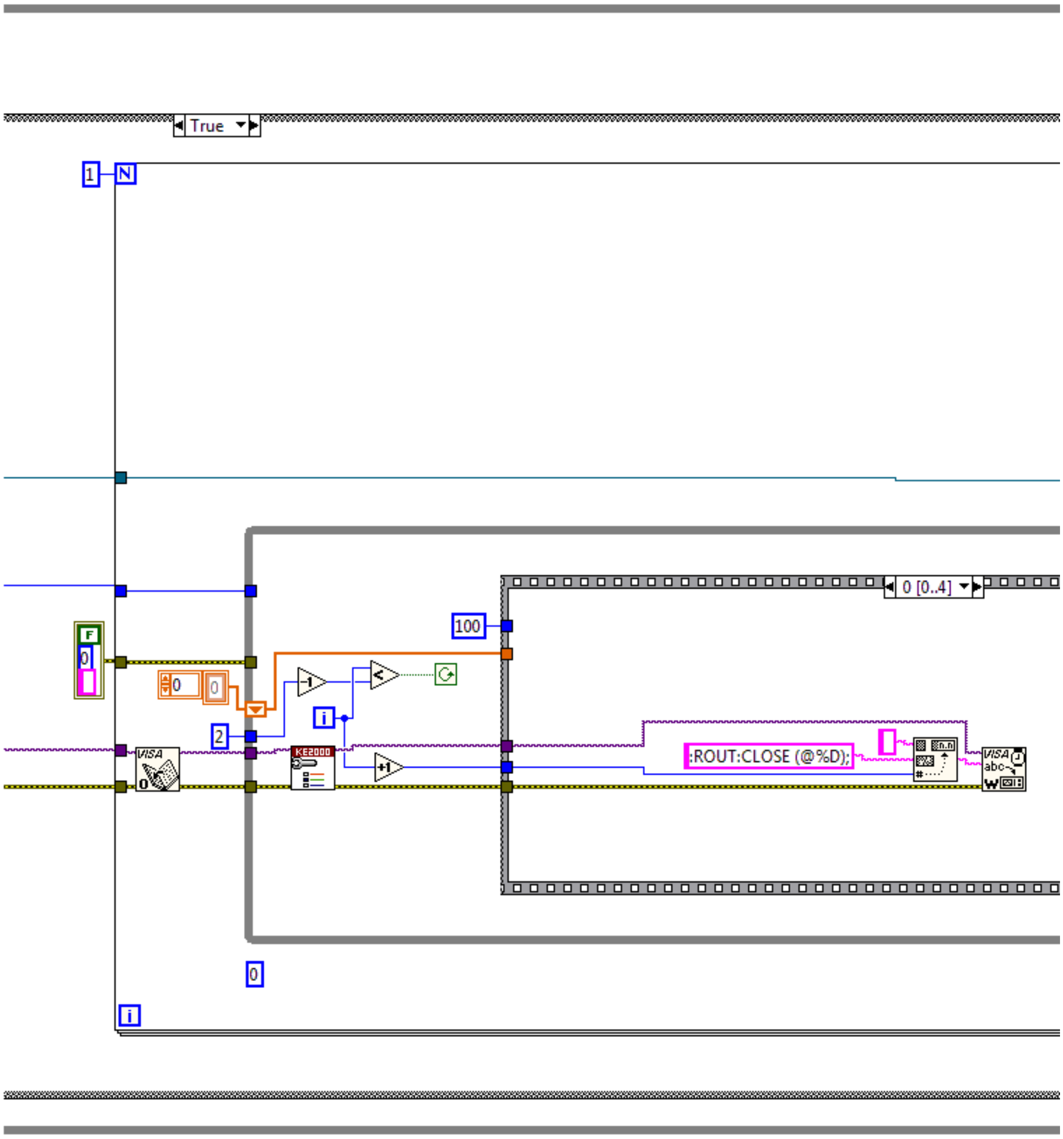
True
1
N
F
0
0
0
2
i
VISA
0
KE2000
-1
+1
100
0 [0..4]
:ROUT:CLOSE (@%D);
VISA
abc
W
0
i

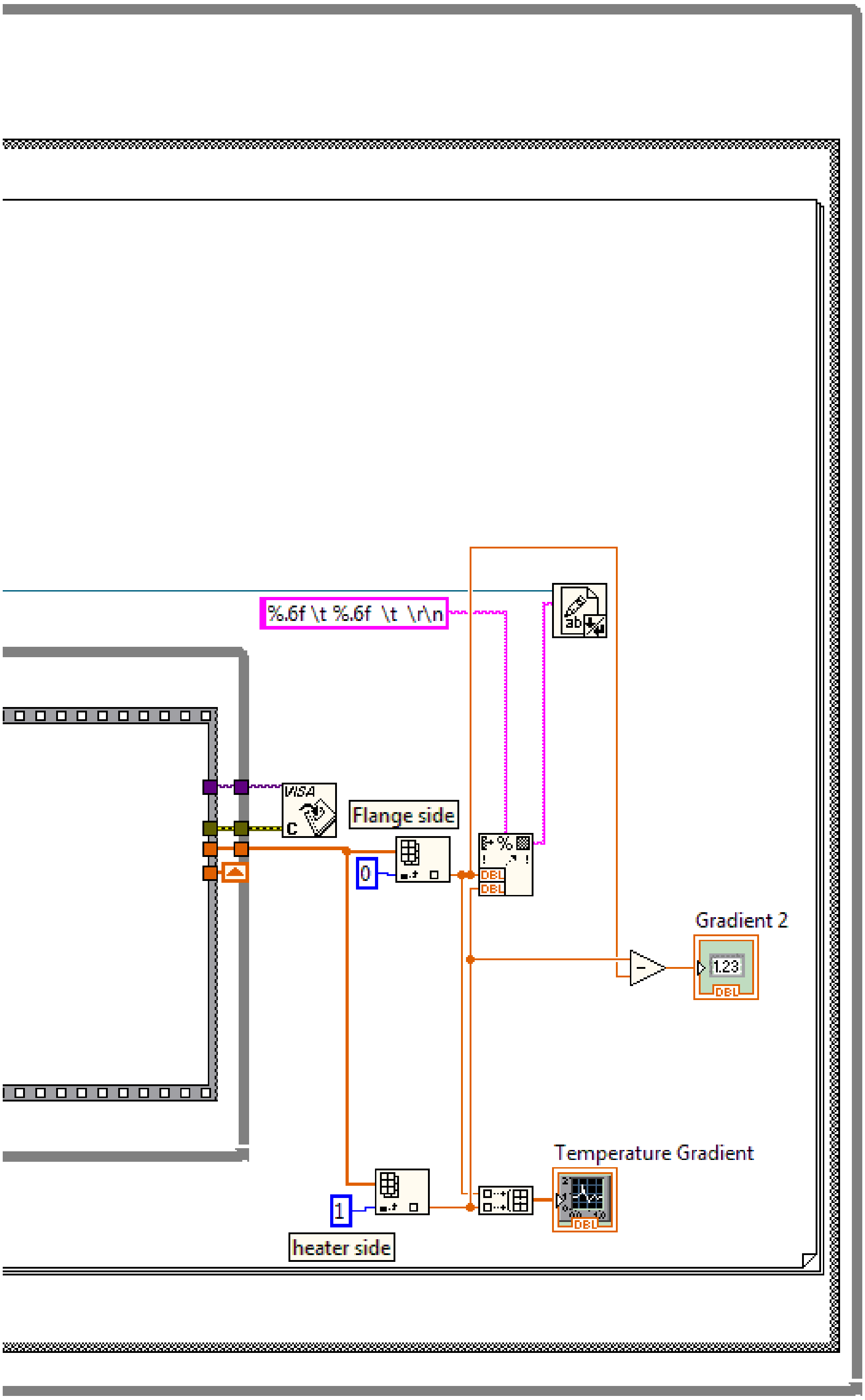
%.6f \t %.6f \t \r\n
VISA
C
Flange side
0
DBL
DBL
Gradient 2
1.23
DBL
1
heater side
Temperature Gradient
DBL

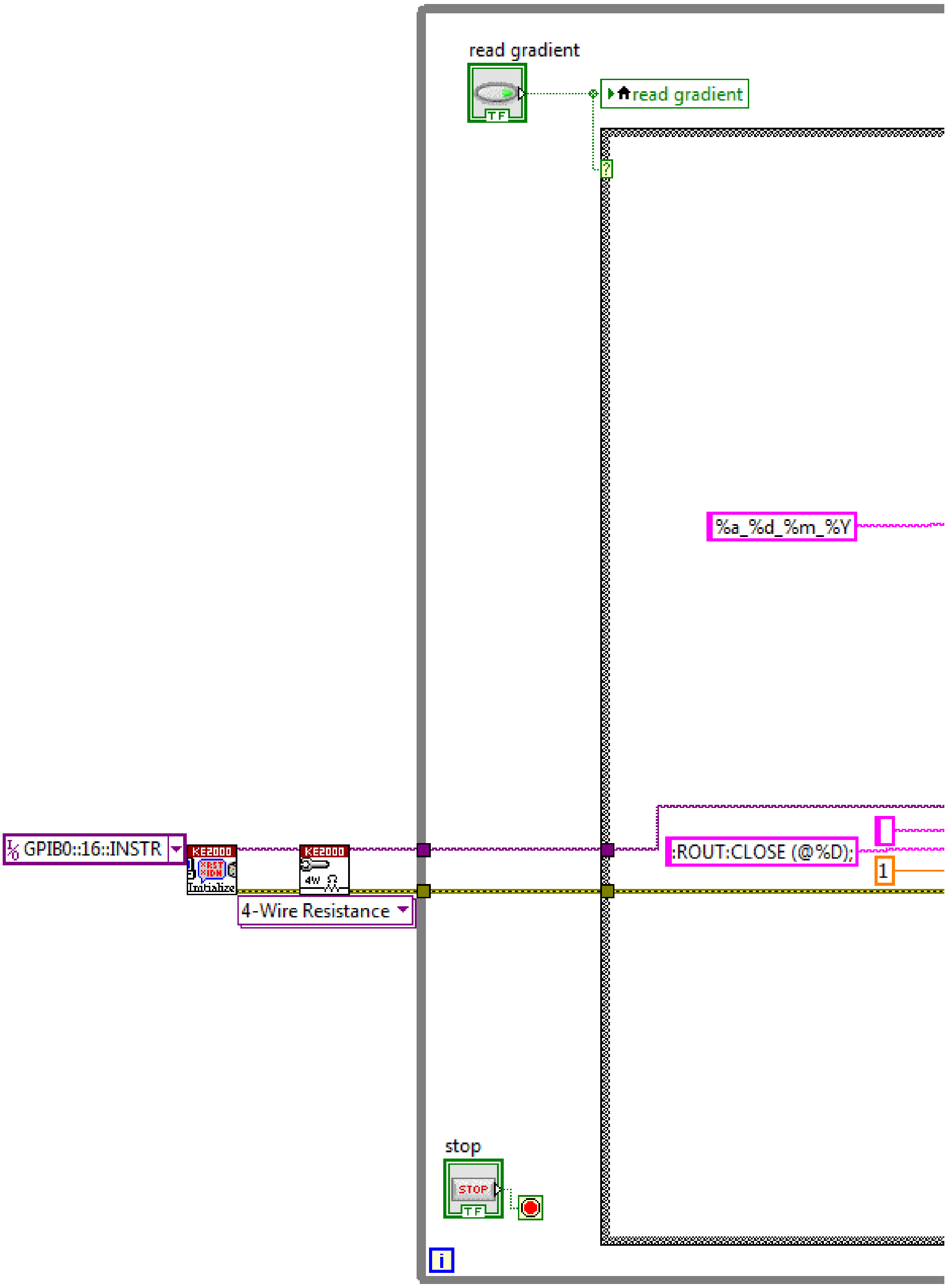
read gradient
read gradient
%a_%d_%m_%Y
GPIB0::16::INSTR
KE2000
Initialize
KE2000
4W
4-Wire Resistance
:ROUT:CLOSE (@%D);
1
stop
STOP
TF
i

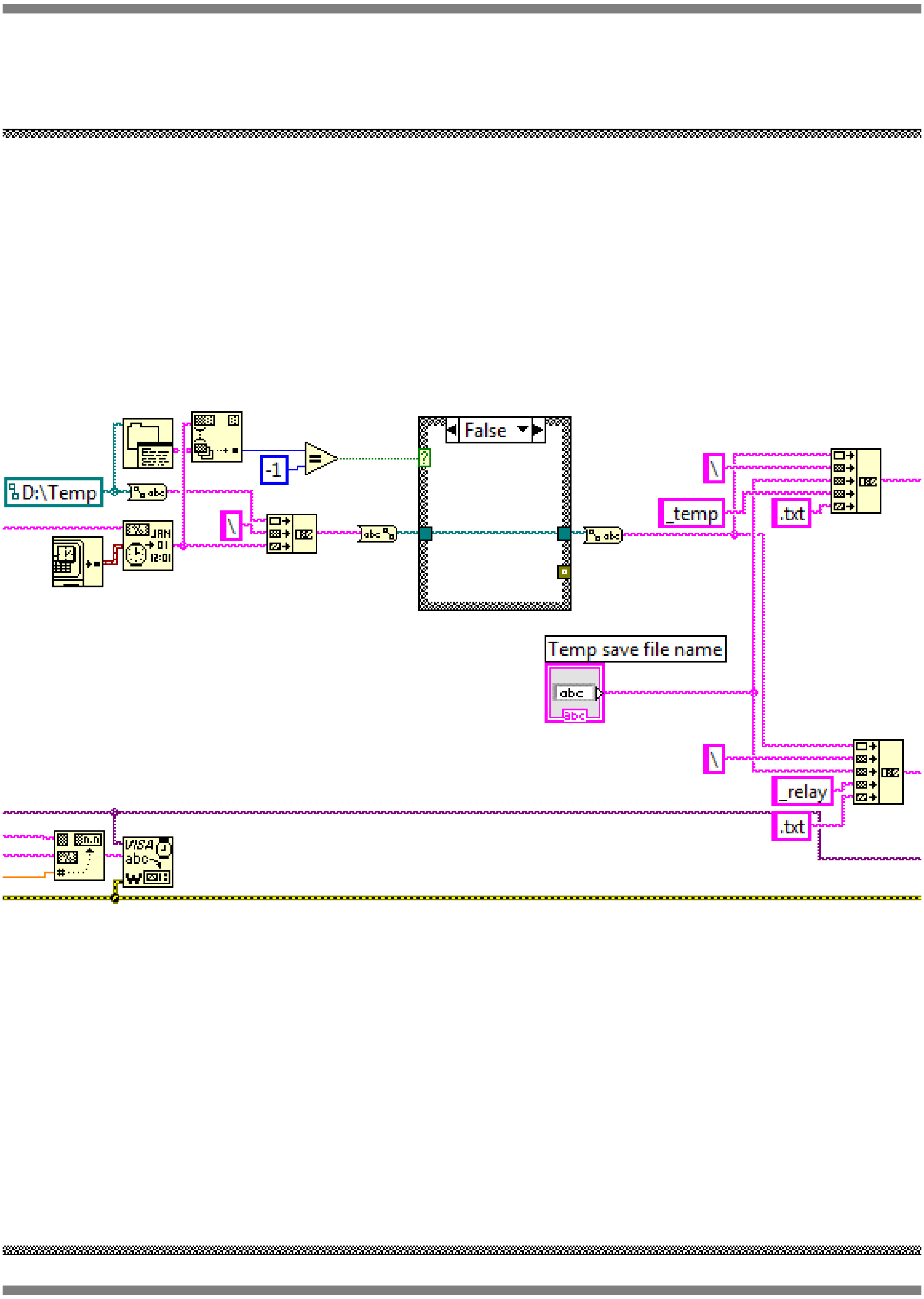
False
D:\Temp
-1
\
_temp
.txt
Temp save file name
abc
\
_relay
.txt
VISA
abc

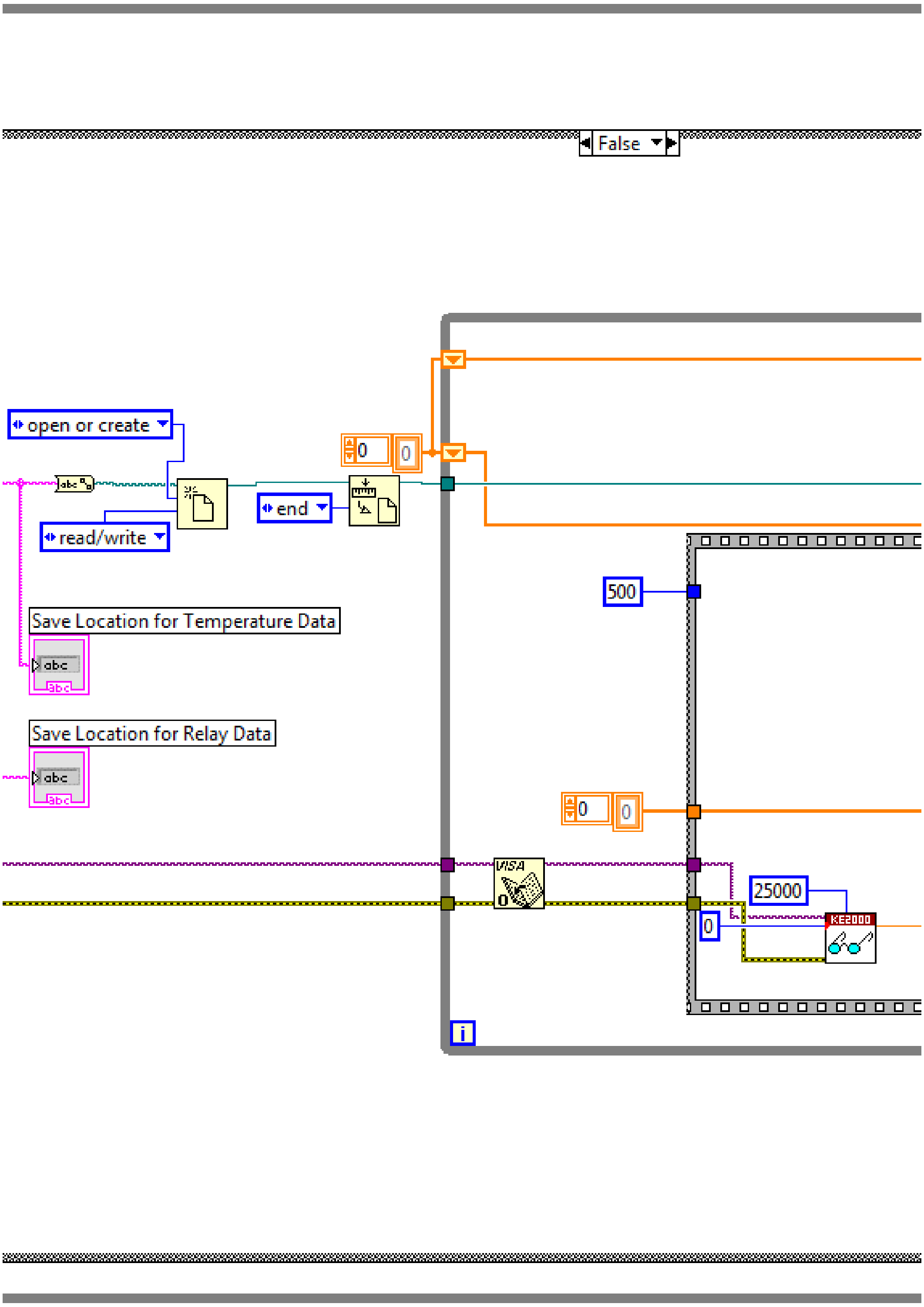
False
open or create
read/write
end
Save Location for Temperature Data
Save Location for Relay Data
0
0
500
0
0
VISA
0
25000
0
KE2000
i

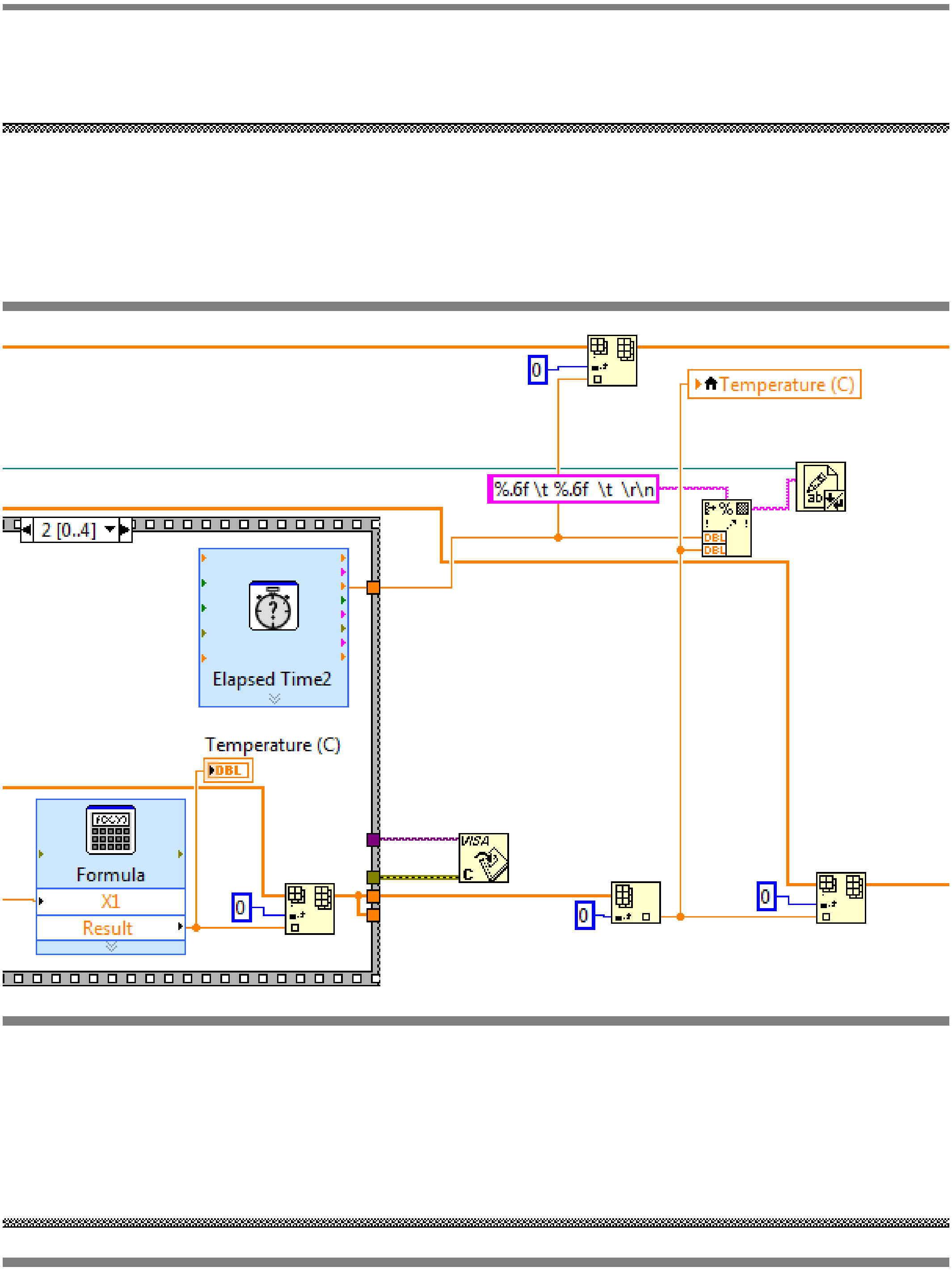
0
Temperature (C)
%.6f \t %.6f \t \r\n
2 [0..4]
Elapsed Time2
Temperature (C)
DBL
DBL
DBL
VISA
C
Formula
X1
Result
0
0
0

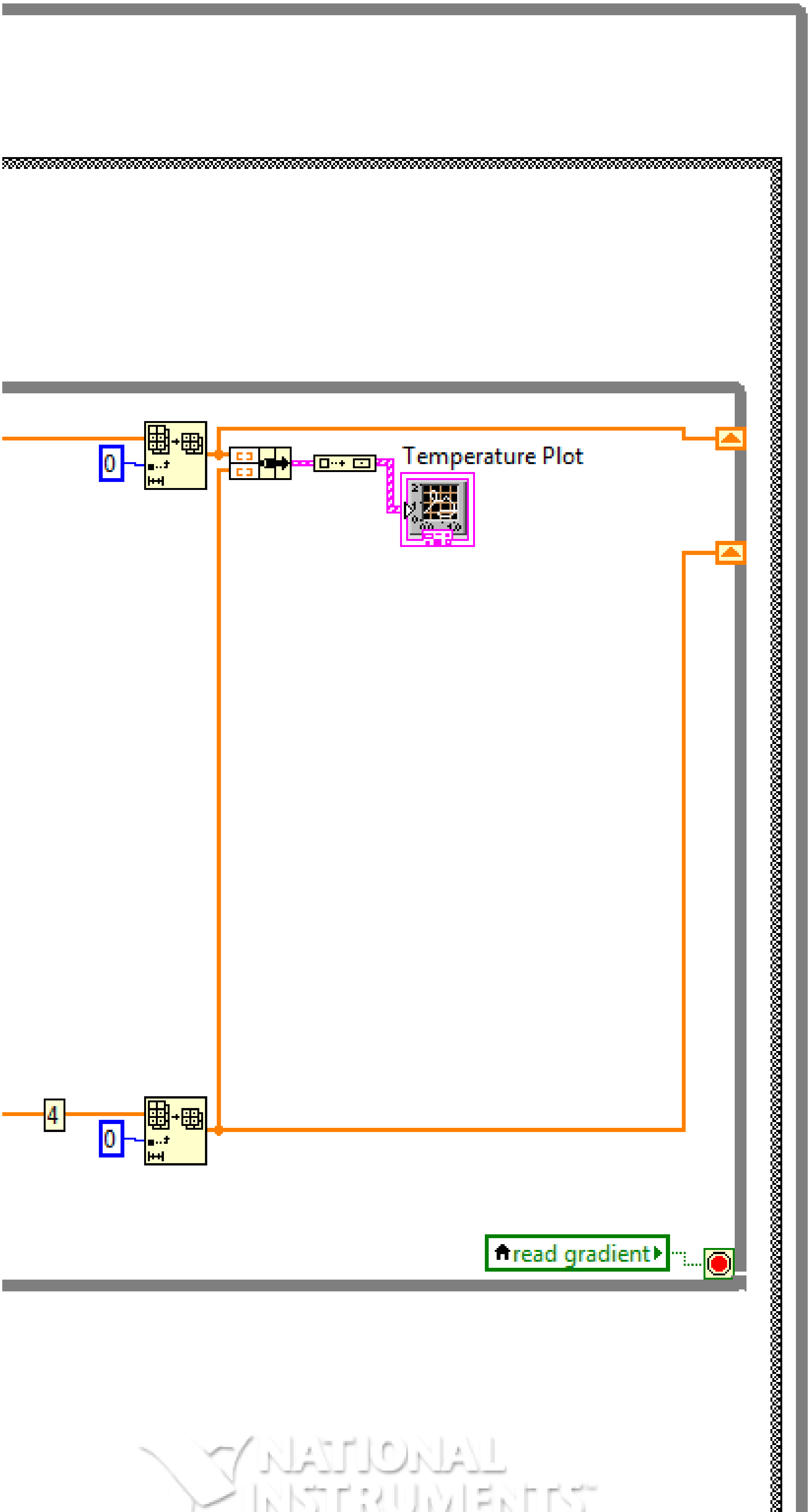
Temperature Plot
0
4
0
read gradient
NATIONAL INSTRUMENTS

A.3 Hidden frames

The following are the subframes of the loops seen in the previous section, displayed in order.

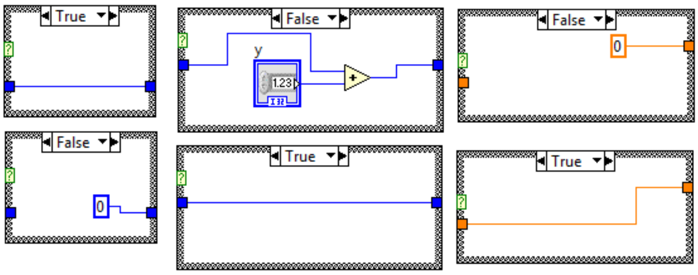

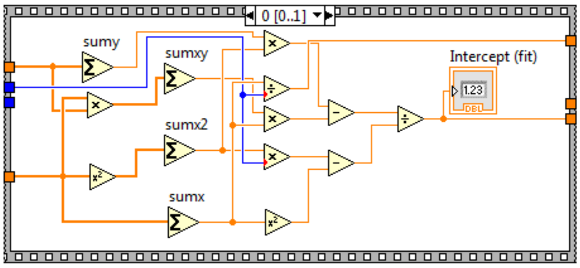

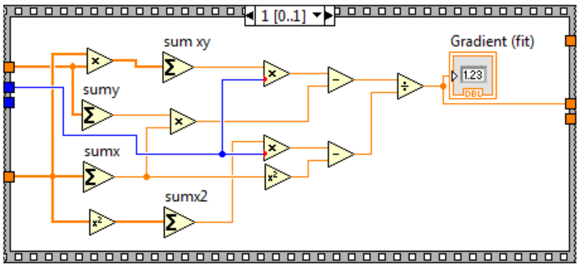

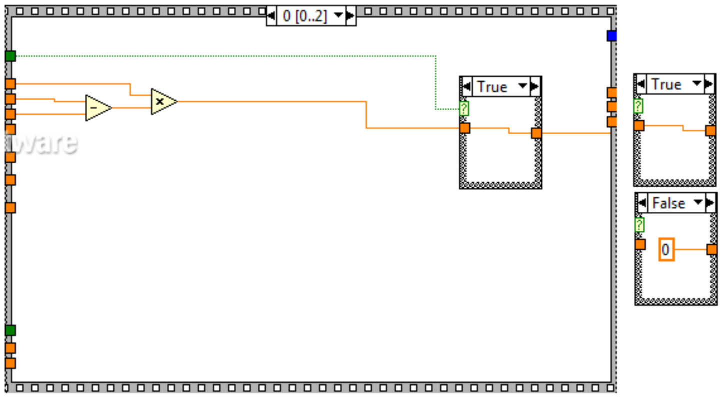

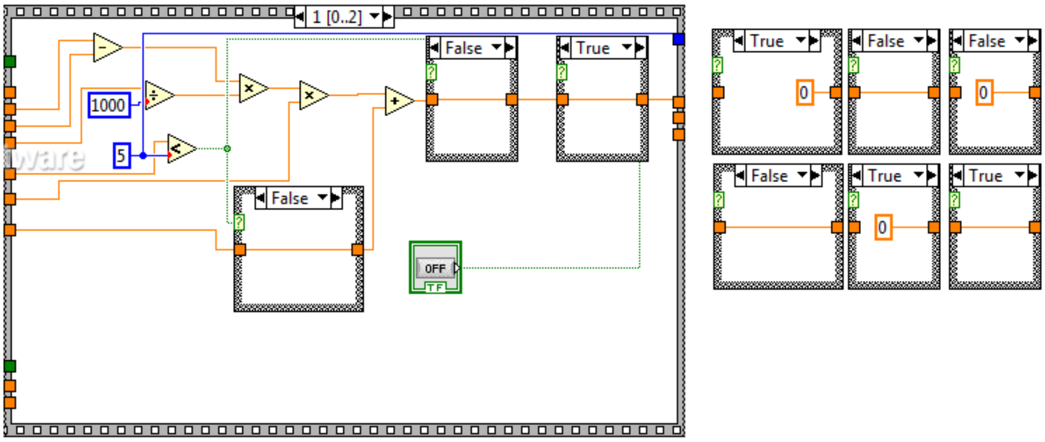
1 [0..2]
1000
5
False
True
False
OFF
TF
True
False
False
False
True
True
0
0
0

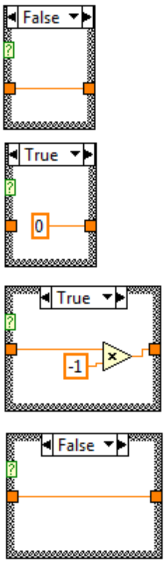
False
True
0
True
-1
False

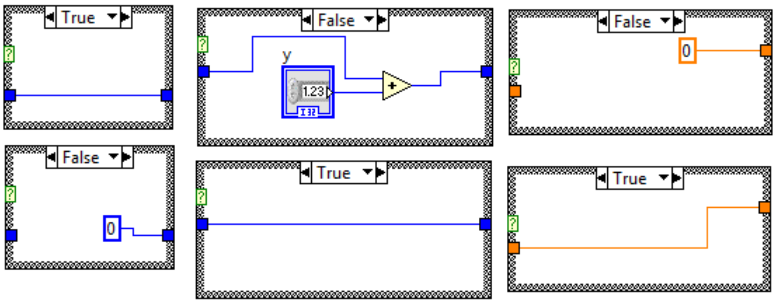
True
False
y
1.23
+
False
0
False
0
True
True

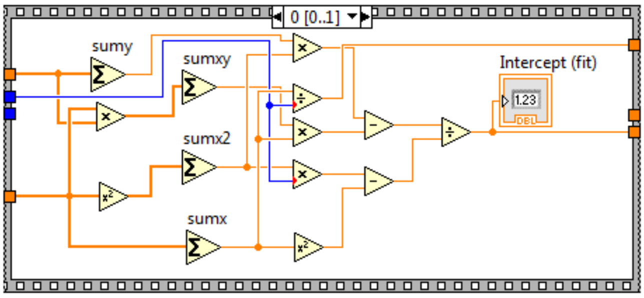
0 [0..1]
sumy
sumxy
sumx2
sumx
Intercept (fit)
1.23
DBL

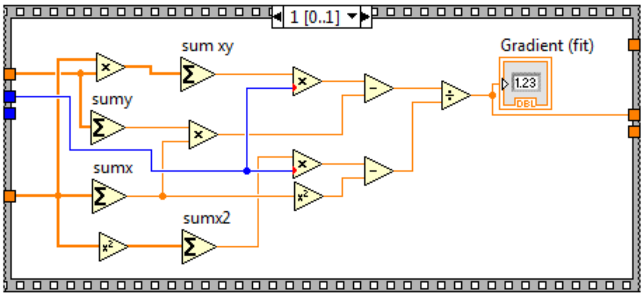
1 [0..1]
sum xy
sumy
sumx
sumx2
Gradient (fit)
1.23
DBL

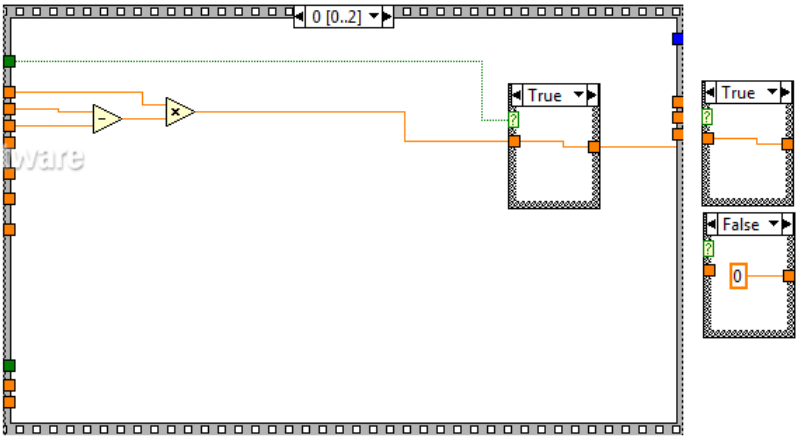
0 [0..2]
True
True
False
0

Appendix B

Agilent Spectrum Analyzer interface code

The labview code used to remotely control the Agilent spectrum analyzer was downloaded from the National Instruments website [69]. Alterations were made to the code, such as adding a function to run multiple runs in a row and save a data file for each run. Controls such as the frequency bandwidth and resolution were placed on the front panel to allow for a higher degree of control in the recording of the data.

Shown below are the ”front panel” and the ”block diagram” which are the user interface and the program code respectively.

B.1 Front Panel

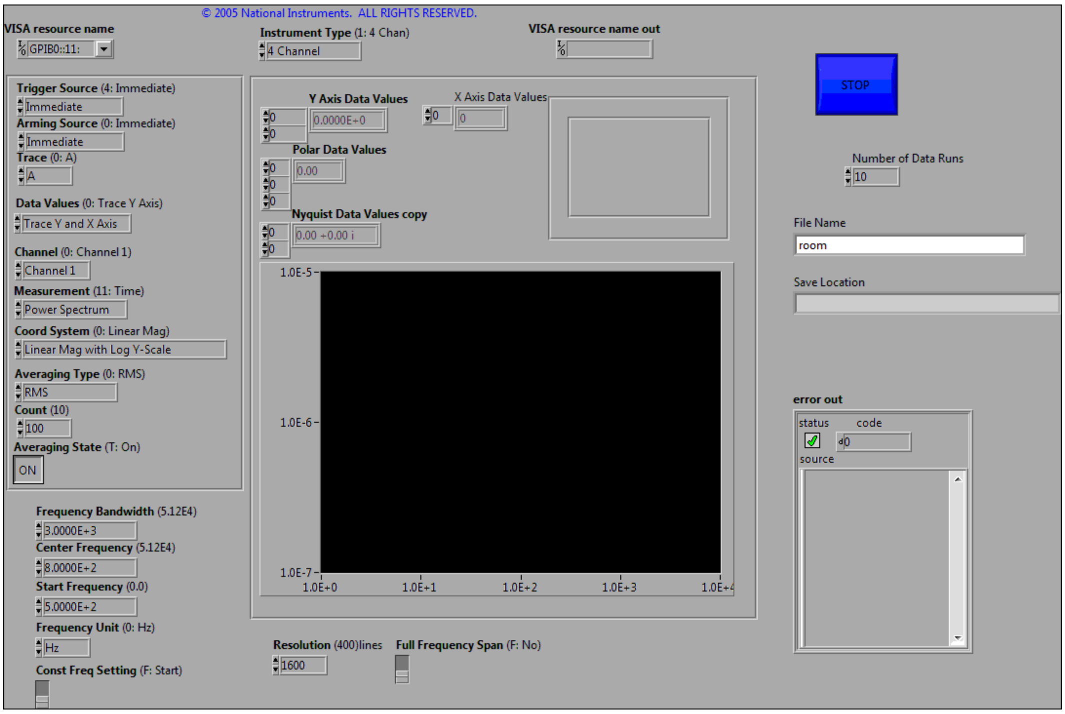

VISA resource name GPIB0::11:

Instrument Type (1: 4 Chan) 4 Channel

VISA resource name out

Trigger Source (4: Immediate) Immediate

Arming Source (0: Immediate) Immediate

Trace (0: A) A

Data Values (0: Trace Y Axis) Trace Y and X Axis

Channel (0: Channel 1) Channel 1

Measurement (11: Time) Power Spectrum

Coord System (0: Linear Mag) Linear Mag with Log Y-Scale

Averaging Type (0: RMS) RMS

Count (10) 100

Averaging State (T: On) ON

Frequency Bandwidth (5.12E4) 3.0000E+3

Center Frequency (5.12E4) 8.0000E+2

Start Frequency (0.0) 5.0000E+2

Frequency Unit (0: Hz) Hz

Const Freq Setting (F: Start)

Y Axis Data Values 0 0 0.0000E+0

X Axis Data Values 0 0

Polar Data Values 0 0 0 0.00

Nyquist Data Values copy 0 0 0.00 +0.00 i

Resolution (400)lines 1600

Full Frequency Span (F: No)

Number of Data Runs 10

File Name room

Save Location

error out

status ✓ code 0

source

B.2 Block Diagram

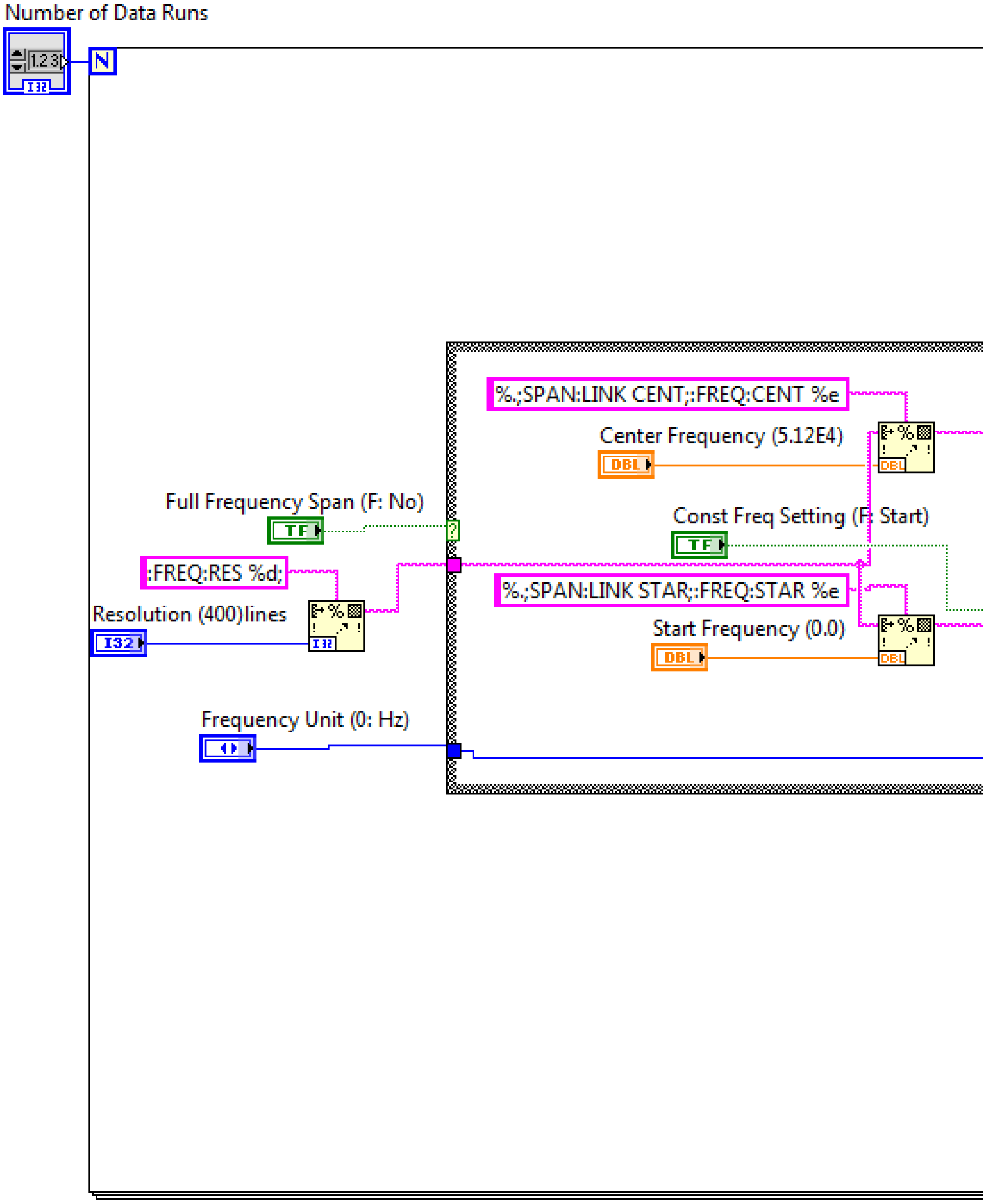

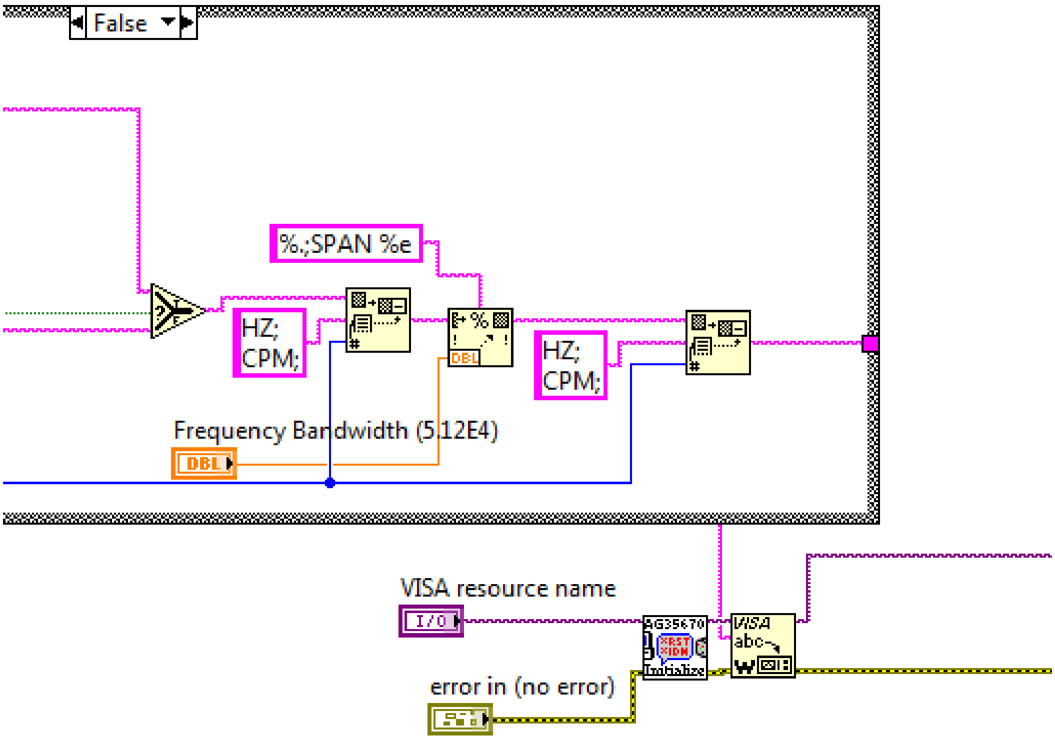
False
%.;SPAN %e
HZ;
CPM;
DBL
HZ;
CPM;
Frequency Bandwidth (5.12E4)
DBL
VISA resource name
I/O
AG35670
Initialize
VISA
abc
error in (no error)

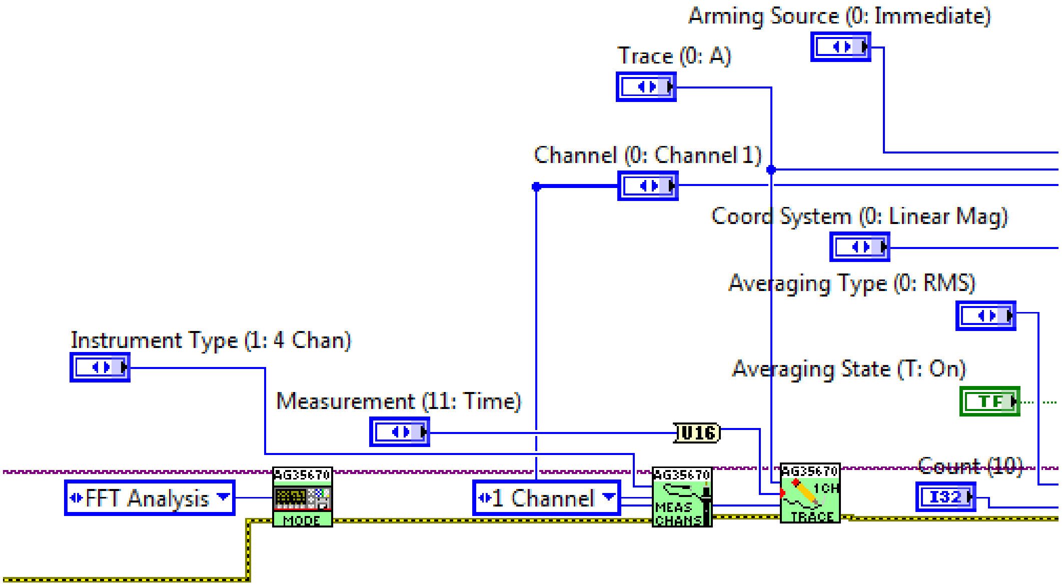
Arming Source (0: Immediate)
Trace (0: A)
Channel (0: Channel 1)
Coord System (0: Linear Mag)
Averaging Type (0: RMS)
Instrument Type (1: 4 Chan)
Averaging State (T: On)
Measurement (11: Time)
U16
TF
Count (10)
I32
FFT Analysis
AG35670
MODE
1 Channel
AG35670
MEAS CHANS
AG35670
1CH
TRACE

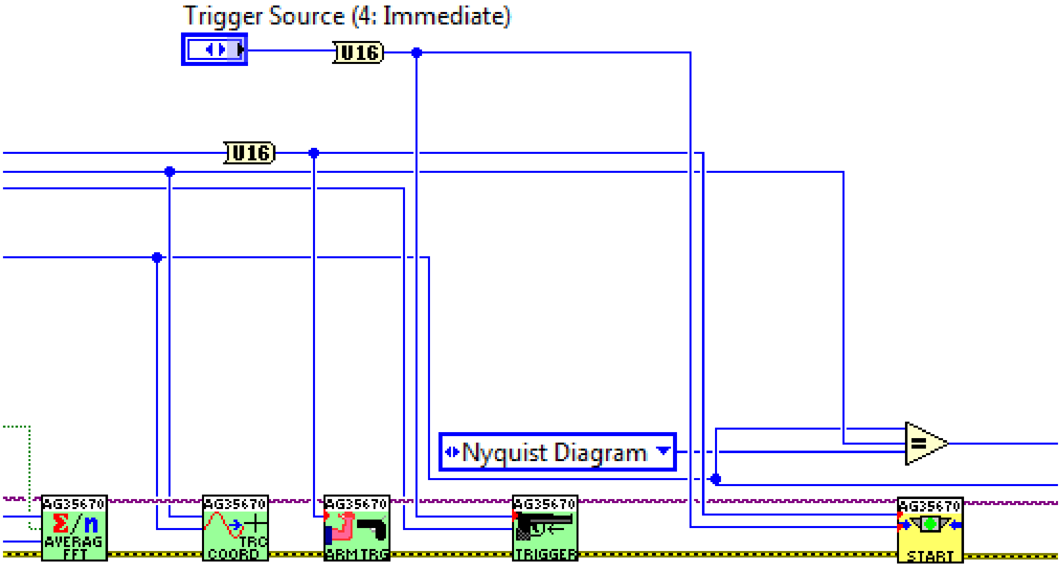
Trigger Source (4: Immediate)
U16
U16
Nyquist Diagram
AG35670
AVERAG FFT
AG35670
TRC COORD
AG35670
ARM TRG
AG35670
TRIGGER
AG35670
START

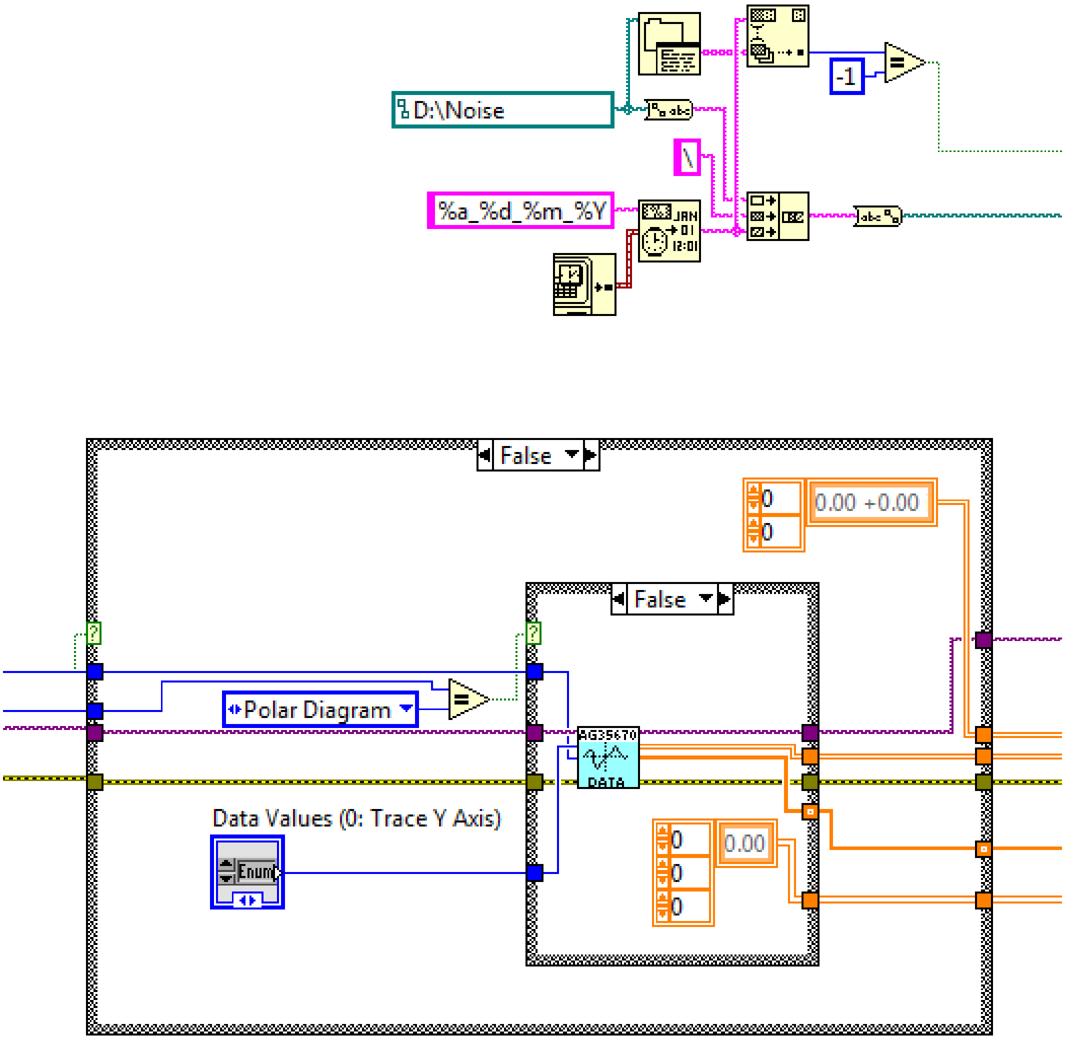
D:\Noise
\
%a_%d_%m_%Y
-1
False
0.00 +0.00
0
0
False
Polar Diagram
AG35670
DATA
Data Values (0: Trace Y Axis)
Enum
0
0
0
0.00

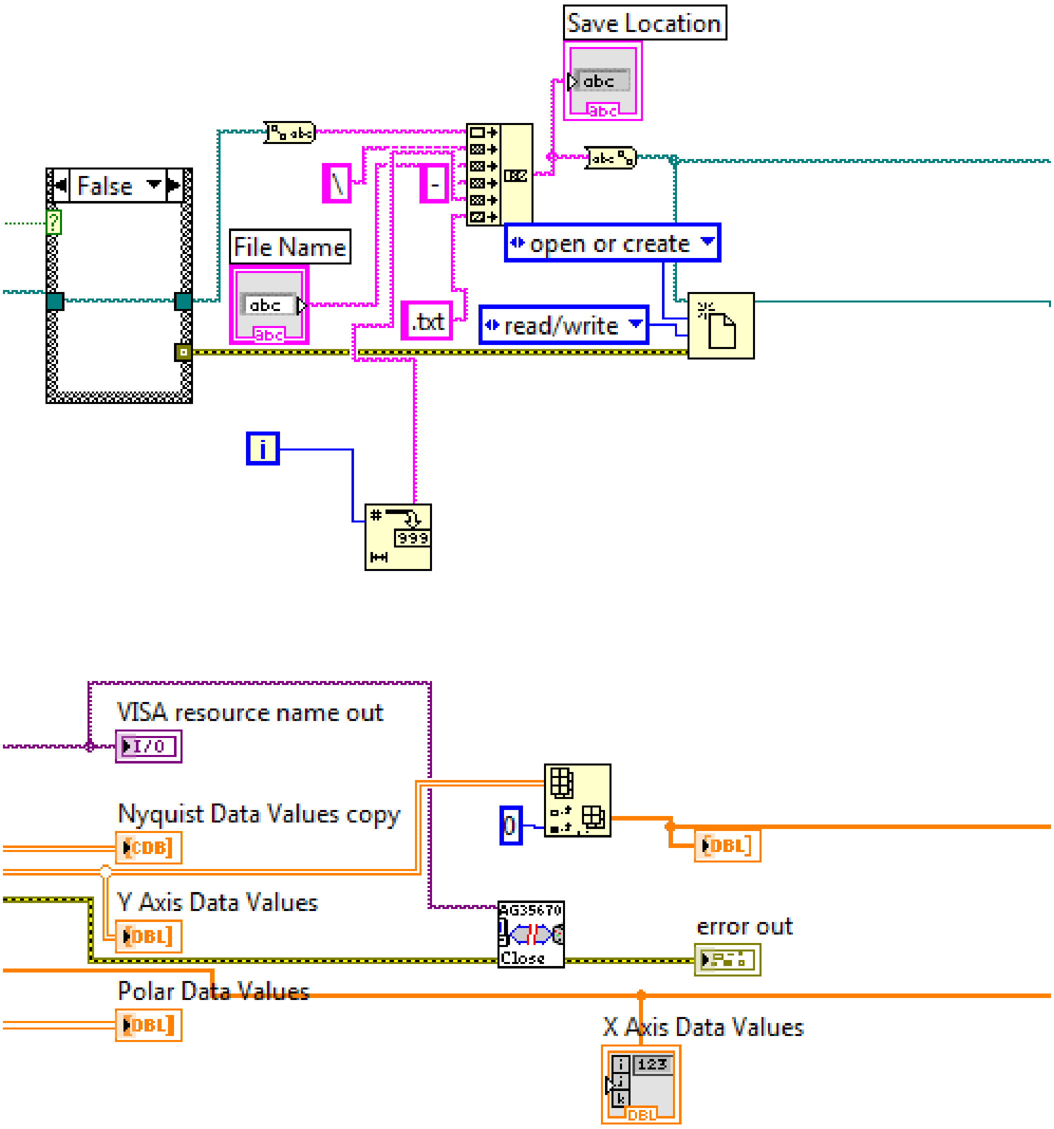
Save Location
abc
False
?
File Name
abc
\
-
.txt
open or create
read/write
i
999
VISA resource name out
I/O
Nyquist Data Values copy
CDB
Y Axis Data Values
DBL
Polar Data Values
DBL
0
DBL
AG35670
Close
error out
X Axis Data Values
123
DBL

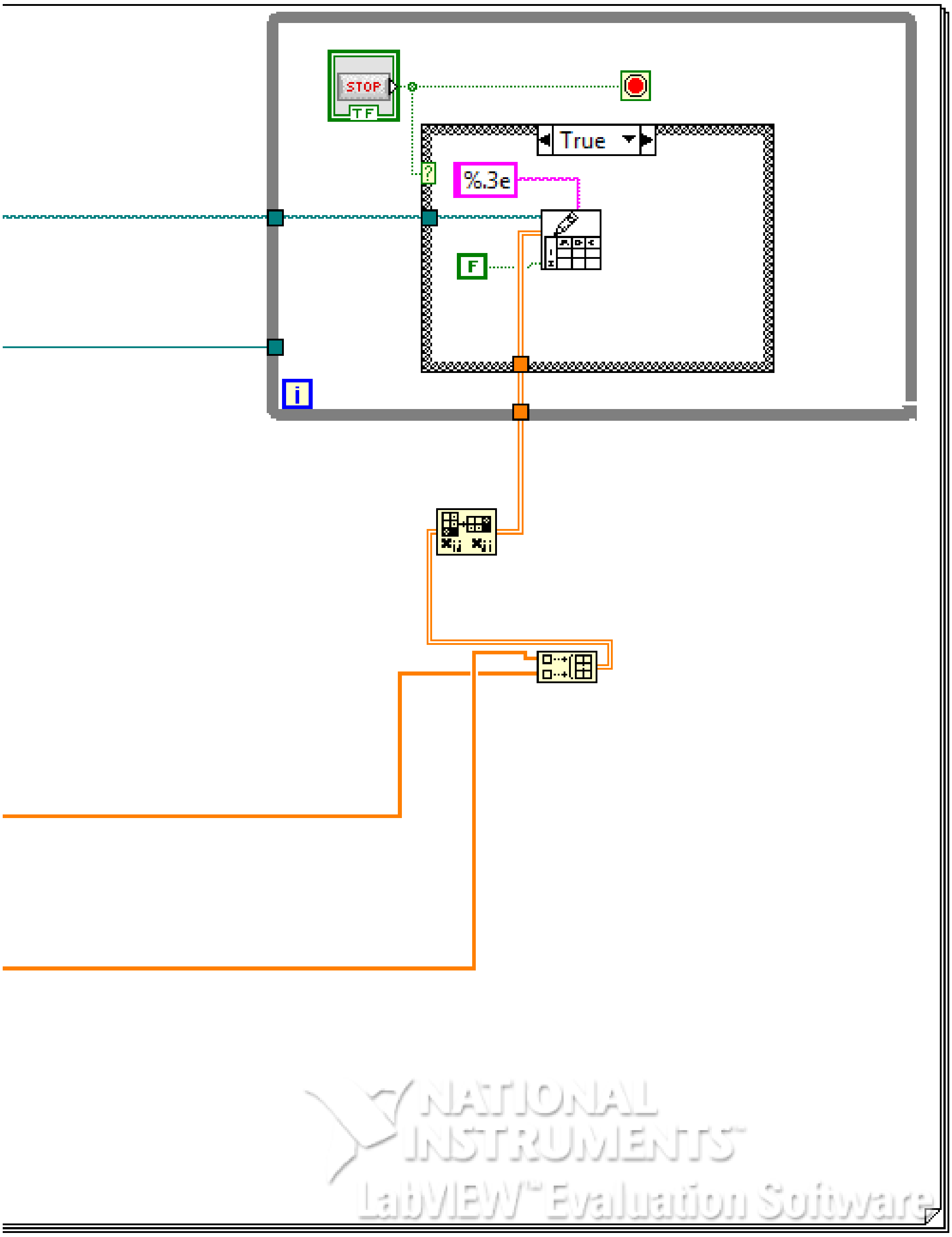
STOP
TF
True
?
%.3e
F
i

B.3 Hidden frames

The following are the subframes of the loops seen in the previous section, displayed in order.

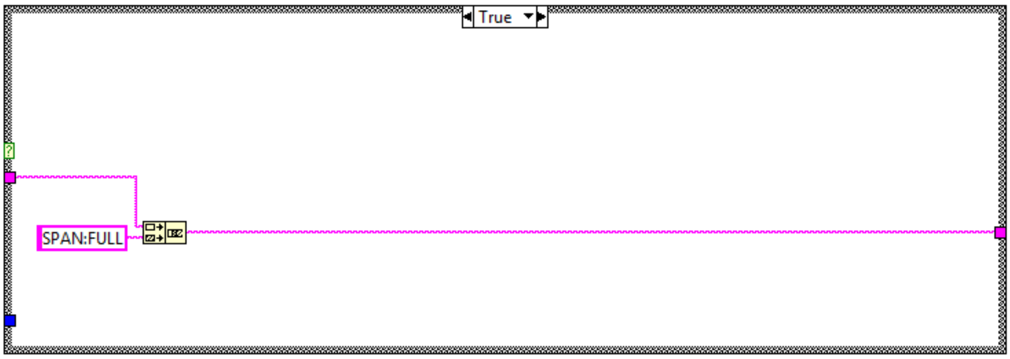

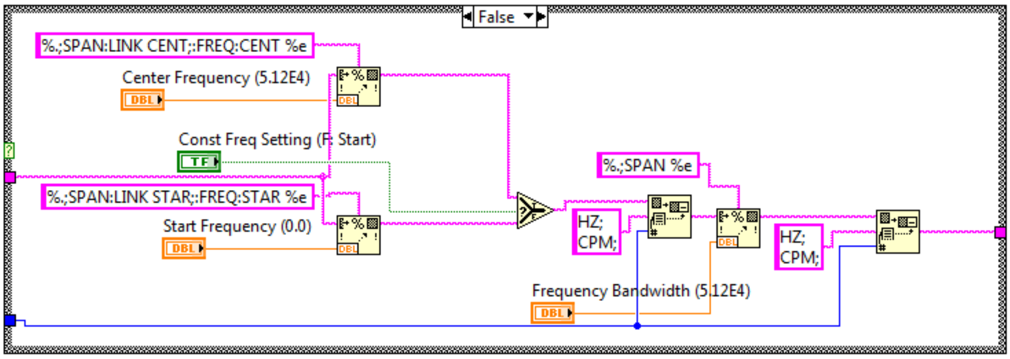

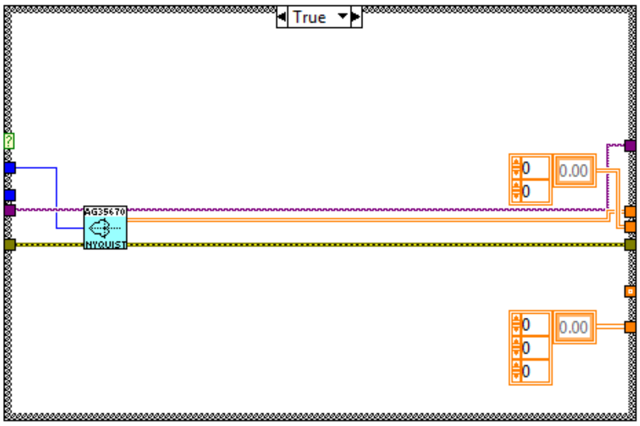

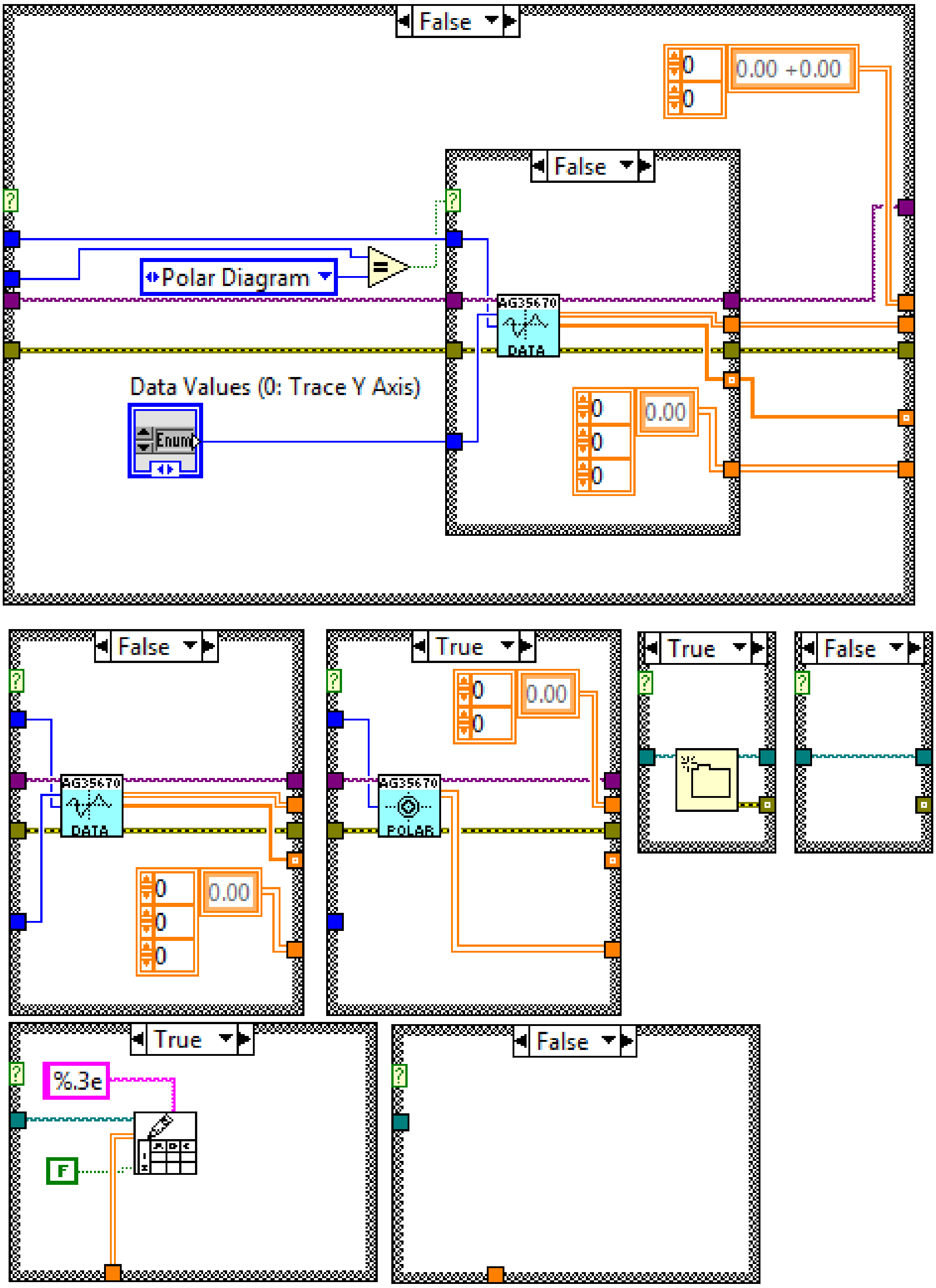
False
0
0
0.00 +0.00
False
Polar Diagram
Data Values (0: Trace Y Axis)
Enum
AG35670
DATA
0
0
0
0.00
False
AG35670
DATA
0
0
0
0.00
True
0
0
0.00
AG35670
POLAR
True
False
True
%.3e
F
False

Bibliography

[1] A. Einstein. *Die Grundlage der allgemeinen Relativitatstheorie. Annalen der Physik*, **49**:769, 1916.

[2] J. Weber. Detection and generation of gravitational waves. *Phys. Rev.*, 117:306–313, Jan 1960. doi: 10.1103/PhysRev.117.306. URL `http://link.aps.org/doi/10.1103/PhysRev.117.306`.

[3] J. Weber. Evidence for discovery of gravitational radiation. *Phys. Rev. Lett.*, 22:1320–1324, Jun 1969. doi: 10.1103/PhysRevLett.22.1320. URL `http://link.aps.org/doi/10.1103/PhysRevLett.22.1320`.

[4] R.A. Hulse and J.H. Taylor. A deep sample of new pulsars and their spatial extent in the galaxy. Oct 1975. URL `http://www.osti.gov/scitech/servlets/purl/4099936`.

[5] J.H. Taylor and J.M. Weisberg. New test of general relativity: Gravitational radiation and the binary pulsar psr 1913+16. Feb 1982. URL `http://www.osti.gov/scitech/servlets/purl/5130227`.

[6] Gregory M Harry, LIGO Scientific Collaboration, et al. Advanced ligo: the next generation of gravitational wave detectors. *Classical and Quantum Gravity*, 27(8):084006, 2010.

[7] Benno Willke, P Aufmuth, C Aulbert, S Babak, R Balasubramanian, BW Barr, S Berukoff, S Bose, G Cagnoli, MM Casey, et al. The geo 600 gravitational wave detector. *Classical and Quantum Gravity*, 19(7):1377, 2002.

[8] B Caron, A Dominjon, C Drezen, R Flaminio, X Grave, F Marion, L Massonnet, C Mehmel, R Morand, B Mours, et al. The virgo interferometer. *Classical and Quantum Gravity*, 14(6):1461, 1997.

[9] Yoichi Aso, Yuta Michimura, Kentaro Somiya, Masaki Ando, Osamu Miyakawa, Takanori Sekiguchi, Daisuke Tatsumi, Hiroaki Yamamoto, KAGRA Collaboration, et al. Interferometer design of the kagra gravitational wave detector. *Physical Review D*, 88(4):043007, 2013.

[10] CS Unnikrishnan. Indigo and ligo-india: Scope and plans for gravitational wave research and precision metrology in india. *International Journal of Modern Physics D*, 22(01), 2013.

[11] Kentaro Somiya. Detector configuration of kagra–the japanese cryogenic gravitational-wave detector. *Classical and Quantum Gravity*, 29 (12):124007, 2012.

[12] Peter R Saulson. *Fundamentals of interferometric gravitational wave detectors*, volume 7. World Scientific, 1994.

[13] VALERIA FERRARI. Gravitational wave sources. In B.G. SIDHARTH, F. HONSELL, and A. DE ANGELIS, editors, *Frontiers of Fundamental Physics*, pages 83–91. Springer Netherlands, 2006. ISBN 978-1-4020-4151-8. doi: 10.1007/1-4020-4339-2_13. URL `http://dx.doi.org/10.1007/1-4020-4339-2_13`.

[14] Curt Cutler and Kip S Thorne. An overview of gravitational wave sources. In *Proceedings of the GR16 Conference on General Relativity and Gravitation, ed. N. Bishop and SD Maharaj (World Scientific, 2002)*, pages 72–111, 2002.

[15] Leonid Petrovich Grishchuk, VM Lipunov, Konstantin Aleksandrovich Postnov, Mikhail Evgen'evich Prokhorov, and BS Sathyaprakash. Grav-

itational wave astronomy: in anticipation of first sources to be detected. *Physics-Uspekhi*, 44(1):1–51, 2001.

[16] Evonne Marietta, Adam Burrows, and Bruce Fryxell. Type ia supernova explosions in binary systems: The impact on the secondary star and its consequences. *The Astrophysical Journal Supplement Series*, 128(2):615, 2000.

[17] Brnard F Schutz. Gravitational-wave sources. *Classical and Quantum Gravity*, 13(11A):A219, 1996.

[18] Christopher J Moore, Robert H Cole, and Christopher PL Berry. Gravitational-wave sensitivity curves. *Classical and Quantum Gravity*, 32(1):015014, 2014.

[19] A De Waard, L Gottardi, J Van Houwelingen, A Shumack, and G Frossati. Minigrail, the first spherical detector. *Classical and Quantum Gravity*, 20 (10):S143, 2003.

[20] OD Aguiar, LA Andrade, JJ Barroso, F Bortoli, LA Carneiro, PJ Castro, CA Costa, KMF Costa, JCN de Araujo, AU de Lucena, et al. The brazilian gravitational wave detector mario schenberg: status report. *Classical and Quantum Gravity*, 23(8):S239, 2006.

[21] GA Prodi, L Conti, R Mezzena, S Vitale, L Taffarello, JP Zendri, L Baggio, M Cerdonio, A Colombo, V Crivelli Visconti, et al. Initial operation of the gravitational wave detector auriga. In *Second Edoardo Amaldi Conference on Gravitational Waves*, volume 4, pages 148–158, 1997.

[22] Karsten Danzmann and Albrecht Rüdiger. Lisa technology-concept, status, prospects. *Classical and Quantum Gravity*, 20(10):S1, 2003.

[23] Robin T Stebbins, Gravitational-Wave Study Team, et al. Future gravitational-wave missions. In *American Astronomical Society Meeting Abstracts*, volume 225, 2015.

[24] Rainer Weiss. Electromagnetically coupled broadband gravitational antenna. *MIT Res. Lab. Electron. Q. Prog. Rep*, 105:54–76, 1972.

[25] Rahul Kumar. *Finite element analysis of suspension elements for gravitational wave detectors.* PhD thesis, University of Glasgow, 2008.

[26] Paul Campsie. *Investigations of Charging Noise in Future Gravitational Wave Detectors.* PhD thesis, University of Glasgow, 2012.

[27] Éric Chassande-Mottin et al. Data analysis challenges in transient gravitational-wave astronomy. *arXiv preprint arXiv:1210.7173*, 2012.

[28] Joshua R Smith, LIGO Scientific Collaboration, et al. The path to the enhanced and advanced ligo gravitational-wave detectors. *Classical and Quantum Gravity*, 26(11):114013, 2009.

[29] J Aasi, J Abadie, BP Abbott, R Abbott, TD Abbott, M Abernathy, T Accadia, F Acernese, C Adams, T Adams, et al. Prospects for localization of gravitational wave transients by the advanced ligo and advanced virgo observatories. *arXiv preprint arXiv:1304.0670*, 2013.

[30] Stefan Hild, LIGO Scientific Collaboration, et al. The status of geo 600. *Classical and Quantum Gravity*, 23(19):S643, 2006.

[31] B Willke, P Ajith, B Allen, P Aufmuth, C Aulbert, S Babak, R Balasubramanian, BW Barr, S Berukoff, A Bunkowski, et al. The geo-hf project. *Classical and Quantum Gravity*, 23(8):S207, 2006.

[32] Fausto Acernese, P Amico, M Alshourbagy, F Antonucci, S Aoudia, S Avino, D Babusci, G Ballardin, F Barone, L Barsotti, et al. The virgo status. *Classical and Quantum Gravity*, 23(19):S635, 2006.

[33] Virgo Collaboration et al. Advanced virgo technical design report. *Virgo internal document VIR-0128A-12*, 2012.

[34] Yoichi Aso, Yuta Michimura, Kentaro Somiya, Masaki Ando, Osamu Miyakawa, Takanori Sekiguchi, Daisuke Tatsumi, and Hiroaki Yamamoto. Interferometer design of the kagra gravitational wave detector. *Phys. Rev. D*, 88:043007, Aug 2013. doi: 10.1103/PhysRevD.88.043007. URL `http://link.aps.org/doi/10.1103/PhysRevD.88.043007`.

[35] Stefan Hild. Beyond the second generation of laser-interferometric gravitational wave observatories. *arXiv preprint arXiv:1111.6277*, 2011.

[36] Scott A Hughes and Kip S Thorne. Seismic gravity-gradient noise in interferometric gravitational-wave detectors. *Physical Review D*, 58(12): 122002, 1998.

[37] M. Pitkin, S. Reid, S. Rowan, et al. *Gravitational Wave Detection by Interferometry (Ground and Space). Living Reviews in Relativity*, **14**(5), 2011.

[38] Jennifer C Driggers, Jan Harms, and Rana X Adhikari. Subtraction of newtonian noise using optimized sensor arrays. *Physical Review D*, 86 (10):102001, 2012.

[39] A V Cumming, A S Bell, L Barsotti, M A Barton, G Cagnoli, D Cook, L Cunningham, M Evans, G D Hammond, G M Harry, A Heptonstall, J Hough, R Jones, R Kumar, R Mittleman, N A Robertson, S Rowan, B Shapiro, K A Strain, K Tokmakov, C Torrie, and A A van Veggel. Design and development of the advanced ligo monolithic fused silica suspension. *Classical and Quantum Gravity*, 29(3):035003, 2012. URL `http://stacks.iop.org/0264-9381/29/i=3/a=035003`.

[40] J Hough. *Proposal for a joint German-British interferometric gravitational wave detector*. Max-Planck-Institut für Quantenoptik, 1989.

[41] Roman Schnabel, 9 2004. URL `http://www.geo600.uni-hannover.de/~schnabel/pagesli.html`.

[42] GD Hammond, AV Cumming, J Hough, R Kumar, K Tokmakov, S Reid, and S Rowan. Reducing the suspension thermal noise of advanced gravitational wave detectors. *Classical and Quantum Gravity*, 29(12):124009, 2012.

[43] G Cagnoli, H Armandula, CA Cantley, DRM Crooks, A Cumming, E Elliffe, MM Fejer, AM Gretarsson, GM Harry, A Heptonstall, et al. Silica suspension and coating developments for advanced ligo. In *Journal of Physics: Conference Series*, volume 32, page 386. IOP Publishing, 2006.

[44] Robert Brown. Xxvii. a brief account of microscopical observations made in the months of june, july and august 1827, on the particles contained in the pollen of plants; and on the general existence of active molecules in organic and inorganic bodies. *The Philosophical Magazine, or Annals of Chemistry, Mathematics, Astronomy, Natural History and General Science*, 4(21):161–173, 1828.

[45] Albert Einstein. Über die vom relativitätsprinzip geforderte trägheit der energie. *Annalen der Physik*, 328(7):371–384, 1907.

[46] Herbert B. Callen and Theodore A. Welton. Irreversibility and generalized noise. *Phys. Rev.*, 83:34–40, Jul 1951. doi: 10.1103/PhysRev.83.34. URL `http://link.aps.org/doi/10.1103/PhysRev.83.34`.

[47] T. J. Quinn, C. C. Speake, R. S. Davis, and W. Tew. Stress-dependent damping in Cu sbnd Be torsion and flexure suspensions at stresses up to 1.1 GPa. *Physics Letters A*, 197:197–208, February 1995. doi: 10.1016/0375-9601(94)00921-B.

[48] S. Twyford. *Development Towards Low Loss Suspensions for Laser Interferometric Gravitational Wave Detectors.* PhD thesis, University of Glasgow, 1998.

[49] Peter R Saulson. Thermal noise in mechanical experiments. *Physical Review D*, 42(8):2437, 1990.

[50] S. Reid. *Studies of materials for future ground-based and space-based interferometric gravitational wave detectors.* PhD thesis, University of Glasgow, 2006.

[51] Phil Willems, Peter Fritschel, David Shoemaker, Mark Barton, and Norna Robertson. Cavity optics suspension subsystem design requirements document. *Interface*, 3:5, 2001.

[52] A. Cumming. *Aspects of mirrors and suspensions for advanced gravitational wave detectors.* PhD thesis, University of Glasgow, 2008.

[53] Arthur S Nowick. *Anelastic relaxation in crystalline solids*, volume 1. Elsevier, 2012.

[54] VB Braginsky, ML Gorodetsky, and SP Vyatchanin. Thermodynamical fluctuations and photo-thermal shot noise in gravitational wave antennae. *Physics Letters A*, 264(1):1–10, 1999.

[55] John Bertrand Johnson. Thermal agitation of electricity in conductors. *Physical review*, 32(1):97, 1928.

[56] Harry Nyquist. Thermal agitation of electric charge in conductors. *Physical review*, 32(1):110–113, 1928.

[57] M Abernathy et al. Einstein telescope design study. 2011.

[58] L Conti, M Bonaldi, Lamberto Rondoni, et al. Rarenoise: non-equilibrium effects in detectors of gravitational waves. *Classical and Quantum Gravity*, 27, 2010.

[59] Denis J Evans, EGD Cohen, and GP Morriss. Probability of second law violations in shearing steady states. *Physical Review Letters*, 71(15):2401, 1993.

[60] G Gallavotti and EGD Cohen. Dynamical ensembles in nonequilibrium statistical mechanics. *Physical Review Letters*, 74(14):2694, 1995.

[61] *High Voltage, Low Noise, Low Distortion, Unity-Gain Stable, High Speed Op Amp.* Analog Devices, 10 2013.

[62] John E Mahan. Physical vapor deposition of thin films. *Physical Vapor Deposition of Thin Films, by John E. Mahan, pp. 336. ISBN 0-471-33001-9. Wiley-VCH, January 2000.*, 1, 2000.

[63] Rosello D Bergmann E. Corrosion protection with perfect atomic layers, June 2012. URL `http://www.polymedia.ch/OpArticles/view/57`.

[64] Michael A. Johnson and Mohammad H. Moradi. *PID Control : New Identification and Design Methods*. Springer, 2005.

[65] *HEL-700 Series Platinum RTDs.* Honeywell, 11 2013. URL `sensing.honeywell.com/index.php?ci_id=50012`.

[66] Inc ANSYS, 2014. URL `http://www.ansys.com/en_uk`.

[67] Colo United States. National Bureau of Standards. Cryogenic Engineering Laboratory, Boulder and V.J. Johnson. *A compendium of the properties of materials at low temperatures: (Phase 1-).* Number pt. 4 in WADD technical report. Wright Air Development Division, Air Research and Development Command, U.S. Air Force, 1961. URL `http://books.google.co.uk/books?id=dJJTAAAAYAAJ`.

[68] Robert C Weast. Handbook of chemistry and physics. *The American Journal of the Medical Sciences*, 257(6):423, 1969.

[69] Unknown. Agilent 35670 analyzer, 2005. URL `http://sine.ni.com/apps/utf8/niid_web_display.download_page?p_id_guid=015055A2BB3E343CE0440003BA7CCD71`.